9-2021

Development and Verification of Extreme Space Weather Phenomena Models

Sophia G. Schwalbe

Development and Verification of Extreme Space Weather Phenomena Models

DISSERTATION

Sophia G. Schwalbe, Capt, USAF

AFIT-ENP-DS-21-S-034

DEPARTMENT OF THE AIR FORCE
AIR UNIVERSITY

AIR FORCE INSTITUTE OF TECHNOLOGY

Wright-Patterson Air Force Base, Ohio

AFIT-ENP-DS-21-S-034

DEVELOPMENT AND VERIFICATION OF EXTREME SPACE WEATHER PHENOMENA MODELS

DISSERTATION

Presented to the Faculty

Graduate School of Engineering and Management

Air Force Institute of Technology

Air University

Air Education and Training Command

in Partial Fulfillment of the Requirements for the

Degree of Doctorate of Philosophy in Applied Physics

Sophia G. Schwalbe, M. S.

Capt, USAF

September 2021

AFIT-ENP-DS-21-S-034

DEVELOPMENT AND VERIFICATION OF EXTREME SPACE WEATHER PHENOMENA MODELS

DISSERTATION

Sophia G. Schwalbe, M. S.
Capt, USAF

Committee Membership:

Robert D. Loper, Ph.D.
Chair

Maj Daniel J. Emmons, Ph.D.
Member

Benjamin F. Akers, Ph.D.
Member

Abstract

A range of 14 M-class flares from 1 June 2015 to 27 September 2016 were analyzed to find significant trends in electron frequency profile modeling using the GLobal airglOW (GLOW) model and radar parameters using a ray tracing algorithm developed by the Air Force Research Laboratory. GLOW was run for all the flares using three different solar spectrum schemes and an average of the three: the Hinteregger method, EUV flux model for aeronomic calculations (EUVAC), and a rebinned Flare Irradiance Spectrum Model (FISM) result. Comparing data for the E-layer where GLOW is most accurate, it was determined that GLOW using EUVAC performed best at the peak flare time for determining both the peak altitude and frequency of the E-region, while using FISM as a user-supplied spectrum in GLOW was less accurate for estimating both, likely due to the extreme variations in solar flux, coarse binning scheme, and lack of robust chemistry and energy calculations within GLOW. GLOW performed better at predicting peak altitude and frequency than the International Reference Ionosphere (IRI), which is often used as a basis for ionosphere predictions. GLOW also outperformed IRI at modeling the radar parameters before and during the solar flares, though no significant trends were found. GLOW using EUVAC or FISM showed promise at predicting the radar parameters and their change over time, but the ray tracing algorithm produced solutions that varied between E- and F-layers and O- and X-modes, leading to results that were often skewed or varied drastically in time.

Acknowledgements

No endeavor is ever accomplished alone, so I would like to thank everyone I have encountered in my journey for their contributions to this work. From the second lieutenants I entered AFIT with that formed my first support network, to all my military mentors from AFROTC and AFIT that encouraged and enabled me to pursue this degree, to my parents and partner that have provided me unending support - I could not have done this without you.

I would like to especially thank my advisors, Dr. Robert Loper and Maj Daniel Emmons, from the bottom of my heart. Your support and mentorship is what has allowed me to finish this program and has given me incredible opportunities that I will treasure.

A special thanks is given to Stanley Solomon for his assistance with GLOW, Eugene Dao for the use of his ray tracing algorithm, and Greg Ginet for his help in acquiring the CODAR data used for the ray tracing algorithm.

In addition, this paper uses data from the Millstone Hill ionosonde, operated by Bodo Reinisch and UMLCAR, and this paper uses data from FISM2, managed by Phillip Chamberlin and Laboratory for Atmospheric and Space Physics (LASP) at University of Colorado Boulder.

Sophia G. Schwalbe

Table of Contents

Page

List of Figures

List of Tables

List of Acronyms

AE-E Atmospheric Explorer E

AFRL Air Force Research Laboratory

AoA Angle of Arrival

CCMC Community Coordinated Modeling Center

CME Coronal Mass Ejection

CODAR Coastal Ocean Dynamics Applications Radar

DIDBase Digital Ionogram DataBase

DoD Department of Defense

DOE Department of Energy

ESA European Space Agency

EUV Extreme Ultraviolet

EUVAC EUV Flux Model for Aeronomic Calculations

EVE Extreme-ultraviolet Variability Experiment

F10.7 Solar radio flux at 10.7 cm

foE Peak Frequency of the E-region

foF2 Peak Frequency of the F_2-region

GIRO Global Ionospheric Radio Observatory

GITM Global Ionosphere Thermosphere Model

GLOW The GLobal airglOW Model

GNSS Global Navigation Satellite System

GOES Geostationary Operational Environmental Satellites

GPS Global Positioning System

HAO High Altitude Observatory

hmE Peak Altitude of the E-region

hmF2 Peak Altitude of the F_2-region

HPI Hemispheric Power Index

HWM Horizontal Wind Model

IFM Interplanetary Magnetic Field

IGRF International Geomagnetic Reference Field

IRI International Reference Ionosphere

ISR Incoherent Scatter Radar

MHD Magnetohydrodynamics

NASA National Aeronautics and Space Administration

NCAR National Center for Atmospheric Research

nmE Peak Electron Density of the E-region

nmF2 Peak Electron Density of the F_2-region

NOAA National Oceanic and Atmospheric Administration

NORAD North American Aerospace Defense Command

NRLMSISE-00 Naval Research Laboratory, mass spectrometer and incoherent scatter radar, extending through the exosphere, released in 2000

NSWP National Space Weather Program

OSTP Office of Science and Technology Policy

PROSWIFT Promoting Research and Observations of Space Weather to Improve the Forecasting of Tomorrow Act

SAMI3 Sami3 is Also a Model of the Ionosphere

SEE Solar EUV Experiment

SESS Space Environment Support System

sfu Solar Flux Units, [$\times 10^{-22}$ W Hz^{-1}m^{-2}]

SOFNET Solar Observing and Forecasting Network

SOLSTICE Solar Stellar Irradiance Comparison Experiment

SORCE SOlar Radiation & Climate Experiment

SpaceWOC Space Weather Operations Center

SPE Solar Proton Event

SRB Solar Radio Burst

SWORM Space Weather Operations, Research and Mitigation Working Group

SWPC Space Weather Prediction Center

TEC Total Electron Content

TECU Total Electron Content Units, [$\times 10^{16} \mathrm{m}^{-2}$]

TIE-GCM Thermosphere-Ionosphere-Electrodynamics General Circulation Model

TIMED Thermosphere Ionosphere Mesosphere Energetics and Dynamics mission

UCAR University Corporation for Atmospheric Research

USAF United States Air Force

USSF United States Space Force

USU-GAIM Utah State University - Global Assimilation of Ionospheric Measurements

UTC Coordinated Universal Time

XPS X-ray Photometer System

XRS X-Ray Sensor

I. Introduction

1.1 Motivation

On 29 May 2020, the first solar flare of solar cycle 25 erupted at 0724 UTC after 925 days without large (M-class or higher) flares and 118 days without sunspots. It was detected by the STEREO spacecraft and classified as an M1.1 flare (Carter, 2020). While this event was significant to the space weather community as a start to the ramp up to solar maximum, it is also significant to many facets of day-to-day life, as solar flares can degrade radio signals, global positioning systems (GPS), and satellite communications (Board et al., 2008; Cannon et al., 2013). Further, solar flares can be accompanied by coronal mass ejections (CMEs), which can create geomagnetic storms that in turn can adversely affect ground-based electronic systems such as power grids (Cannon et al., 2013).

The worst example of this is known as the Carrington Event (Carrington, 1859; Hodgson, 1859). This event occurred on 1 September 1859 and was the most intense flare ever recorded, accompanied by an equally powerful CME that overloaded telegraph lines and created aurora as far south as Cuba and Hawaii (Kimball, 1960). If a similar event were to impact the Earth today, it is estimated that the damage caused would cost from $30 to $70 billion to just repair the satellite fleet (Bell and Phillips, 2008), and from $1 to $2 trillion in the first year for the world to recover. Ultimately, it would take four to ten years to recover completely (Board et al., 2008). Radio signals, cellular communications, satellite communications, and GPS would all vanish, and at least some power grids would be knocked out as well. This has occurred with more recent events like the 13 March 1989 solar storm and the 2003 Halloween storms, both of which affected regional power grids in Canada and Sweden, respectively. Currently, electromagnetic vulnerabilities have been examined by gov-

ernment institutions (Stuckenberg et al., 2018) due to the devastating effects natural or man-made disruptions might have on the public.

This becomes all the more relevant with recent predictions concerning the intensity of solar cycle 25. Initially, scientists in the international NOAA/NASA co-chaired Solar Cycle 25 Prediction Panel had agreed that the new cycle would be similar to the previous cycle with between 95 and 130 sunspots per month (NOAA Space Weather Prediction Center, 2019) - which are considered indicators of solar activity. However, a new method for sunspot predictions for the average monthly sunspot number has indicated that solar cycle 25 might be twice as active as solar cycle 24 with a 95% confidence level of there being between 153 and 305 sunspots per month (McIntosh et al., 2020), meaning that the likelihood of larger flares increases significantly.

In addition to global interest in space weather, the United States Air Force (USAF) in particular has a long history with space weather research, beginning in 1948 when Harvard University astronomer Dr. Donald Menzel set up the framework for solar observatories to continue radio propagation research that started in World War II (Liebowitz, 2002). The USAF Air Weather Service (AWS) expanded its observations to the sun after the launch of *Sputnik*-1 and the Solar Observing and Forecasting Network (SOFNET) was formed to provide solar predictions to support the North American Aerospace Defense Command (NORAD). In 1965, to assist SOFNET with its mission, the 4th Weather Wing created the Solar Forecast Center, which was co-located with NORAD to assist in real-time decisions (Markus et al., 1987). This was also the start of continuous space weather observations and four daily space weather forecasts. By 1967, USAF had global observation locations for solar activity, four in the United States, one in Greece, and one in the Philippines (Knipp et al., 2016).

Between 21 and 28 May 1967, extreme space weather events captured national attention when a highly active sunspot began emitting large solar radio bursts (SRBs),

flares, and x-ray emissions. The sunspot, noted as McMath Plage Region 8818, produced 76 significant flares, 3 large radio bursts, a long solar proton event (SPE) that began on 23 May and was closely followed by a massive CME, and a geomagnetic storm that affected many space and radio operations (Knipp et al., 2016). The extreme SRBs caused signal losses and communications blackouts at high latitude sites, which at the time were predominantly military bases. Due to the political climate of the Cold War at the time, such SRBs were interpreted as jamming signals until the AWS informed NORAD of the space weather events occurring (Citrone, 1995). As a consequence, the AWS consolidated SOFNET and all other space observation programs into the Space Environment Support System (SESS) in 1968, which moved to Offut Air Force Base to support continuous ionospheric forecasting. In 1972 the AWS and the National Oceanic and Atmospheric Administration (NOAA) came to an agreement for a cooperative forecasting efforts that remains in effect to this day (Poppe and Jorden, 2006) through NOAA's Space Weather Prediction Center (SWPC) and USAF's Space Weather Operations Center (SpaceWOC).

Space weather policy changed again in 1994 with the creation of the National Space Weather Program (NSWP) under the Office of the Federal Coordinator for Meteorological Services and Supporting Research (Bonadonna et al., 2017). This coalition ended in 2015, but it marked a huge shift in emphasis on to space weather and a community of cooperation. In 2010, meanwhile, the White House Office of Science and Technology Policy (OSTP) was directed by Congress to help manage NSWP activities and increase preparedness for extreme space weather events (Lipiec and Humphreys, 2020). This culminated in the formation of the Space Weather Operations, Research and Mitigation (SWORM) Working Group in 2014 and the subsequent release of the 2015 report, USA National Science and Technology Council (2015). This was followed by an executive order (Obama, 2016) to coordinate roles

in space weather research and response in 2016, and an additional executive order in 2019 (Trump, 2019) that added emphasis to the country's response to electromagnetic pulses (EMPs). Congress outlined specific space weather roles in the 115th Congress (2018). SWORM released an updated strategy plan in 2019 (Space Weather Operations; Research; and Mitigation Working Group et al., 2019), which helped inform the passage of the 2019 Promoting Research and Observations of Space Weather to Improve the Forecasting of Tomorrow (PROSWIFT) Act(116th Congress, 2020). This law gave a definitive directive on predicting space weather and extreme space weather events like flares.

Given the magnitude of the impact that large flares can have on terrestrial systems, it is important to understand how they affect the earth-space environment. Multiple computational models exist to illustrate the inherent physics in the sun, magnetosphere, and ionosphere, and some of these models can compute the effect of a solar flare on radio and electric power systems (Huang et al., 2014). However, ionosphere models typically do not have small enough time scales for extreme space weather phenomena like flares, even though this region is where signals such as radio waves propagate and are reflected. It is therefore imperative to analyze extreme space weather phenomena with applicable models in order to anticipate their effects on the ionosphere and to use these results to determine the influence on communication signals.

1.2 Research Objectives

This research aims to accomplish two major goals: first, find an ionosphere model that can accurately predict the change in the ionosphere caused by a solar flare; and second, illustrate how the solar flare affects high frequency (HF) skywave circuits.

The first relies on finding a model that can be run quickly, but can be run over

a small time scale to match a flare's time scale of minutes to hours. The model also cannot just use a solar proxy for the solar spectrum, as solar proxies are averaged over the day to eliminate extreme fluxes caused by events like solar flares. Instead, the model must allow for a user-supplied spectrum. This user-supplied spectrum will be compared to various spectra calculated from solar proxies to determine which provides the most accurate electron frequency profile during a flare. The model results will be compared to ground-based ionosonde measurements for the same flare period.

The second objective is to try to model HF signals under the ionospheric effects from M-class solar flares. This portion uses a ray tracing algorithm that can compute group delay, azimuth angle, and elevation angle to compare to measured HF angle-of-arrival (AoA) data from the same time period. This ray tracing algorithm computes the ray paths through the electron frequency profiles, so again the computed profiles from the different solar spectra will be compared. This will inform to what extent the solar flare affects the propagation of a radar signal.

1.3 Preview

Chapter II provides relevant background information, to include the necessary concepts in solar and ionospheric physics and an introduction to the models that are commonly used for current research. This will also include an analysis of the codes and data used for this research. Chapter III details the first component of the research that examines an ensemble of solar flares for use with an existing ionospheric model, in this case the GLobal airglOW (GLOW) model. GLOW will be used to model the ionospheric response to these solar flares, and the model efficacy will be compared to ionosonde data for validation. The generated electron frequency profiles from this portion will inform the work of Chapter IV, where the profiles will be used in a ray tracing algorithm to produce a prediction of radar performance and then compared to

data from a coastal ocean dynamics applications radar (CODAR). Chapter V provides the final conclusions and outlines how the research may be expanded. An appendix is included for additional figures and tables too long to include in the main body of text.

II. Background

2.1 Earth's Ionosphere

The upper atmosphere of Earth, where ionization occurs and plasma is present, is part of Earth's radiation environment. The terrestrial ionosphere is a layer of Earth's atmosphere above the troposphere and stratosphere, usually starting in the mesosphere between 40 km and 100 km depending on the reference, and extending up to roughly 1,000 km into the thermosphere and exosphere (Pisacane, 2016). The ionosphere is said to be the lower bound of the magnetosphere. It is characterized by the significant number of free electrons and accompanying ions which form a plasma layer. Figure 1 shows the stratification of the layers of the atmosphere. Historically, scientists have known about interactions in the upper atmosphere for millennia through the existence and observation of aurorae. However, the ionosphere as a layer was not hypothesized until the 1800s when Carl Gauss and Balfour Stewart theorized the existence of electric currents in the atmosphere (Schunk and Nagy, 2009). Then, in 1902, Arthur E. Kennelly (Kennelly, 1902) and Oliver Heaviside (Heaviside, 1902) independently predicted that there was a highly conductive layer in the atmosphere, termed the "Heaviside layer", to explain Guglielmo Marconi's radio transmissions, which were the first evidence of the layer (Russel et al., 2016). The existence was finally verified in 1925 when the first accepted measurements were taken by Gregory Breit and Merle A. Tuve in the U.S. (Breit and Tuve, 1925) and Edward V. Appleton and M. A. F. Barnett (Appleton and Barnett, 1925) in the United Kingdom.

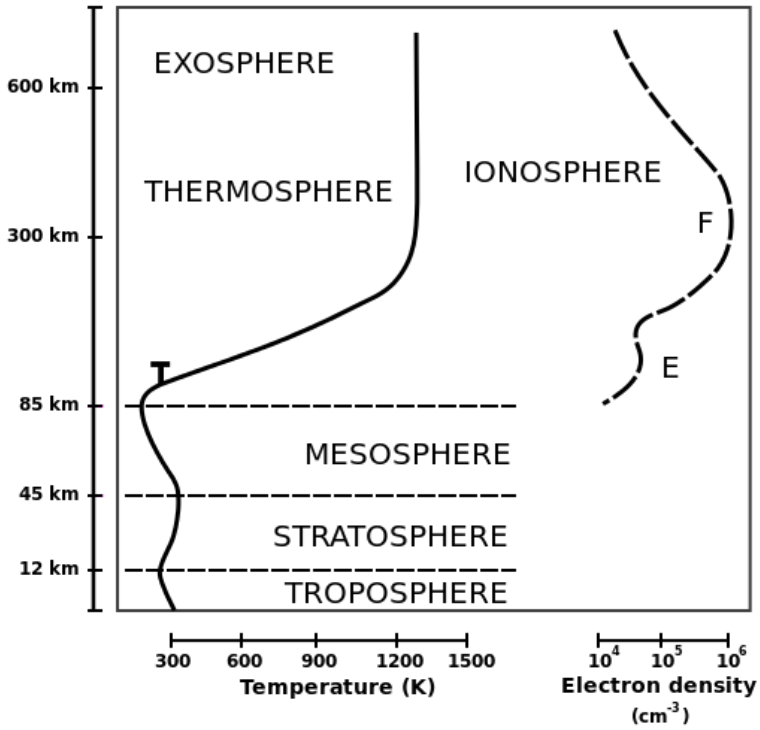

Figure 1. The ionosphere is distinguished from the atmosphere by its temperature and its electron density. It is a part of the thermosphere, situated above the troposphere, stratosphere, and mesosphere, but below the magnetosphere and protonosphere. Figure public domain, courtesy of Bhamer.

The ionosphere is divided into main three layers: the D-layer, E-layer, and the F-layer, with the F-layer being split into the F_1-layer and F_2-layer during the daytime, since the ionizing photons create two distinct electron density peaks; at night, however, the ionization processes stop and the two F-layers merge. Literature will sometimes refer to these altitude regimes as regions rather than layers, but to remain consistent will be referenced as layers here. The layers are distinguished from each other by the peak electron densities as a function of height, as can be distinguished in the electron density profiles in Figure 2. The different layers have been shown to have different transport mechanisms and drivers, as discussed in the relevant subsections.

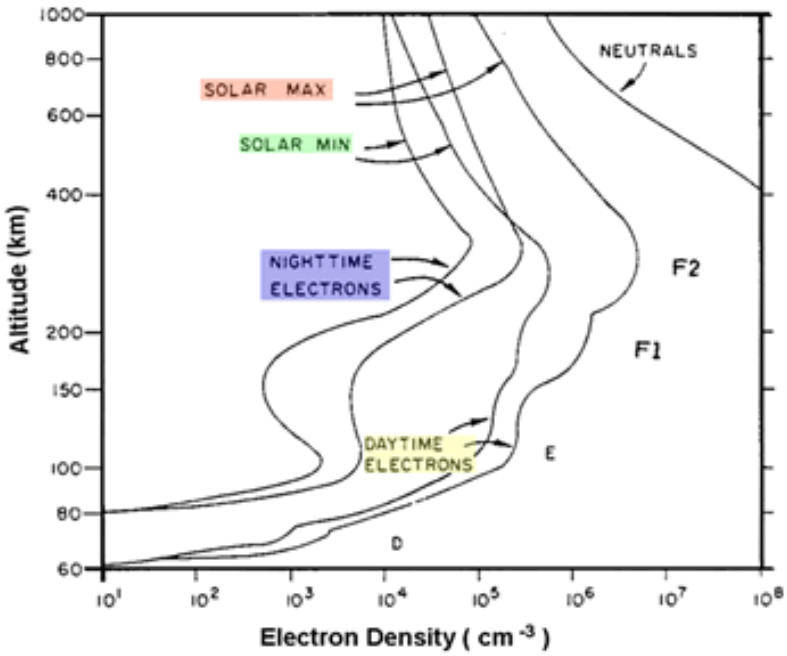

Figure 2. The ionosphere is subdivided into four layers: the *D*-layer, *E*-layer, F_1-layer, and F_2-layer. The ionosphere is separated by electron density peaks. Figure courtesy of Peter Guest at the Naval Postgraduate School, Department of Meteorology.

D-Layer.

The *D*-layer of the ionosphere is the lowest layer, located between approximately 40 km to 95 km. This layer is heavily driven by hard x-rays with wavelengths between 0.1-1 nm and by Lyman α radiation with a wavelength of 121.5 nm (Pisacane, 2016). These radiation regimes ionize N_2, O_2, O, and NO. The major ion species that result from the ionization are NO^+ and O_2^+. These ion species cause hydration in this layer, which cause water cluster ions and cause three-body chemical reactions (Schunk and Nagy, 2009). Further, negative ions can be found in this layer, further complicating the chemistry. This layer essentially disappears at night, but during the day the electron number density (N_e) can be on the order of magnitude of 10^9 m^{-3} (Pisacane, 2016), with neutral densities ranging from 10^{23} m^{-3} at the bottom of the layer to 10^{19} m^{-3} at the top (Mitra, 1978).

***E*-Layer.**

The first observed layer of the ionosphere was the E-layer. Directly above the D-layer, it extends from 95 km to 150 km. In this layer, soft x-rays with wavelengths from 1-10 nm ionize N_2, O_2, O, and NO, while ultraviolet radiation from approximately 80 nm to 102.7 nm ionizes O_2 that combines with nitrogen to create NO^+ (Pisacane, 2016). The E-layer can be well modeled by production and recombination mechanisms, and has a distinct peak at about 120 km; this peak shifts upwards in altitude at night. Typically, the E-layer has an N_e of 10^{11} m^{-3} (Pisacane, 2016) but with a neutral density of 10^{17} m^{-3} (Schunk and Nagy, 2009), which makes this layer weakly ionized. It is also known for the sporadic-E phenomena.

***F*-Layer.**

Above the E-layer is the F-layer, extending from 150 km to approximately 1,000 km. The F-layer is ionized by EUV radiation in the regime of 10-100 nm, which ionizes atomic oxygen and, at higher altitudes, H and He (Pisacane, 2016). This layer splits into two distinct layers during the day: the lower layer, the F_1-layer, is typically found between 150 km and 250 km and is driven by some chemical reactions and some transport mechanisms (Schunk and Nagy, 2009) with an N_e between 2-5 $\times 10^{11}$ m^{-3} (Pisacane, 2016); the F_2-layer extends into the protonosphere and exhibits the ionization maximum, where the transport mechanisms are balanced by the chemical losses. The peak value normally occurs between 300 km and 350 km and has an N_e of 10^{12} m^{-3} during the day, but an order of magnitude less at night (Pisacane, 2016), and a neutral density of 10^{14} m^{-3} (Schunk and Nagy, 2009). The layer above the F_2-layer peak is referred to as the topside ionosphere. The difference between the F_1-layer and the F_2-layer during the day results from decrease in recombination coefficient for the chemical reactions as the altitude increases.

2.2 Extreme Space Weather Phenomena

The ionosphere is highly dependent on solar activity, which is most obvious when concerning extreme solar events like flares. However, flares are not the only extreme space weather events that can affect the the ionosphere. Geomagnetic activity can also affect the ionosphere, as can human effects like nuclear detonations. To fully understand how to model the affects of these events, first it is necessary to understand the events themselves and what components affect the ionosphere.

2.2.1 Solar Flares

Some of the most impressive space weather events are solar flares. These are massive ejections of electromagnetic radiation and energetic particles into space, caused by the disturbance of the magnetohydrodynamic (MHD) equilibrium of the Sun's magnetic field. Energy stored in the magnetic field lines is released, up to 10^{25} J over a time span of seconds to minutes (Foukal, 2013). These areas of high magnetic activity are often noticeable in the visible spectrum in the form of dark spots on the photosphere of the Sun, called sunspots. Flares are classified by either the radiation emissions in the visible spectrum or the X-ray spectrum; the visible spectrum classification, based on the Hα line of the Balmer series, uses total size of the brightening on the solar disk and the relative brightness, but is less reliable than the X-ray spectrum classification in Table 1 which relies on the flux in the 1-8 Å wavelength range (Kranich, 2015).

Table 1. The designators for the X-ray classifications for solar flares, based on the flux in the 1-8 Å wavelength range (Kranich, 2015). The flare is classified first with a letter, then with the logarithmic coefficient of the flux; for example, the two solar flares associated with the 1989 storms were an X4.5 (4.5×10^{-4} W/m^2) and an M7.3 (7.3×10^{-5} W/m^2) (Boteler, 2019).

Letter Designator	Peak X-ray Flux [W/m^2]
A	$< 10^{-7}$
B	10^{-7}-10^{-6}
C	10^{-6}-10^{-5}
M	10^{-5}-10^{-4}
X	$> 10^{-4}$

A flare typically occurs in three stages: the pre-flare phase, the impulse or flare, and decay, as shown in Figure 3. In the pre-flare phase, the active region brightens in the X-ray and extreme ultra-violet (EUV) spectrum, and the magnetic field lines become increasingly unstable. This lasts on the order of minutes, but can endure for several hours (Foukal, 2013). The impulsive phase is when the greatest amount of energy is released, and the maximum emissions from the X-ray, EUV, microwave, and Hα spectra are detected, which are used to mark the time of the flare (Kranich, 2015). Then, there is the decay phase, characterized by a decrease of the radiation back to pre-flare levels. However, strong magnetic regions may continue to have flare eruptions, which can extend the time frame to the order of days.

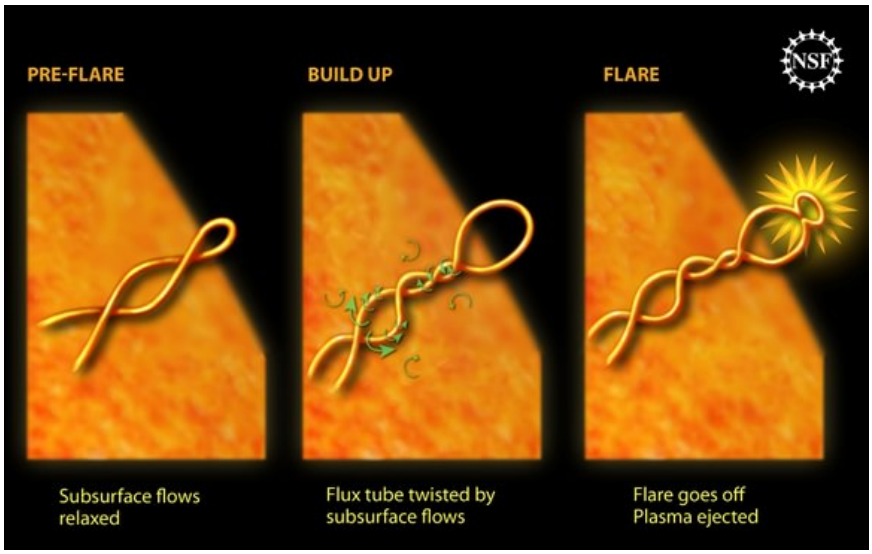

Figure 3. The main stages of a solar flare, excluding the decay phase. Often, the build up and the pre-flare are combined as one phase, and the impulse is when the flare is officially determined to have erupted. Figure taken from NOAA (Atkinson, 2010).

2.2.2 High-Altitude Nuclear Detonations

Another significant extreme event to consider is a high-altitude nuclear detonation (HAND). HANDs have similar effects on the ionosphere as solar flares and CMEs, as they increase the received solar flux (Schwalbe, 2019) and create significant fluctuations in the ionospheric currents. One fission reaction results in the generation of approximately 200 MeV in products. Roughly 85% of the energy is released in the form of fission fragments. Approximately 93% of the prompt energy from the fission reaction, meanwhile, goes to the kinetic energy of the fission fragments, with the remaining fraction being split between neutrons and gamma rays (Bridgman, 2001). Gamma rays will typically only be 0.1-0.3% of the total yield. The kinetic energy of the fission fragments is transformed into radiation that corresponds with X-rays, so anywhere from 70 to 80% of the total yield of a weapon will be in the form of X-rays (Conrad et al., 2010). The remaining yield is split between thermal and blast effects,

as shown in Figure 4, though the percentage of X-rays goes up with altitude as the other effects cannot manifest due to decreased environmental interaction.

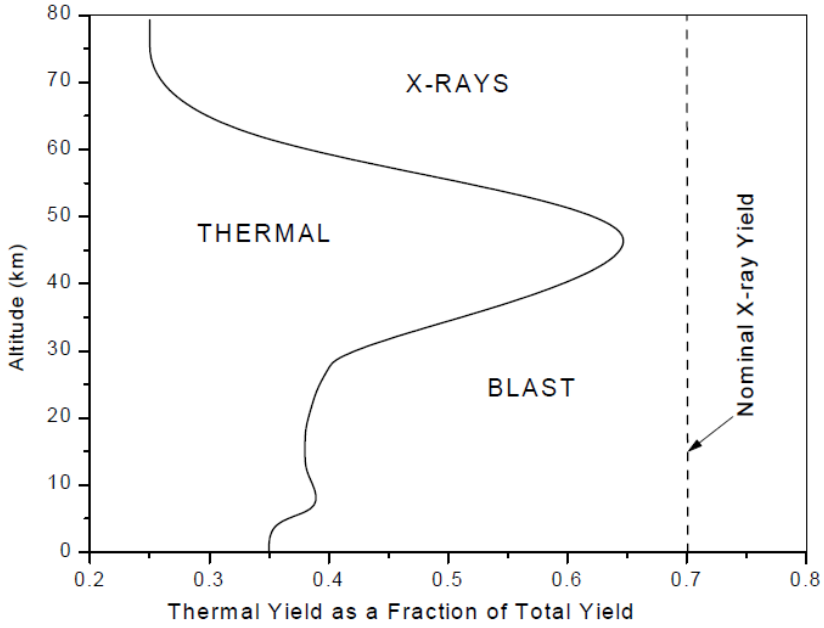

Figure 4. The nominal X-ray yield of a typical nuclear weapon is between 70-80 % of the total yield, shown by the dashed vertical line, with the remaining fraction being split between blast and thermal effects, denoted by the solid line. The exact percentages are highly dependent on the altitude of detonation, with the X-ray yield increasing as the atmosphere thins. Figure taken from Bridgman (2001).

The emitted X-rays from the weapon are part of the blackbody spectrum of the nuclear explosion. A blackbody is an object that absorbs all radiation and reflects none of it. When a nuclear detonation occurs, the resulting photons form a wavelength (λ) spectrum with intensity, or spectral radiance, I, based on Planck's equation,

$$I(\lambda) = \frac{2hc^2}{\lambda^5} \frac{1}{\exp[hc/\lambda kT] - 1}, \tag{1}$$

where h is Planck's constant, c is the speed of light, k is the Boltzmann constant, and T is the temperature of the blackbody at thermal equilibrium. The equation can also be written in terms of frequency ν as

$$I(\nu) = \frac{2h\nu^3}{c^2} \frac{1}{\exp[h\nu/kT] - 1}. \tag{2}$$

Between the extreme ultraviolet (EUV) and radio wavelengths, a blackbody curve can be used to fit the emission spectrum of the Sun, though the Sun is not a perfect emitter outside of this region, as shown in Figure 5.

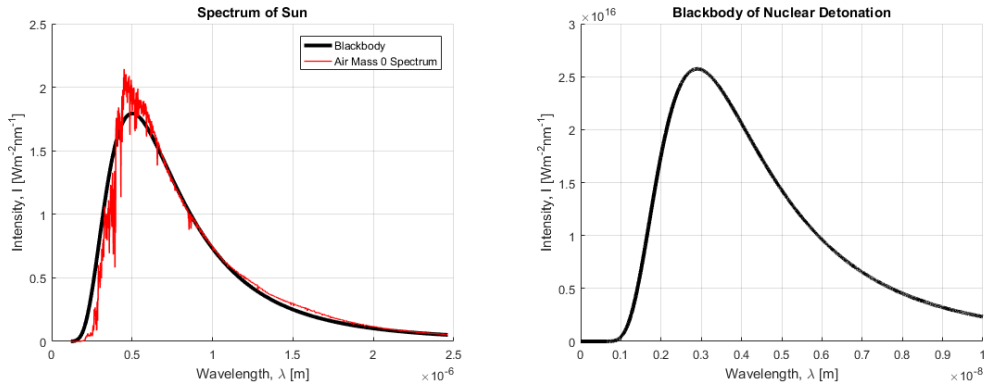

(a) **(b)**

Figure 5. Example blackbody spectra of the Sun at 5778 K (5a) and a nuclear detonation at 10^6 K (5b), estimated according to Wertz and Larson (2007). The red line in 5a is the 2000 American Society for Testing and Materials (ASTM) E-490 Air Mass 0 spectrum from the U.S. Department of Energy (DOE)/NREL/ALLIANCE, displayed to show that the Sun is not a perfect blackbody. Note that the axes are on different scales. The Sun peaks in the visible spectrum, whereas the nuclear detonation peaks in the EUV/X-rays.

The X-rays from the nuclear detonation then produce electrons through Compton scattering, bremsstrahlung radiation, the photoelectric effect, and fluorescence, whereas gamma rays will interact through Compton scattering, pair production, and the photoelectric effect. These electrons go on to create the EMP, damage electronics, create an aurora, and eventually form an artificial radiation belt.

When discussing HANDs, strategic analysts and members of the military are most concerned about the resulting electromagnetic pulse (EMP), an intense spike in electrical current and field produced by the effects of a nuclear detonation on the

environment. A pulse from a nuclear weapon detonated at high altitudes, defined as being above 30 km, can have an electric field magnitude of tens of thousands of volts per meter. This pulse propagates through the atmosphere to the ground, where it can disrupt power grids and microelectronics. Lightning and solar storms can also produce EMPs, though nuclear detonations are different in that they have three distinct EMP stages, illustrated by Figure 6.

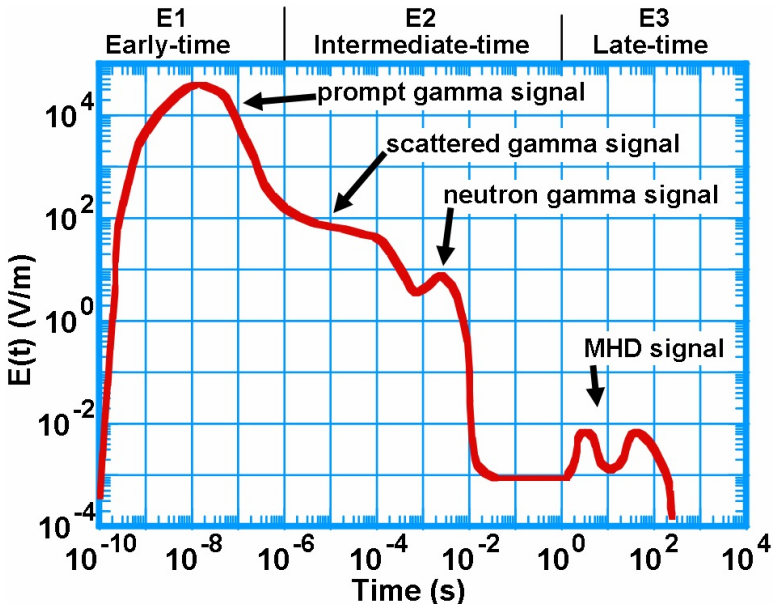

Figure 6. The EMP is divided into three main phases: E1, E2, and E3, with E3, or the MHD signal, being segmented into two separate phases. Each phase is caused by a different physical process and radiation source, and as such each phase has a distinct energy signature and timing. The graphic is courtesy of Popik et al. (2017).

Formation of the EMP.

In a high altitude nuclear detonation, a weapon will detonate at a height where the atmosphere is negligible. The gamma rays, which are emitted spherically in an exponentially rising pulse within tens of nanoseconds, disperse, with a flux on the order of:

$$F_\gamma \sim \frac{\exp^{-d/\lambda_a}}{4\pi d^2}. \tag{3}$$

where d is the distance of the observer from the detonation and λ_a is the mean free path of the gamma rays. Those gamma rays that are directed toward the Earth eventually come to interact with the atmosphere at lower altitudes, where through Compton scattering they produce Compton electrons. The region of interaction between gamma rays and atoms in the atmosphere is known as the source region. The Compton electrons produce a radial current with respect to the Earth's coordinate system. These Compton electrons are then turned by the magnetic field around Earth, turning circularly with a radius known as the gyroradius or cyclotron radius, which is inversely proportional to the magnetic field strength:

$$r_c = \frac{m_e v_\perp}{|q_e| B}, \tag{4}$$

with m_e representing the mass of the electron, q_e being the charge of the electron, $v_\perp$ the velocity of the electron perpendicular to the magnetic field direction, and B being the magnetic field. The electrons will come to a halt at the stopping distance, determined by the energy lost in collisions that produce secondary electrons. It takes 34 eV of energy to produce one electron-ion pair from these collisions after all ionization, so each Compton electron produces about 30,000 electron-ion pairs (Longmire, 1978).

E1 Phase.

The turning of these secondary electrons produces a transverse current, while the resulting electrons from the ionization process form a conducting layer that will actually serve to shield some of the effects of the EMP. The current in turn generates

an induced electric field, which propagates down to the Earth's surface as an EMP. The fields from the E1 phase are illustrated in Figure 7. This ionizes almost the entire local atmosphere, which can cause ionospheric waves and drastically affect the chemistry of the region.

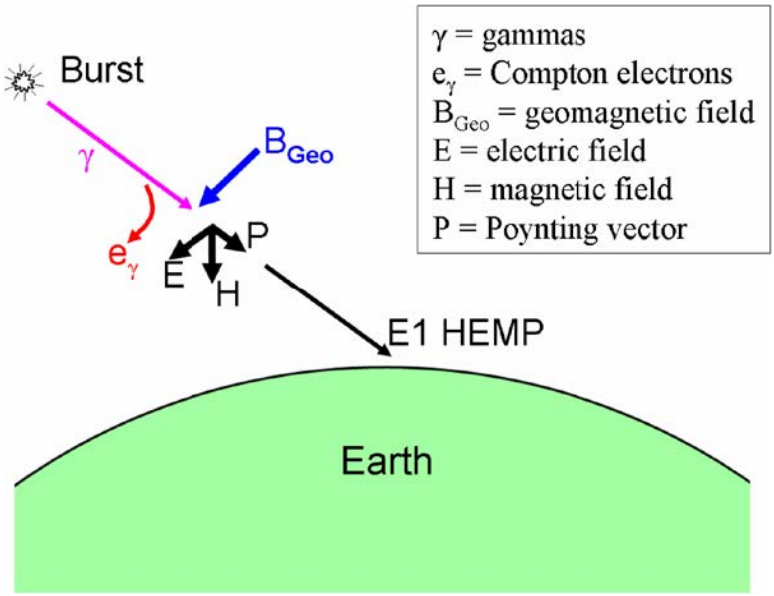

Figure 7. A simplified diagram of the E1 phase of an EMP generated by a HAND. The gamma rays start at the point of detonation and through collisions produce Compton electrons, which are turned by the geomagnetic field. The turning produces currents and electric fields. This diagram was taken from Gombosi et al. (2017).

For a high-altitude burst, the area that the EMP affects is determined by the local magnetic field direction and the altitude of the burst. Typically, the electric fields will be distorted and will follow the field lines.

E2 Phase.

Some fraction, 1/e or about 37%, of the gamma rays emitted from the detonation will interact with the atmosphere above the source region (Gombosi et al., 2017). As a result, there will be a time delay between when the prompt gamma rays arrive at the source region and when these delayed gamma rays arrive, as well as a small

discrepancy in energy. These secondary gamma rays will interact similarly to the prompt gamma rays and will Compton scatter, producing another pulse similar to that in the E1 phase. However, the E2 phase will last up to 1,000 times longer than the E1 phase, while being weaker (Popik et al., 2017). This signal is further supplemented by the current produced from high energy neutrons that escape the blast, which eventually scatter inelastically at altitudes similar to the source region and produce gamma rays, which then Compton scatter at low altitudes. This causes replacement currents in the atmosphere and in the ground, which in turn produce both vertical electric fields from the Compton scattering and horizontal electric fields from the current in the ground since the ground is an imperfect conductor.

E3 Phase.

The X-rays emitted from the detonation will also spherically diverge from the point of detonation. Roughly half of these X-rays will travel downwards towards the ground and will be absorbed by the atmosphere above the source region. These X-rays will scatter a K-shell electron out of the atmospheric atom, producing a photoelectron and a secondary X-ray from a higher-orbit electron filling the electron shell gap. The X-rays will cause an ionization cascade, which causes a heating of the higher altitude atmosphere. The heating and ionization, in turn, shields the ground from any signals from the blast region and locks in the magnetic field lines. Meanwhile, some of the fission fragments and the remaining weapon debris become highly ionized as a result of the detonation and are highly conductive as a result. The highly ionized elements are pushed upwards in altitude and push the geomagnetic field lines out of the region, creating a diamagnetic cavity. The expansion of the cavity is determined by the debris velocity and later by the altitude, eventually slowed by either atmospheric pressure or magnetic pressure. At large distances, the resulting cavity and deformation of

the field lines can be approximated as a field-aligned dipole situated at the point of detonation and thus create electric and magnetic fields that can exist for longer than E1 and E2 and cover an even wider area. This is called the blast phase, shown in Figure 8, and usually only occurs if the detonation took place above 100 km.

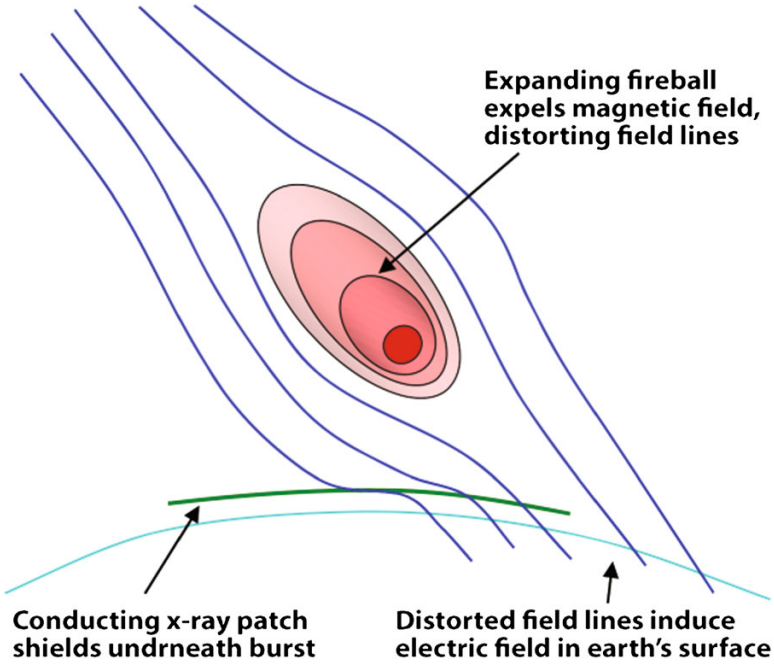

Figure 8. During the E3 phase, the X-rays released from the HAND will cause an ionization cascade and heat the atmosphere. Meanwhile, the fission fragments will be shot upwards and will push the geomagnetic field lines out, creating a diamagnetic cavity. This cavity acts as a field-aligned dipole that creates a farther-reaching effect. Figure courtesy of Gombosi et al. (2017).

The remaining debris and fission fragments, along with ions heated by the shock, travel down along the geomagnetic field lines. At altitudes under the point of detonation, the energy will be deposited similarly to other phases, and the deposition will heat and ionize the atmosphere. Typically, this will be in the E-region of the ionosphere. There is additional heating from EUV radiation. The atmosphere will first expand and then start to buoyantly rise as it becomes increasingly conductive. The rising conductive layer then crosses the geomagnetic field, inducing a current

through the dynamo effect. The current from the dynamo flows to the west, with northern and southern return currents at the edges of the buoyant region. This causes a two-cell current system that induces an electric field oriented in the same direction and propagates to the ground, as illustrated in Figure 9. This is known as the heave phase and only occurs for blasts above 150 km. It is more localized than the blast phase.

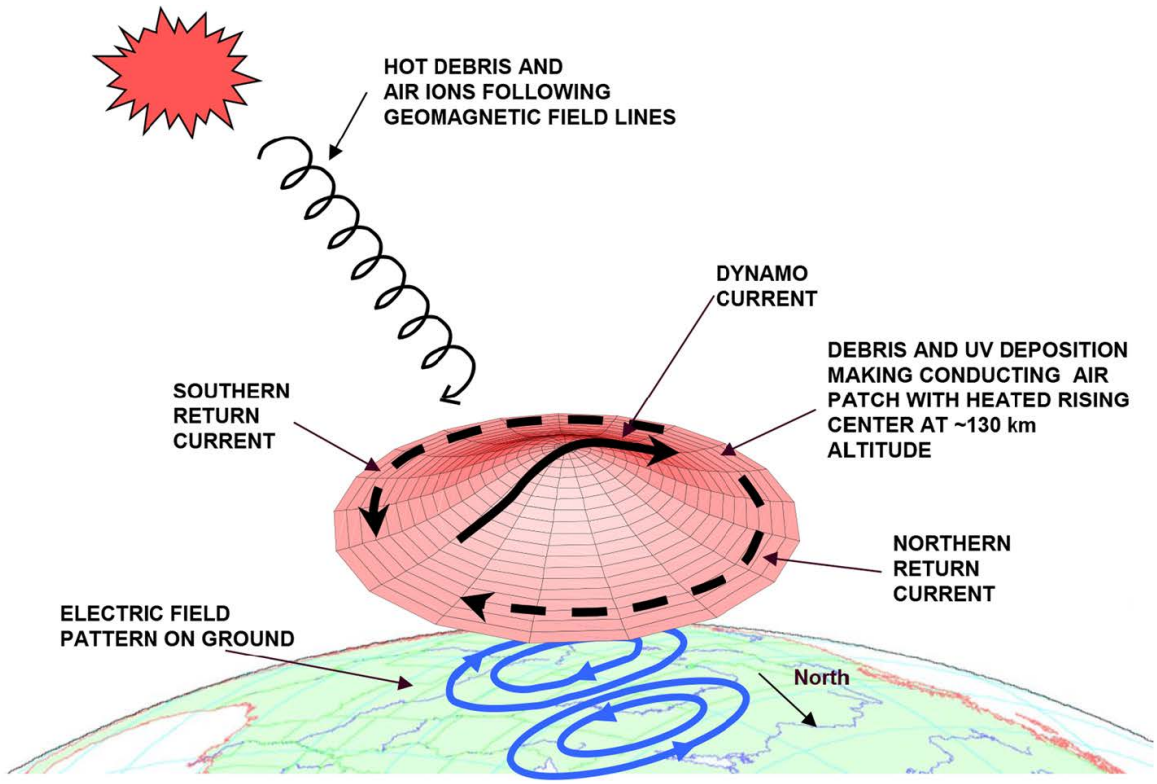

Figure 9. As the atmosphere under the HAND heats, the atmosphere will expand and then buoyantly rise. The layer will be extremely conductive. As the layer rises and crosses the geomagnetic field lines, the dynamo effect will induce a current. This image was taken from Gombosi et al. (2017).

2.3 Ionospheric Models

The ionosphere has a considerable effect on day-to-day operations on Earth. High frequency radio waves propagate by bouncing off the lower ionosphere. GPS is also

affected by the ionosphere through scintillation, refraction, dispersion, and other effects, which cumulatively are the source of the greatest error in timing and precision (Codrescu, 2007). As a consequence, many agencies are interested in developing a model of the ionosphere to forecast the changes in TEC, peak frequency of the E-layer (foE) or F_2-layer (fof2), peak electron density of the E-layer (nmE) or F_2-layer (nmF2), and peak altitude of the E-layer (hmE) or F_2-layer (hmF2). Several common models that are important historically and operationally will be discussed in the following subsections. First, however, is an overview of the solar proxies that compose some of the driving mechanisms for the ionospheric models.

2.3.1 Solar Spectrum Models

Every ionospheric model includes a solar spectrum, the photon flux at particular wavelengths drive the chemical reactions in the ionosphere. Therefore, to understand the ionospheric models, an overview of solar spectrum models must be given. There are several available reference spectra, but also variables that serve as solar activity proxy measurements.

Solar Proxies.

There are two predominant variables used as solar proxies: the radio flux at the 10.7 cm waveband, and the sunspot number. The radio flux at 10.7 cm, most commonly referred to as the $F_{10.7}$ index, is actually a flux density measured from two ground-based monitors in Canada, averaged over 1-hour periods three times daily and typically given as daily measurements (Tapping, 2013). The choice to use the 10.7 cm band was an artifact from radio communications used during World War II, but has been shown to be closely correlated to the sunspot number (Clette, 2021; Tiwari and Kumar, 2018). The $F_{10.7}$ index is measured in units of [$\times 10^{-22}$ W Hz^{-1}m^{-2}],

or solar flux units (sfu), and can be converted into a spectrum of EUV wavelengths through various empirical schemes found typically by fitting the $F_{10.7}$ index to the spectrum (Hinteregger et al., 1981), described in later sections. There have been other proposed indices based on the $F_{10.7}$ index, either in a different wavelength band (Dudok de Wit and Bruinsma, 2017) or with higher time resolution (Acebal, 2008), but the $F_{10.7}$ index is still widely used in ionospheric models to produce the EUV spectrum or in empirical calculations for the chemical reactions.

The other prominent proxy is the sunspot number. There are many various sunspot indices, including the International Sunspot Number R_I; the Zürich Sunspot Number R_Z; the 12-month running mean average of sunspots R_{12} (ITU Radiocommunication Assembly, 1999),

$$R_{12} = \frac{1}{12}[\sum_{n-5}^{n+5} R_k + \frac{1}{2}(R_{n+6} + R_{n-6})], \tag{5}$$

where R_k is the mean of daily sunspot numbers in month k, and the month is represented by k=n; and the Wolf number N_W (Berghmans et al., 2006),

$$N_w = 10N_G + N_s, \tag{6}$$

where N_G is the group sunspot count and N_s is the individual sunspot count. All the sunspot number indices rely on slightly different techniques or weighting schemes (Clette et al., 2007), though most models use either R_i or R_{12}. Typically, the sunspot number is converted to the $F_{10.7}$ index to produce the EUV spectrum since the sunspot number and $F_{10.7}$ index are approximately linearly correlated (Clette, 2021) since R_{12} is typically less than 20. There are many equations relating the two, with varying degrees of accuracy, but the recommended fit given by ITU Radiocommunication Assembly (1999) is

$$F_{10.7} = 63.7 + 0.728R_{12} + 0.00089R_{12}^2, \tag{7}$$

and the reverse is given as

$$R_{12} = \sqrt{167273 + 1123.6(F_{10.7} - 63.7)} - 408.99. \tag{8}$$

There are three other solar proxies that are used in the space weather community: the He 1083 Equivalent Width (Floyd et al., 2005), the H I Lyman-α emission line at 121.6 nm (Barth et al., 1990), and Mg II core-to-wing ratio (Viereck et al., 2001), where the He 1083 Equivalent Width, Mg II core-to-wing ratio, sunspot number, and $F_{10.7}$ index are compared in Figure 10. These proxies are not often included in ionospheric models and will not be discussed in-depth here.

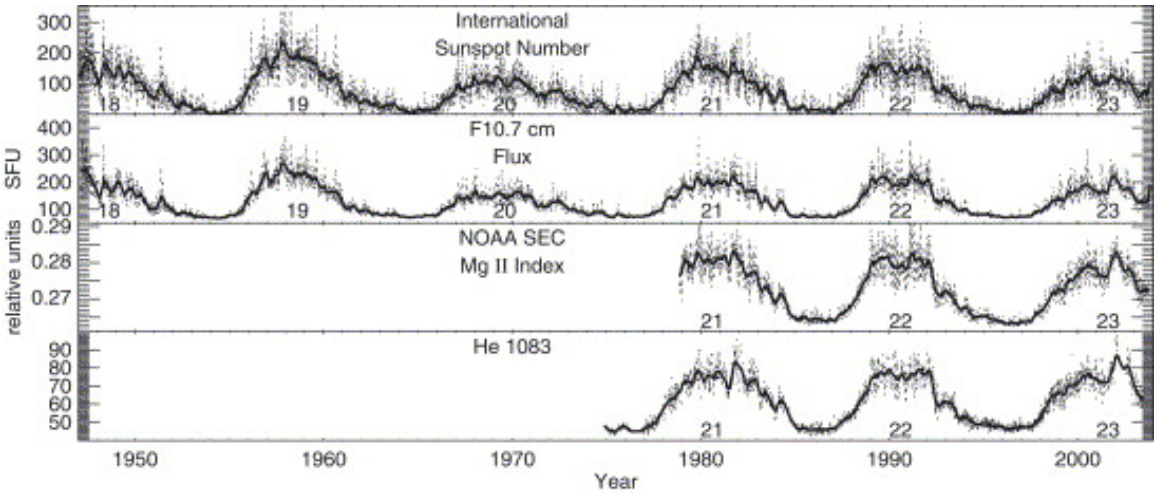

Figure 10. The international sunspot number R_i, $F_{10.7}$ index, the Mg II core-to-wing ratio, and the He 1083 Equivalent Width are compared over the solar cycles since their inception as solar proxies. These proxies are often used in space weather models and are closely correlated. Figure from Floyd et al. (2005).

The Hinteregger Method.

An early fit of the $F_{10.7}$ index to the EUV spectrum was described by Hinteregger et al. (1981). The Hinteregger method, as this method will be referred to, is an empirical model based on observations from the Atmospheric Explorer E (AE-E) satellite that uses the daily $F_{10.7}$ index and the 81-day average, $<F_{10.7}>$ to compute the irradiance in specific wavelength bins, denoted as i. The Hinteregger method finds its coefficients c_i from fitting the satellite data, and uses the F74113 reference spectrum. The irradiance is found through the calculation used by Solomon and Qian (2005)

$$I_i = F74133_i + r_1 c_{1i} + r_2 c_{2i}, \tag{9}$$

where r_1 and r_2 are given as:

$$\begin{aligned} r_1 &= 0.0138(F_{10.7} - 71.5) + 0.005(F_{10.7} - < F_{10.7} > +3.9), \\ r_2 &= 0.5943(F_{10.7} - 71.5) + 0.381(F_{10.7} - < F_{10.7} > +3.9). \end{aligned} \tag{10}$$

The reference spectrum and coefficients used in the 22-bin scheme and in the GLOW model are found in Tables 25 and 26, respectively, in Appendix A.

EUVAC.

The EUV flux model for aeronomic calculations (EUVAC) was designed to model the solar EUV flux since the Sun is not a perfect blackbody, detailed in Richards et al. (1994). This model has been incorporated into many ionospheric models to simply calculate various parameters such as ionization rates and unattenuated photoelectron fluxes. The model relies on the input of the $F_{10.7}$ index, and the 81-day average of

the $F_{10.7}$ index, $<F_{10.7}>$. The combination of these factors is combined into a simple factor,

$$P = \frac{F_{10.7} + < F_{10.7} >}{2}. \tag{11}$$

The EUVAC model uses 37 wavelength intervals from 5 nm to 105 nm, based on measurements from the EUVS instrument on the AE-E satellite (Schunk and Nagy, 2009). These intervals are associated with a modified reference flux, called F74113, and a scaling factor A for the interval, which are included in Table 27 in Appendix A.

The unattenuated flux for each interval i is empirically calculated by

$$I_i = \text{F74113}_i[1 + A_i(P - 80)]. \tag{12}$$

The model has been updated for newer measurements and newer models have been made for higher resolutions, but EUVAC remains heavily ingrained in more sophisticated ionospheric models.

FISM.

The Flare Irradiance Spectral Model Version 2 or FISM2 (Chamberlin et al., 2020, 2008) is another empirical model that has higher wavelength resolution of 1 nm and a smaller time step of 60 seconds than the other models discussed. It delivers a daily irradiance value and a flare value as products. FISM is based on measurements from the Thermosphere Ionosphere Mesosphere Energetics and Dynamics (TIMED) mission Solar EUV Experiment (SEE), SOlar Radiation & Climate Experiment (SORCE), Extreme-ultraviolet Variability Experiment (EVE), the Solar Stellar Irradiance Comparison Experiment (SOLSTICE), and the X-ray Photometer System

(XPS) in comparison to just the AE-E satellite, and is specifically tailored towards modeling flares. Data from this model can be obtained through the online FISM2 GUI (`https://lasp.colorado.edu/lisird/data/fism_flare_hr/`). FISM2 also covers more of the UV spectrum than the Hinteregger method and EUVAC, expanding from 0.1-190 nm.

This model uses calculations based on solar proxies, including the $F_{10.7}$ index, the Mg II core-to-wing ratio, and the Lyman-α emission line. The algorithm is composed of a sum of five components that begin with a basis reference spectrum for solar minimum, I_{min}, then add variations due to solar cycle (I_{SC}), solar rotation (I_{SR}), the gradual phase of the solar flare (I_{GP}), and the impulsive phase of the solar flare (I_{IP}). The daily irradiance from FISM2 as a function of day d for wavelength λ is

$$I_{daily}(d, \lambda) = I_{min}(\lambda) + I_{SC}(d, \lambda) + I_{SR}(d, \lambda) \tag{13}$$

while the flare irradiance is found as a function of time t to be

$$I_{flare}(t, \lambda) = \text{spline}[I_{daily}(d - 2 : d + 2, \lambda)] + I_{GP}(t, \lambda) + I_{IP}(t, \lambda). \tag{14}$$

The solar minimum reference spectrum is found by taking the smoothed time series over 108 days from observations from the various experimental measurements. The solar cycle irradiance component is the difference in the 108-day average irradiance and the reference spectrum,

$$I_{SC}(d, \lambda) = \frac{1}{108} \sum_{d-54}^{d+54} I(d, \lambda) - I_{min}(\lambda). \tag{15}$$

The solar cycle irradiance is found by matching a linear fit of the solar proxies ($I_{SC,P}$) to the measured irradiance due to the solar cycle ($I_{SC,M}$) at each wavelength,

$$I_{SC,M} = A_{SC}(\lambda) + B_{SC}(\lambda) I_{SC,P}, \tag{16}$$

with A and B are fitting parameters. The solar rotation irradiance is found in a similar manner, but instead is the difference between measured daily irradiance and the 108-day average,

$$I_{SR}(d, \lambda) = I(d, \lambda) - \frac{1}{108} \sum_{d-54}^{d+54} I(d, \lambda), \tag{17}$$

and again is given by a linear fit. The gradual phase irradiance relies on the Geostationary Operational Environmental Satellites (GOES) X-Ray Sensor B (XRS-B) high time cadence flare measurements $\mathrm{E}_{GP,P}$ and is split into two fits: a linear relationship for wavelengths under 6 nm,

$$I_{GP}(t, \lambda) = A_{GP}(\lambda) + B_{GP}(\lambda) I_{GP,P}(t); \tag{18}$$

and a power-law fit for wavelengths between 6-190 nm,

$$I_{GP}(t, \lambda) = A_{GP}(\lambda) + I_{GP,P}(t)^{B_{GP}}. \tag{19}$$

Finally, the impulsive phase irradiance also is given as a power-law fit, though the proxy is given as the positive time derivative of the GOES XRS-B measurements.

2.3.2 Chapman Model

The simplest model of the ionosphere is the Chapman model. Developed by Sydney Chapman in 1931 (Chapman, 1931), this model assumes monochromatic light is entering a plane-parallel atmosphere of one absorbing species at an angle less than about 85°, depicted in Figure 11. It also assumes that the concentration of the

absorbing species varies with altitude by a constant characteristic length, known as the scale height, H, and that the species has an absorbing cross section, σ_a that is independent of altitude. From Schunk and Nagy (2009), letting n be the number density of the absorbing species at an altitude z and χ be the solar zenith angle measured from the vertical, the neutral number density is defined as

$$n(z) = n(z_0) \exp[-\frac{(z - z_0)}{H}], \tag{20}$$

where z_0 is an arbitrary reference height. If m is the mean mass of a molecule of the absorbing species, T is the temperature of the absorbing species, and g is the acceleration due to gravity, and assuming that temperature and gravitational acceleration do not noticeably change with altitude, then the scale height H for the absorbing species is

$$H_s = \frac{kT}{mg}. \tag{21}$$

Finally, denoting the unattenuated photon flux at the top of the ionosphere as I_∞, the photon flux at an altitude z can be written as

$$I(z, \chi) = I_\infty \exp[-Hn(z)\sigma_a \sec \chi]. \tag{22}$$

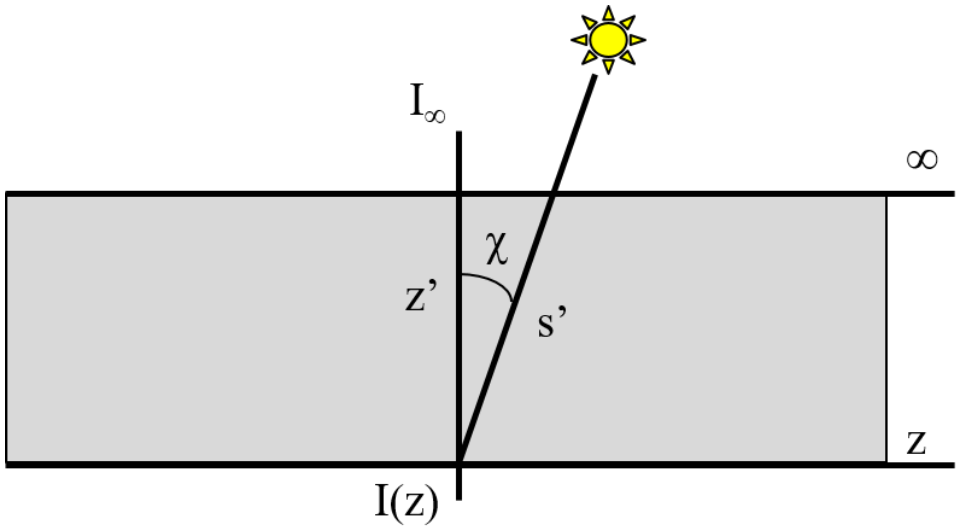

Figure 11. This is a simplified illustration of the Chapman model for the ionosphere. This assumes a source at an altitude of infinity above the surface with one species and monochromatic light. The unattenuated photon flux, described as the photon flux at infinite altitude, is I_∞, while at an altitude z it is $I(z)$. The photons travel along a path of length s', with a vertical distance of z' and a solar zenith angle of χ.

However, this equation does not take into consideration that the there is a wavelength dependence for the absorption cross section and the unattenuated photon flux. It also does not consider multiple species (denoted by s) or the inherent dependence of temperature and gravitational acceleration on altitude. Taking this into consideration, the new equations for scale height, number density, and photon flux are:

$$H_s(z) = \frac{kT_s(z)}{m_s g(z)} \tag{23}$$

$$n_s(z) = n_s(z_0)\exp[\frac{T_s(z_0)}{T_s(z)}]\exp[-\int_{z_0}^{z}\frac{dz*}{H_s(z*)}] \tag{24}$$

$$I(z,\lambda,\chi) = I_\infty(\lambda)\exp[-\int_{\infty}^{z}\sum_s n_s(z)\sigma_s^a(\lambda)ds'], \tag{25}$$

where s' is the optical path of the photons. This leads to a common parameter known as the optical depth, τ:

$$\tau(z, \lambda, \chi) = \int_{\infty}^{z} \sum_{s} n_s(z) \sigma_s^a(\lambda) ds'. \tag{26}$$

With the probability of the absorption of a photon that results in an ion-electron pair symbolized as η, the Chapman production function to describe the rate of production of electrons P_c is thus written as

$$P_c(z, \chi) = I_\infty \eta \sigma_a n(z) \exp[-Hn(z)\sigma_a \sec \chi]. \tag{27}$$

The peak production rate can be found through differentiation, and the altitude of the maximum $z_{\max}$ and the maximum production rate are found to be

$$z_{\max} = z_0 + H \log[n(z_0) H \sigma_a \sec \chi], \tag{28}$$

$$P_c(z_{\max}, \chi) = \frac{I_\infty \eta \cos \chi}{H} e^{-1}. \tag{29}$$

Although the Chapman model is fairly basic, it does work as an approximation for the E-layer and the F_1-layer, but fails for the D-layer and F_2-layer, as the D-layer is dominated by chemical processes, specifically concerning negative ions, and the F_2-layer is dominated by transport mechanisms. Most ionospheric models build off this simple model and add complexity, including having several absorbing species, higher moments of the transport equation, temperatures influenced by chemical reactions, and electromagnetic interactions.

2.3.3 Quick-Run Models

Slightly more complex than the Chapman model are the quick-run models of the ionosphere. These models are designed to be computationally inexpensive and are empirically-based climatological models. The most common such models, are the International Reference Ionosphere (IRI) and NeQuick, both three-dimensional, time dependent models. Specific details are further explained in documentation by Bilitza (1990) for the IRI and European Commission (2016) for NeQuick.

The IRI is the standard accepted model for the ionosphere, sponsored by the Committee on Space Research (COSPAR) and the International Union of Radio Science (URSI). It is composed of empirical calculations using data assimilation schemes to collect current and historical data from the worldwide network of ionosondes, incoherent scatter radars, topside sounders, Global Navigation Satellite Systems (GNSS), and *in situ* measurement devices from sounding rockets and satellites (Bilitza, 2018). IRI provides monthly averages for electron density, electron temperature, ion composition, and ion temperature, but requires position of interest, time, solar indices of either $F_{10.7}$ or sunspot number, ionospheric index of the ionosonde-based IG index 12-month running mean, and the Ap index. However, if a past date is provided to IRI, it can automatically look up the parameters needed. The altitude range is from approximately 80 km to 2,000 km.

NeQuick was developed by the Aeronomy and Radiopropagation Laboratory, now T/ICT4D Laboratory, of the Abdus Salam International Centre for Theoretical Physics in Trieste, Italy, with the collaboration of the Institute for Geophysics, Astrophysics and Meteorology of the University of Graz in Austria, and is now in its second iteration. The description of the new version (Nava et al., 2008) uses a modified G. Di Giovanni and S. M. Radicella (DGR) model for the profile from 90 km up to the F_2-layer peak, which includes five semi-Epstein layers. The bottomside and

topside of the ionosphere are determined by different modeled semi-Epstein layers. The topside of the model can extend up into the Van Allen radiation belts, extending to 25,000 km, but NeQuick does not consider the interactions of the magnetosphere or radiation belts. The model requires the inputs of position of interest, time, and either the $F_{10.7}$ value or the sunspot number, which can be computed empirically from the $F_{10.7}$ index. It outputs the electron number density as a function of altitude.

2.3.4 Full-Physics Models

The most physically robust models for forecasting and research are the full-physics models, which rely on numerical schemes to solve the Boltzmann equation or its moment approximations, along with the field equations for the electrodynamics of the ionosphere. A few of these models also incorporate data assimilation features, but for the most part rely completely on their internal codes to develop a global, three-dimensional, time-dependent model of the ionosphere.

USU-GAIM.

Utah State University's Global Assimilation of Ionospheric Measurements (USU-GAIM) is a data assimilation model of the ionosphere built upon the physics-based Ionosphere Forecast Model. From Zhu et al. (2006), the Ionosphere Forecast Model is a three-dimensional, high-resolution, multi-ion global model that can extend from 90 km to 1,600 km in altitude, with the vertical profiles being variable in refinement. Its spatial resolution is variable, but the finest resolution is 2° latitude and 5° longitude. The temporal resolution is also variable, being able to scale down to 5 minute increments. The Ionosphere Forecast Model numerically solves the equations for continuity, momentum, and energy for multiple ion species along magnetic field lines for plasma flux tubes. It focuses on five ion species: NO^+, O_2^+, N_2^+, O^+, and

H^+. It also includes processes for field-aligned diffusion, cross-field electrodynamic drifts, thermospheric wind, compositional changes, energy-dependent chemical reactions, ion production from EUV and from auroral precipitation, thermal conduction, diffusion-thermal heat flow, local heating and cooling effects, and pole displacement. The model requires the inputs of neutral composition, neutral wind, the $\vec{E} \times \vec{B}$ field, EUV radiation, and precipitation and convection at latitudes greater than $\pm 60°$. Specifically, according to the CCMC, it requires the $F_{10.7}$ index, the 81-day average of the $F_{10.7}$ index, the daily Ap index, and eight 3-hour Kp indices. Outputs include three-dimensional number density distributions of the ions and electrons, ion and electron temperatures, TEC, nmE, nmF2, hmE, and hmF2, plus other additional plasma parameters.

GAIM, which builds off of the physics-based model, comes in two different packages: GAIM Gauss-Markov (GAIM-GM) and GAIM Full Physics (GAIM-FP). GAIM-FP has evolved to use the Ionosphere-Plasmasphere Model instead of the IFM, but both use a Kalman filter for the data assimilation. Currently, GAIM-GM is employed both at the USAF 557^{th} Weather Wing and at NASA's CCMC. Due to the availability of GAIM-GM over GAIM-FP, GAIM-FP will not be discussed here despite it being the only current model looking to incorporate D-layer chemistry. According to the working paper by Scherliess et al. (2017), GAIM-GM uses various ionospheric measurements to correct the predictions of the Ionosphere Forecast Model, using the Kalman filter techniques to incorporate the data and the Gauss-Markov process to evolve the deviations and error covariances over time. It is limited in altitude to between 92 km and 1,400 km, with a set vertical resolution of 4 km in the E-layer and 20 km in the F-layer and above. The global resolution is also less refined than the Ionosphere Forecast Model, with 4.6° resolution in latitude and 15° resolution in longitude. When run on the CCMC, the only input parameters necessary are the

start date for the time of interest and the duration, as the other parameters are looked for automatically through available databases.

GITM.

The University of Michigan also developed a physics-based model of the ionosphere, the Global Ionosphere-Thermosphere Model, or GITM, which is detailed in Ridley et al. (2006). This model uses a stretched three-dimensional spherical grid, where the longitude resolution is fixed but the latitude and altitude resolution can be non-uniform. It is also different from other ionospheric models as it uses an altitude-based vertical grid based on scale height instead of a pressure-based vertical grid that other models use. It also does not assume hydrostatic equilibrium when solving the dynamics equations, solves for advection and chemistry explicitly, and includes nine neutral species (O, O_2, N(^{2}D), N(^{2}P), N(^{4}S), N_2, NO, H, and He) and nine ion species (O^+(^{4}S), O^+(^{2}D),O^+(^{2}P), O_2^+, N^+, N_2^+, NO^+, H^+, and He^+). It also has the option to incorporate the International Geomagnetic Reference Field (IGRF) model for variable magnetic fields, and GITM is further coupled to many high-latitude ionospheric electrodynamic models that can be chosen depending on the system of interest, and it has options for data assimilation. Of note is that heating in GITM is determined by solar and Joule heating, and heat from excitation is not calculated. The model available on the CCMC has a longitudinal resolution of 5° and a latitudinal resolution of 2.5°, and an altitude range between 90 km and 600 km. Similar to other models, it requires an input for the $F_{10.7}$ index but not the 81-day average, as well as needing the hemispheric power index (HPI), interplanetary magnetic field (IMF) parameters, and solar wind velocity. In return, it outputs neutral wind velocity, temperature, number density, and mass density; ion temperature and number density; electron temperature and number density; and plasma velocity.

SAMI3.

The cleverly-named Sami3 is Also a Model of the Ionosphere (SAMI3) was developed at the Naval Research Laboratory as a three-dimensional physics-based ionospheric model, based on SAMI2 (Sami2 is Also a Model of the Ionosphere), which was a two-dimensional model. Its strength is in its chemical calculations; according to Huba et al. (2017), SAMI3 models the plasma and chemical evolution of seven ion species: NO^+, O_2^+, N_2^+, O^+, N^+, H^+, and He^+. This includes twenty-one chemical reactions and radiative recombinations. It solves temperature equations for electrons and the H^+, He^+, and O^+ ions. It also includes ion inertia in the ion momentum equations along the magnetic field, and it uses the $\vec{E} \times \vec{B}$ drift for transverse motion. It has an altitude range of 85 km to 20,000 km, but since the ionosphere is calculated as a complete flux tube, is latitudinally limited to between $\pm 62.5^\circ$ about the magnetic equator. The CCMC cites that the neutral composition and temperature are determined from the empirical NRLMSISE-00 (Naval Research Laboratory, mass spectrometer and incoherent scatter radar, extending through the exosphere, released in 2000) model while the neutral winds are from the empirical Horizontal Wind Models (HWMs). The model requires the $F_{10.7}$ index and the 81-day average $F_{10.7}$ index, the Ap index, and the $\vec{E} \times \vec{B}$ drift velocity. It outputs the ion density, temperature, and velocity; the electron density and temperature; TEC; nmF2; and hmF2. It also has options for incorporation into models like TIE-GCM.

TIE-GCM.

The last model is the Thermosphere-Ionosphere-Electrodynamics General Circulation Model (TIE-GCM) developed at the High Altitude Observatory (HAO) at the National Center for Atmospheric Research (NCAR). This model is a three-dimensional physics-based ionospheric model with options for data assimilation. It

focuses on the coupling of the thermosphere and ionosphere and the self-consistent solutions of the low-latitude electric fields, further detailed in Qian et al. (2013). For high latitudes, it relies on either the Heelis potential or the Weimer empirical potential. To solve the equations of continuity, momentum, and energy, it uses explicit fourth-order centered finite difference for the horizontal component. It also employs a Shapiro filter to smooth the solutions. It includes the evolution of five neutral species (NO, N(^{4}S), N(^{2}D), O, and O_2) with an option for He and with CO_2 being specified through diffusive equilibrium (Foster, 2016), and it includes calculations for five ion species: O^+, O_2^+, N_2^+, NO^+, and N^+. TIE-GCM has multiple options for auroral forcing to drive the polar layers; various options for the magnetic field parameters, including using the IGRF model; and options for solar forcing, making it highly versatile. Since the model is based on a pressure grid, its altitude range is dependent on solar conditions but is typically between 97 km and 700 km. The longitudinal and latitudinal resolutions are 5°, but this can be refined to 2.5°. It requires an input of the $F_{10.7}$ index, the 81-day average $F_{10.7}$ index, the 3-hour Kp index, and specifications for either the Heelis or Weimer potential. It can produce outputs for ion and electron number densities; neutral mass-mixing ratios; ion, neutral, and electron temperatures; neutral wind velocities; pressure surfaces; and electric potential.

2.3.5 GLOW

In contrast to the other models discussed above, the GLobal airglOW (GLOW) model is a toolkit of functions for analysis on the results of the ionosphere models to calculate optical emissions and spectral features, developed by the HAO at NCAR under the University Corporation for Atmospheric Research (UCAR) and detailed in Solomon (2018, 2017). It is designed to accept input from TIE-GCM and its counterpart, the Thermosphere-Ionosphere-Mesosphere-Electrodynamics General

Circulation Model (TIME-GCM), but also can accept input from empirical models like IRI and the NRLMSISE-00, which are included in the code package. It is a one-dimensional, single-column, single-time model that must be repeatedly run to build a three-dimensional, time-dependent model. It requires solar irradiance as an input, usually calculated from EUVAC and other ultraviolet models internally (Solomon, 2017), but it can also use a given measured solar flux. GLOW does not calculate neutral gas concentrations for O, O_2, N_2, NO, and N(^{4}S), or neutral, ion, and electron temperatures, so these must be provided as inputs manually or from the ionosphere models. Electron densities for the F-layer above 200 km are also not calculated and therefore an electron density profile must be provided, making this model ideal for bottomside ionosphere calculations. The auroral electron flux can also be provided or calculated based on the given parameters. In return, the model recalculates the electron density below 200 km, the ionized and excited species densities, airglow volume emission rates, and vertical column brightness, along with all the intermediate quantities used to calculate these. It solves the Boltzmann equation for energetic electrons and finds the electron heating rate as well.

2.4 Ray Tracing Algorithm

A common method to model the path of a radar signal is to use a ray tracing algorithm. This simplifies the problem by visualizing the signal as a ray instead of a wave and computing the reflection of the ray off the ionosphere and back to the ground. The ray tracing algorithm in this research was developed by Eugene Dao at the Air Force Research Laboratory (AFRL) (Dao et al., 2016) from a modified version of the Jones-Stephenson code (Jones and Stephenson, 1975). This code computes the path of the ray by first computing the index of refraction, n, from the Appleton-

Hartree equations:

$$n^2 = 1 - 2X\frac{1 - iZ - X}{2(1 - iZ)(1 - iZ - X) - Y_T^2 \pm \sqrt{Y_T^4 + 4Y_L^2(1 - iZ - X)^2}}, \tag{30}$$

where:

$$X = \frac{f_N^2}{f^2}, \tag{31}$$

$$Z = \frac{\nu}{2\pi f}, \tag{32}$$

$$Y_T = Y \sin\psi, \tag{33}$$

$$Y_L = Y \cos\psi, \tag{34}$$

$$Y = \frac{f_g}{f}, \tag{35}$$

f_N is the plasma or electron frequency, f_g is the electron gyrofrequency, ν is the electron collision frequency, f is the wave or signal frequency, and ψ is the angle between the normal of the wave and the Earth's magnetic field. The electron gyrofrequency is calculated as

$$\omega_g = \frac{q_e B}{m_e}, \tag{36}$$

with q_e as the electron charge, B as the Earth's magnetic field, and m_e being the electron mass. The AFRL version uses updated IGRF coefficients to calculate the

gyrofrequency and other portions of the ray tracing algorithm. Taking the positive component corresponds to the ordinary or O-mode, while the negative component is related to the extraordinary or X-mode.

The ray tracing algorithm solves the Hamiltonian equations, using the group path $P' = ct$ as an independent variable. The Hamiltonian equations used by Jones and Stephenson (1975) are in spherical coordinates and are given as:

$$\frac{dr}{dP'} = -\frac{1}{c}\frac{\partial H/\partial k_r}{\partial H/\partial \omega}; \tag{37}$$

$$\frac{d\theta}{dP'} = -\frac{1}{rc}\frac{\partial H/\partial k_\theta}{\partial H/\partial \omega}; \tag{38}$$

$$\frac{d\phi}{dP'} = -\frac{1}{rc\sin\theta}\frac{\partial H/\partial k_\phi}{\partial H/\partial \omega}; \tag{39}$$

$$\frac{dk_r}{dP'} = -\frac{1}{c}\frac{\partial H/\partial r}{\partial H/\partial \omega} + k_\theta\frac{d\theta}{dP'} + k_\phi \sin\theta\frac{d\phi}{dP'}; \tag{40}$$

$$\frac{dk_\theta}{dP'} = \frac{1}{r}(\frac{1}{c}\frac{\partial H/\partial \theta}{\partial H/\partial \omega} - k_\theta\frac{dr}{dP'} + k_\phi r\cos\theta\frac{d\phi}{dP'}); \tag{41}$$

$$\frac{dk_\phi}{dP'} = \frac{1}{r\sin\theta}(\frac{1}{c}\frac{\partial H/\partial \phi}{\partial H/\partial \omega} - k_\phi \sin\theta\frac{dr}{dP'} - k_\phi r\cos\theta\frac{d\theta}{dP'}); \tag{42}$$

where H represents the Hamiltonian; k_r, k_θ, and k_ϕ are the components of the propagation vector in spherical coordinates; and ω is the angular frequency, $2\pi f$. The Hamiltonian has different forms depending on if the magnetic field is included and if collisions are included.

The ray tracing algorithm produces the group path, group delay, azimuth angle, and elevation angle. An example is given in Figure 12 from Burg (2020), where the

top left plot is the longitudinal variation, the top right is the latitudinal variation, the bottom left is the top-down view of the ray path, and the bottom right is the electron frequency profile. The gradient is the electron frequency.

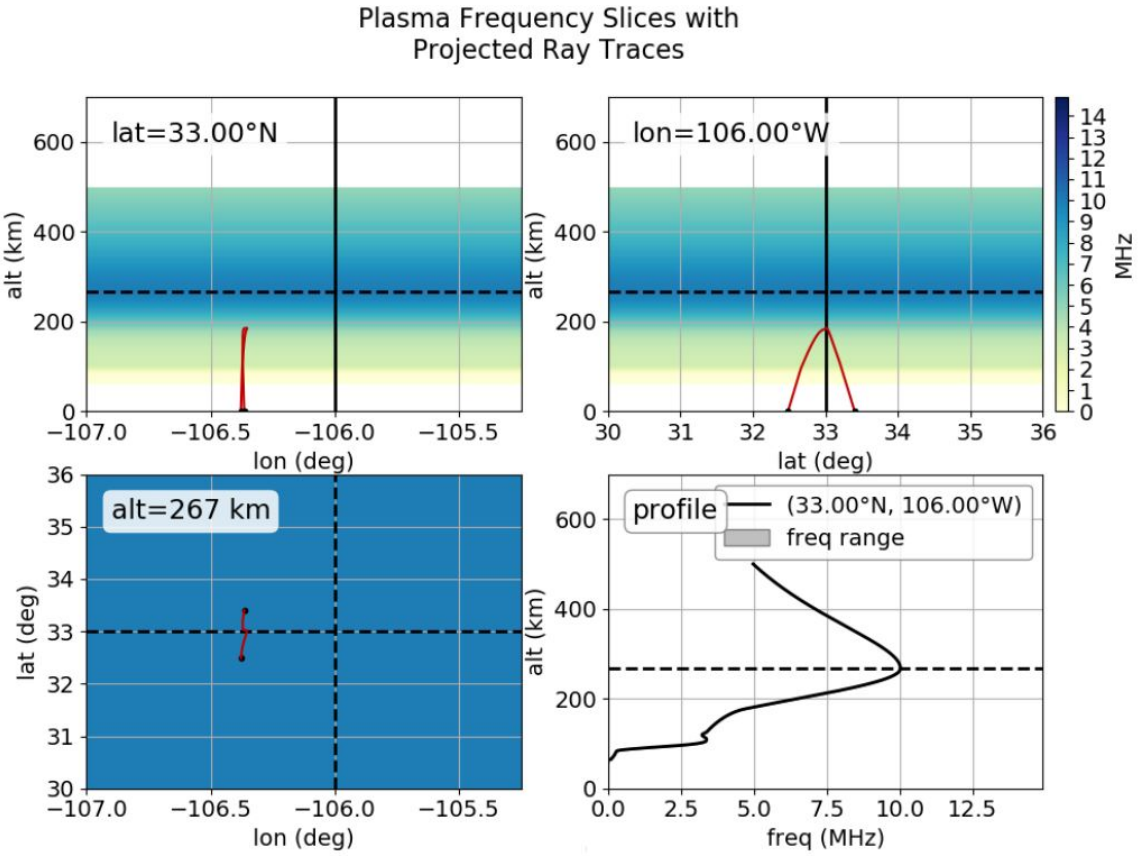

Figure 12. An example of the ray trace produced from the algorithm. The top left is the longitudinal variation, the top right is the latitudinal variation, the bottom left is the top-down view, and the bottom right is the electron frequency profile. Figure courtesy of Burg (2020) using the ray tracing algorithm from Dao et al. (2016).

While Jones and Stephenson (1975) and Dao et al. (2016) did internal validations for their algorithms, additional studies were conducted in Burg (2020) and Chakraborty (2021), where the latter focuses on solar flares as well.

III. Solar Flare Analysis

Overview

The first objective of this research is to examine the electron density profiles before and during a flare. These electron densities will form the input for the ray tracing algorithm in Chapter IV. Meanwhile, the modeled profiles are examined to determine the flare impacts on the profile by analyzing the peak frequency and peak altitude of the E-region.

3.1 Methodology

First, solar flares using an existing ionospheric model were analyzed, but with varying solar spectra to inform the chemistry and excitation.

3.1.1 Solar Flare Selection

Between 1 January 2003 and 31 December 2016, there were a total of 34 X-class flares, 1,084 M-class flares, 8,760 C-class flares, and 8,048 B-class flares. However, not all of the flares have usable data, so the data must be narrowed to a smaller selection.

The flares were found using the GOES x-ray flux database (`https://www.ngdc.noaa.gov/stp/space-weather/solar-data/solar-features/solar-flares/x-rays/goes/xrs/`), which contains all X-ray spikes recorded by the SWPC GOES X-ray satellite between 1 January 2003 and 31 December 2016. The data was cross-referenced using the Harvard integrated solar flare database (Angryk et al., 2020) that contains flares between 1 May 2010 and 29 December 2018.

The location for data collection was chosen to be Millstone Hill, Massachusetts, which contains an ionosonde for electron frequency profiles and a CODAR array with two transmitting sites; it is also well-known for its incoherent scatter radar. The

CODAR array used for the IARPA HFGeo Long Term Collect project (Ginet et al., 2018) was used for the ray tracing application in Chapter IV. The Millstone Hill ionosonde is located at 42.503° latitude and 288.765° longitude (Reinisch and Galkin, 2011).

Since the excess EUV and x-ray photons from the solar flares only impact the dayside and much of the D-layer, E-layer, and F_1-layer dissipate at night, only flares taking place during daylight were selected. To do this, the zenith angle was restricted to be less than 75°. The zenith angle was calculated using a MATLAB function written by Roy (2004) based on the solar position algorithm developed by Reda and Andreas (2005).

Further, not all the flares are strong enough to elicit an enhancement in electrons in the ionosphere that can be noticeable in the instruments or code, and some are too strong and cause blackouts in the instruments. For these reasons, all B- and C-class flares were eliminated completely, since they cannot produce enough enhancement to detect. Therefore, only M- and X-class flares were considered. Using the GIRO DIDBase (Reinisch and Galkin, 2011), the ionograms for each flare were analyzed for instrument blackout, starting from the beginning of the hour before the peak and ending at the beginning of the hour after the peak; for example, an M-class flare on 21 August 2015 with a peak time of 2034 UTC would be analyzed from 1900 UTC to 2100 UTC. This would capture the start of the flare for all in order to analyze both pre-flare and peak flare conditions.

Restricting to only flares taking place during the time period the CSTM transmitter was active, it was found that there were no X-class flares and 14 M-class flares. Instead, the X-class flare time period was expanded to the entire range of the GOES data, where there were 14 X-class flares that met the criteria.

3.1.2 Solar Flare Modeling

After the flares were selected, a model was chosen to produce electron frequency profiles for the same two hour period around the flare that was observed with the ionograms. GLOW was chosen for several reasons: it runs faster than full-physics models, it is built on IRI, it does an adequate job of simulating the relevant physics in the ionospheric layers where M- and X-class flares have the most effect, and it has the ability to use an user-generated solar spectrum for its calculations instead of a common scheme like EUVAC, though it can also use EUVAC or the Hinteregger method. This model typically uses the IRI as a starting basis to calculate starting parameters including the electron frequency profile, then recalculates electron, excited, and neutral densities as well as airglow emission rates for a single column at a single location for a single time. It requires a latitude and longitude, date and time UTC, daily $F_{10.7}$ index, the previous day's $F_{10.7}$ index, an 81-day average $F_{10.7}$ index, and the Ap index to run the calculations.

The $F_{10.7}$ index and its averages were taken from the database hosted by The Solar Radio Monitoring Program, operated jointly by the National Research Council Canada and Natural Resources Canada with support from the Canadian Space Agency (Tapping, 2013) or on the client (`https://lasp.colorado.edu/lisird/data/penticton_radio_flux/`). This data has a cadence of 24 hours between 1 January 1947 to present day. The Ap index was found through a host run by the GFZ German Research Centre for Geosciences (`https://www.gfz-potsdam.de/en/kp-index/`), or the OMNI client King and Papitashvili (2005) (`https://omniweb.gsfc.nasa.gov`). The Ap index is a magnetic parameter derivative of the Kp index, and defined as the earliest maximum value taken from an average of eight indices over a 24-hour period. The inputs for the chosen flares were formatted into a text file as described in Table 28, while the parameters for the chosen flares are found in Tables

2 and 3 for M-class flares and X-class flares respectively.

Table 2. The parameters and characteristics for the select M-class flares. Included are the date in the format DD-MM-YYYY, start time, peak time, peak flare intensity, $F_{10.7}$ index, and Ap index.

Date	**Start Time** (UTC)	**Peak Time** (UTC)	**Flare Intensity** [10^{-5}W/m^2]	**$F_{10.7}$ index** [sfu]	**Ap index**
21-6-2015	1810	1820	1.1	130.1	7
3-7-2015	1247	1251	1.5	113.0	2
6-7-2015	2032	2040	1.7	132.5	10
21-8-2015	1910	2034	1.1	117.0	5
22-8-2015	2119	2124	3.5	122.3	8
1-10-2015	1303	1310	4.5	117.4	10
2-10-2015	1219	1226	1.0	106.6	12
2-10-2015	1708	1718	1.0	104.4	12
17-10-2015	2009	2023	1.1	118.2	10
31-10-2015	1748	1752	1.0	116.1	6
4-11-2015	1331	1352	3.7	113.8	30
9-11-2015	1249	1312	3.9	108.0	25
13-2-2016	1516	1524	1.8	110.8	7
14-2-2016	1918	1926	1.0	108.7	9

Table 3. The parameters and characteristics for the select X-class flares. Included are the date, start time, peak time, peak flare intensity, $F_{10.7}$ index, and Ap index.

Date	**Start Time** (UTC)	**Peak Time** (UTC)	**Flare Intensity** [10^{-4}W/m^2]	**$F_{10.7}$ index** [sfu]	**Ap index**
17-3-2003	1850	1905	1.5	135.2	42
9-6-2003	2131	2139	1.7	178.4	28
23-10-2003	1950	2004	1.1	201.6	6
26-10-2003	1721	1819	1.2	267.9	10
2-11-2003	1703	1725	8.3	260.8	18
13-8-2004	1807	1812	1.0	145.1	6
7-11-2004	1542	1606	2.0	137.6	50
27-1-2012	1737	1837	1.7	167.3	7
7-1-2014	1804	1832	1.2	306.0	7
29-3-2014	1735	1748	1.0	145.8	7
10-6-2014	1136	1142	2.2	166.9	6
22-10-2014	1402	1428	1.6	209.9	13
25-10-2014	1655	1708	1.0	225.4	9
5-5-2015	2205	2211	2.7	135.6	5

GLOW has the ability to use a user-supplied solar spectrum that must be provided as a text file within the GLOW file architecture. The user-supplied spectrum was taken from FISM2, the Flare Integrated Spectral Model Version 2 Chamberlin et al. (2020). FISM2 provides the solar irradiance at 1 AU over a cadence of 60 seconds for every 0.1 nm between 0 and 190 nm for all times going back to 1981 (`https://lasp.colorado.edu/lisird/data/fism_flare_hr/`). The FISM2 data was sorted in the 123 bins used in the supplied flux file for each of the 120 minutes over the span of the flare.

GLOW was run for each minute for every flare for all three solar spectrum schemes - the Hinteregger method, EUVAC, and the user-supplied scheme, which will be referenced as FISM. Then, all three were averaged together, referred to as the spectral composite. This served to reduce the potential for outliers in the electron frequency

profiles, but also gave more weight to the less temporally variable spectral models. IRI electron frequency profiles can also be extracted from the GLOW subroutines as IRI is included in the code package, so all five profiles were compared to the ionograms used to check for blackout. These ionograms, while examined for blackout, were also hand-scaled using the SAO Explorer and ARTIST5 software (Galkin et al., 2008) to provide the ground-based electron frequency profiles. The electron frequency profiles derived from the ionograms are considered to be the observed ionospheric conditions.

3.1.3 Comparisons and Statistics

The comparison between models and the ionograms are made during the start times of the flares and peak times of the flares. Instead of contrasting the full electron frequency profiles, the peak altitude of the E-layer (hmE) and peak frequency of the E-layer (foE) were compared, since GLOW is only valid up to 200 km, restricting it to the E-layer and F_1-layer. GLOW can be run for any time, but the ionograms have a cadence between 5 minutes and 15 mintues, so all ionograms were interpolated in time using a cubic spline to match the start and peak flare times. The difference between the models and the ionograms are compared using the root-mean-squared (RMS) and prediction efficiency (PE), or forecast, skill scores (Shim et al., 2012). The RMS is calculated as:

$$RMS = \sqrt{\frac{\sum_{i=1}^{N}(x_{obs_i} - x_{model_i})^2}{N}}, \tag{43}$$

where x_{obs} is the observed value from the ionosonde, x_{model} is the value calculated from the specific model, and N is the total number of values in either data set. The PE is derived from the RMS, but using the mean of the observed data $< x_{obs} >$:

$$PE = 1 - \sqrt{\frac{\sum_{i=1}^{N}(x_{obs_i} - x_{model_i})^2}{\sum_{i=1}^{N}(x_{obs_i} - < x_{obs} >)^2}} = 1 - \frac{RMS_{model}}{RMS_{obs}}. \quad (44)$$

A PE of 1 indicates perfect agreement between the model and the data; a PE of 0 indicates the model prediction is comparable to the variance of the data around the mean value; a PE of less than 0 indicates that the mean of the data is a better prediction than the model.

3.2 Results

3.2.1 Example Case Study

The FISM spectra from the start and peak flare times were compared first. Since the resolution for FISM is 1 nm, the 123 bins used for GLOW were included to show the full difference between times and are referred to as "GLOW FISM" in the figures. The greatest difference in the flux occurs at the lower wavelengths in the X-ray regime, in some bins with an enhancement over an order of magnitude. The difference in fluxes are similar between all flares, so an example M-class flare was chosen to demonstrate the difference in Figure 13. The example flare occurred on 13 February 2016, starting at 1516 UTC and peaking at 1524 UTC. To show the difference in fluxes between M- and X-class, an example X-class flare was also analyzed as shown in Figure 14, peaking at 1606 UTC on 11 July 2004 and showing a difference of up to two orders of magnitude in the X-ray regime and a larger difference past 10 Å. The flux for the bins are a weighted sum of the fluxes in the wavelength bins, which gives greater emphasis to smaller wavelengths.

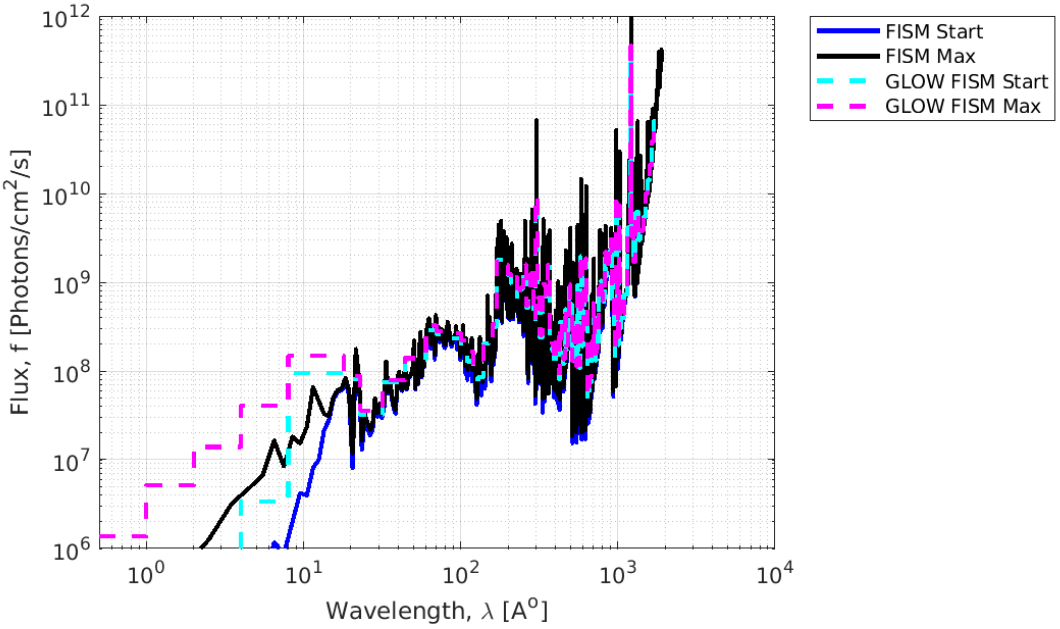

Figure 13. FISM solar spectrum at start and peak of flare for an example M-class flare with a peak at 1524 UTC on 13 February 2016.

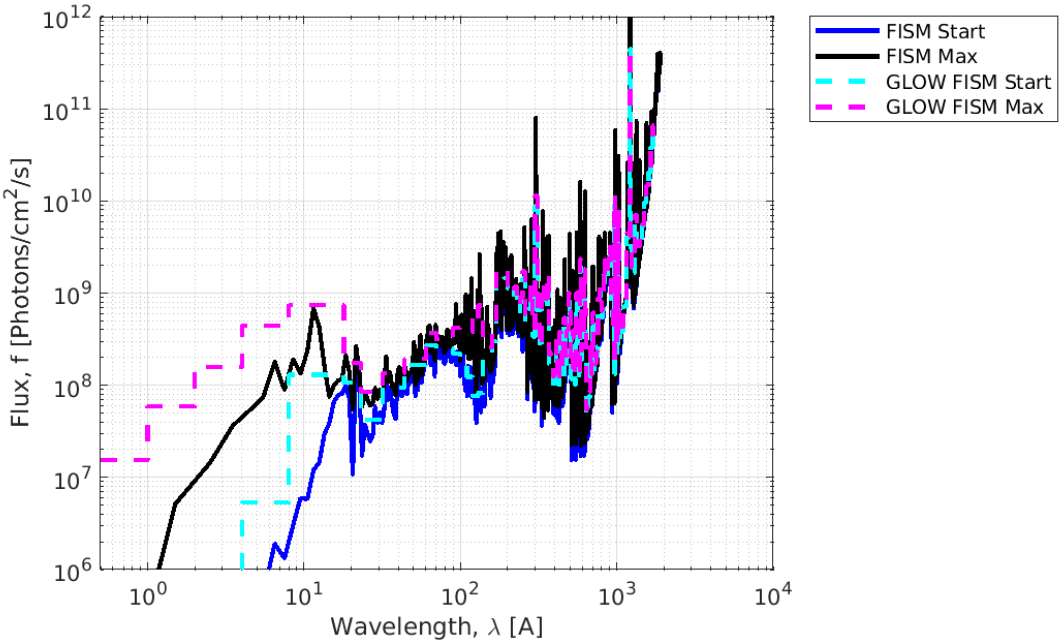

Figure 14. FISM solar spectrum at start and peak of flare for an example X-class flare with a peak at 1606 UTC on 11 July 2004.

Next, the FISM spectra and ionospheric parameters were fed into GLOW to create the electron frequency profiles. Again, an example is shown in Figure 15 and 16 for the same date and times for the start and peak of the M- and X-class flares, and includes the ionogram profile. The solid lines are at the peak times, while the dashed are at the start. The X-class again shows greater variation between the start and peak flare times except for the ionogram comparison, but also an elevated hmE.

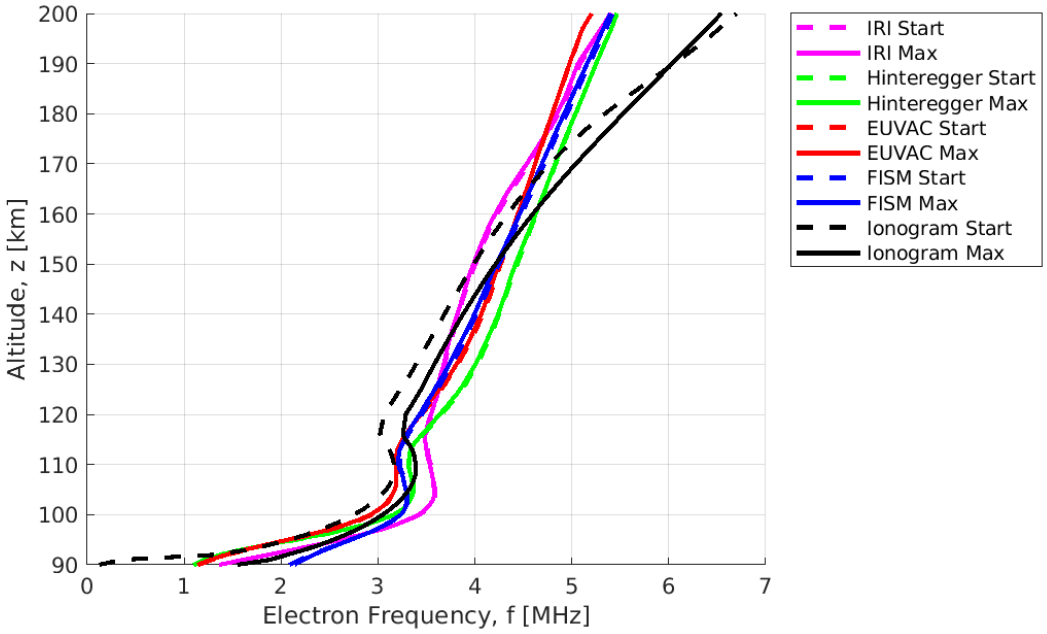

Figure 15. Electron frequency profiles at start and peak of flare for an example M-class flare with a peak at 1524 UTC on 13 February 2016.

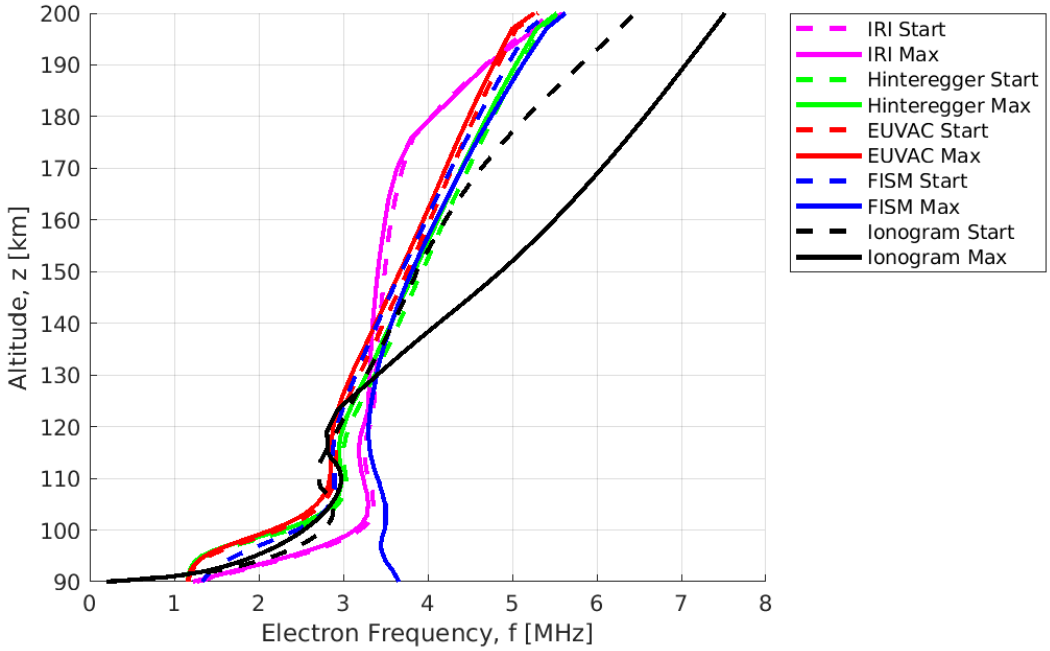

Figure 16. Electron frequency profiles at start and peak of flare for an example X-class flare with a peak at 1606 UTC on 11 July 2004.

3.2.2 hmE and foE Variations

M-class flares do not exhibit the extreme variations in electron frequency observed in X-class flares, so the difference between start and peak electron densities are minute as shown in Figure 17 for the hmE and foE differences for each of the 14 M-class flares analyzed in this study. The same differences are plotted for X-class flares in Figure 18 for the 14 flares over the entire GOES data collection period. The difference between peak time and start time values was compared against the difference in integrated intensities of the flare for the same times. The integrated intensity is the Riemann sum of the FISM spectrum bins between 0.05 and 14 nm, which according to Huang et al. (2014) is the wavelength range that has the most effect on the ionosphere due to solar heating. The integrated intensity at the start of the flare was subtracted from the integrated intensity at the peak to give the differential. This was performed to

determine how well the model handles the most extreme solar intensity differences, and also allowed a check for the model performance during a less disturbed ionosphere at the start of the flare. Although some values of the differential integrated flux are negative, implying that the flux was greater at the start than at the peak, this is not true for the entire spectrum and only for this specific wavelength bin. The ionograms have the greatest foE variation for the M-class flares, with GLOW run with FISM having the highest variation in hmE. IRI has some variation in hmE in time, but GLOW run with Hinteregger or EUVAC has no noticeable variation in time. GLOW run with FISM for the X-class flares, however, has the greatest variation in both hmE and foE, though the ionograms suggest the variation is higher for hmE than foE. IRI, GLOW run with Hinteregger, and GLOW run with EUVAC all exhibit little variation for hmE and foE for the X-class flares, which is similar to the results for the M-class flares. It would not be expected for IRI or GLOW run with either the Hinteregger method or EUVAC to exhibit significant variation in time for any class of flare, as these models are reliant only on the $F_{10.7}$ index and have little temporal variation over minutes. Meanwhile, GLOW run with FISM has a 60 second cadence and is designed to model the significant change in solar spectrum due to a flare, so the drastic variations in hmE and foE are expected.

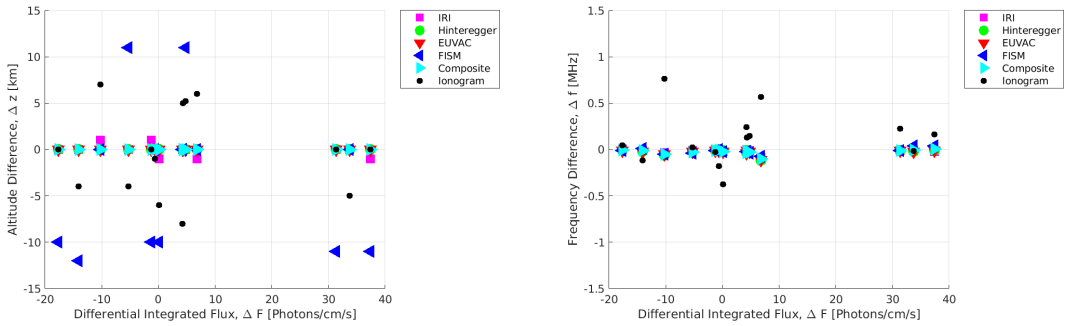

(a) hmE Difference **(b) foE Difference**

Figure 17. The hmE and foE difference between start and peak times for ionograms and all models for M-class flares compared against the difference in integrated intensity.

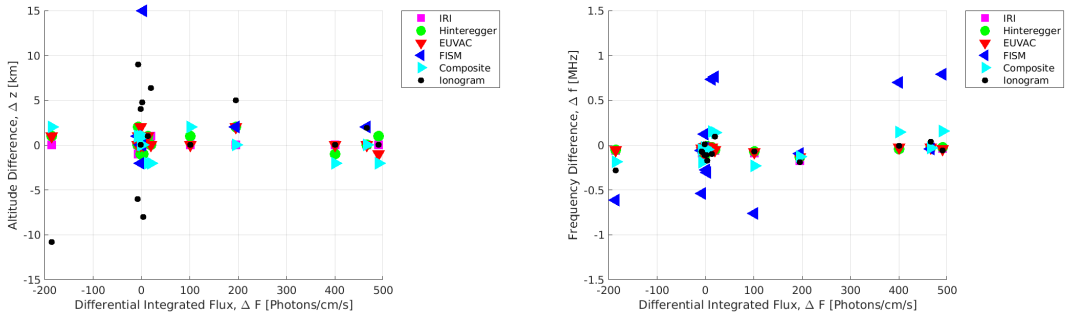

(a) hmE **(b) foE**

Figure 18. The foE difference between start and peak times for ionosonde data and all models for X-class flares compared against the difference in integrated intensity.

To check if there were any other factors that could affect the difference between start and peak times, the difference in hmE and foE were also compared to the zenith angle during the flare. If the time of day was closer to sunset and thus the zenith angle was closer to 90°, it could drastically change the resulting profiles as ionization rates would decrease. However, there was no discernible trend for the change in hmE for M-class flares in Figure 19a or the change in foE for X-class flares in Figure 20b. There is, however, somewhat of a positive relationship between solar zenith angle and

the difference in foE for the ionosonde data for M-class flares in Figure 19b and for the difference in hmE for X-class flares in Figure 20a, but not for any of the models. The lack of consistent trends between flare classes indicates that zenith angle is not responsible for the difference in hmE and foE for start and peak times. This is also somewhat expected, as the intensity as a function of altitude ($I(z)$) is derived from the optical depth τ, given in Equations 25 and 26, respectively. Thus, an examination of the change in neutral densities would also be required to determine correlation. This was not done as GLOW does not calculate the neutral densities and instead relies on the included NRLMSISE-00 model.

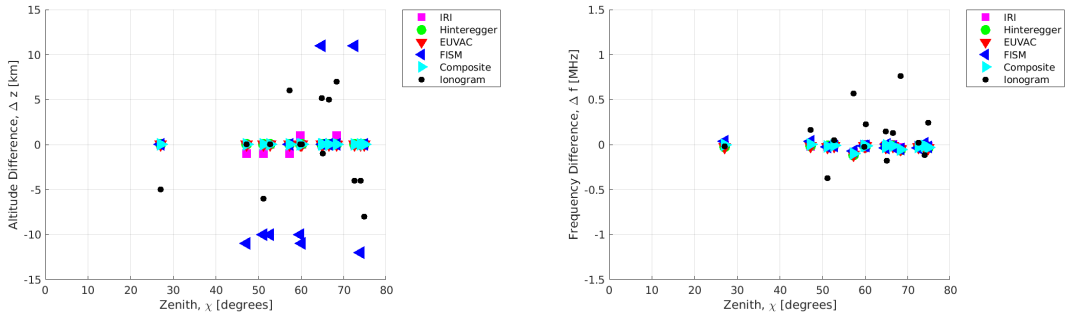

(a) hmE **(b) foE**

Figure 19. The hmE and foE differences between start and peak times for ionograms and all models for M-class flares compared against the solar zenith angle during the time of the flare.

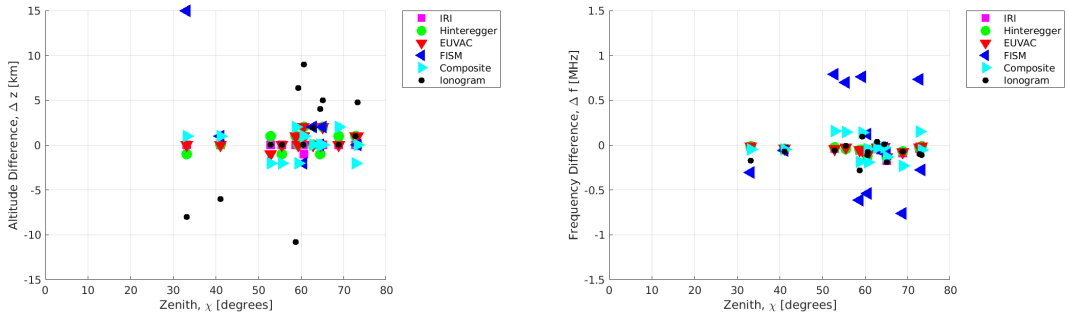

(a) hmE **(b) foE**

Figure 20. The hmE and foE differences between start and peak times for ionosonde data and all models for X-class flares compared against the solar zenith angle during the time of the flare.

To examine the accuracy of the models at predicting the data, the hmE and foE from the models at the start and peak times were compared to those from the ionosonde data. First, the difference in hmE and foE between peak and start times for the models was shown against the difference for the ionograms in Figures 21 and 22 for M- and X-class flares respectively. The ionograms for the majority of flares for both classes vary in hmE and foE between start and peak times but with no clear trend if the variation is positive or negative. Meanwhile, IRI and GLOW run with FISM vary in hmE, while GLOW run with the Hinteregger method and EUVAC do

not exhibit any change in hmE. All models have some variation in foE, but none follow the expected linear trend that would result if the models predicted the ionosonde data accurately for either class of flare.

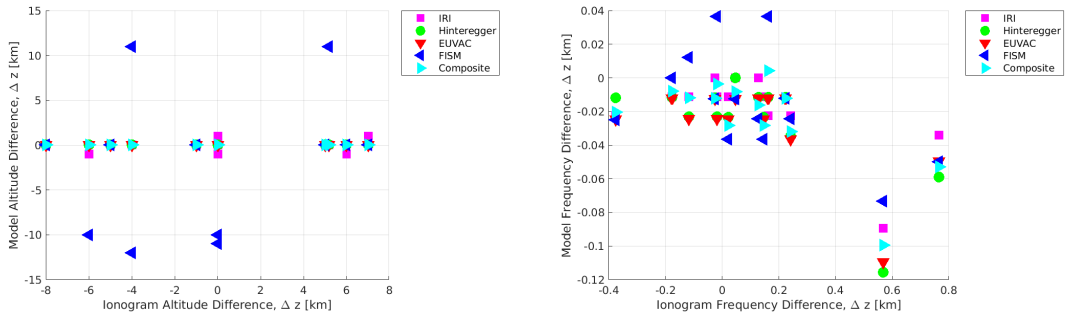

(a) hmE **(b) foE**

Figure 21. The hmE and foE differences between start and peak times for ionosonde data compared to those for all models for the M-class flares.

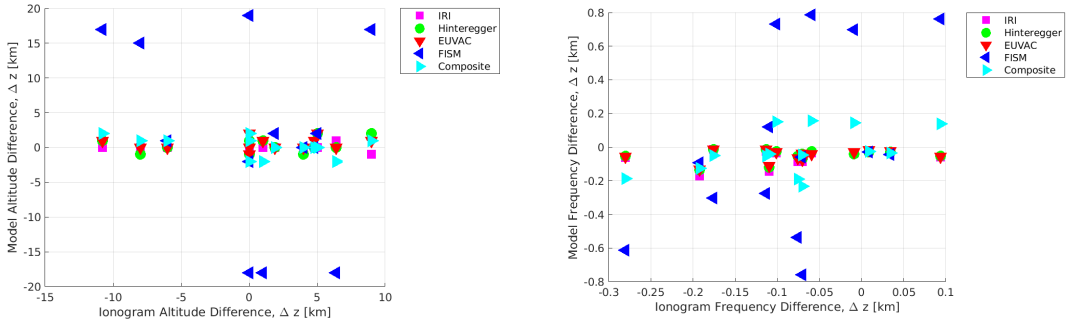

(a) hmE **(b) foE**

Figure 22. The hmE and foE differences between start and peak times for ionosonde data compared to those for all models for the X-class flares.

The difference between the observed ionogram data and the model predictions was calculated for both start and peak times, where the model hmE and foE at the start and peak times were subtracted from the ionogram hmE and foE at the start and peak times, respectively. The difference in hmE in Figure 23 revealed that IRI, the model GLOW starts with and builds calculations upon, consistently underestimated the hmE for the flares. GLOW using FISM, however, varied significantly for all flares.

GLOW using both Hinteregger and EUVAC overestimated the hmE in the flares. The composite output of GLOW followed the same trends as the Hinteregger method and EUVAC with slightly more even distribution around zero. There were not significant deviations of the differences between start and maximum times for any of the models. Overall, however, the models had no significant trend for hmE prediction.

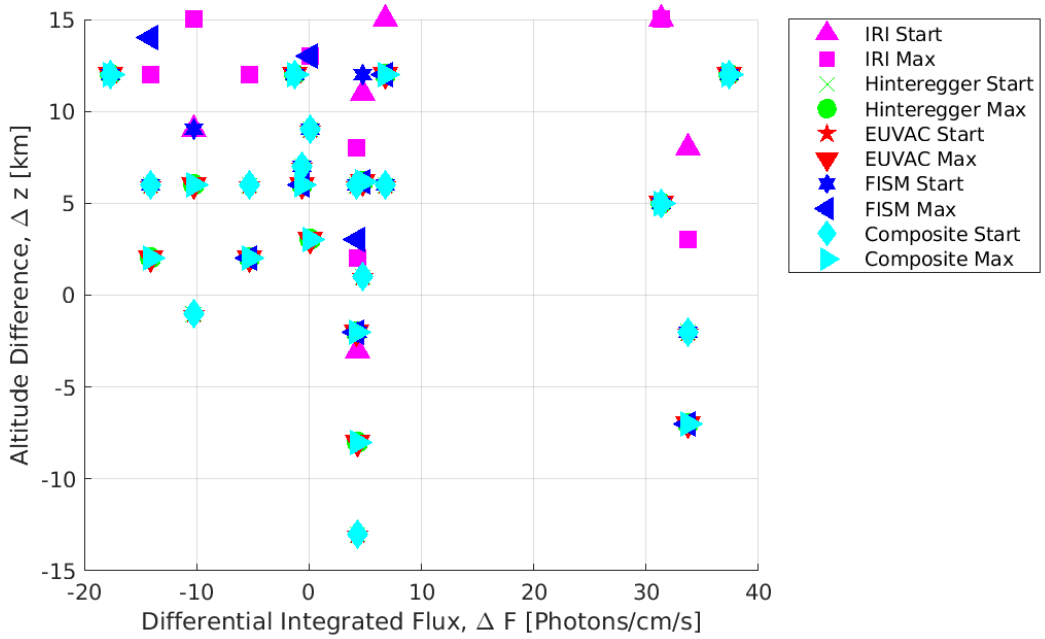

Figure 23. The hmE difference for all M-class flares between model and ionosonde data.

The difference in foE between ionosonde data and GLOW outputs in Figure 24, however, were more tightly clustered around zero than the difference in predictions for the hmE. IRI here tended to overestimate the frequency. Again, there was no significant deviation according to time or intensity.

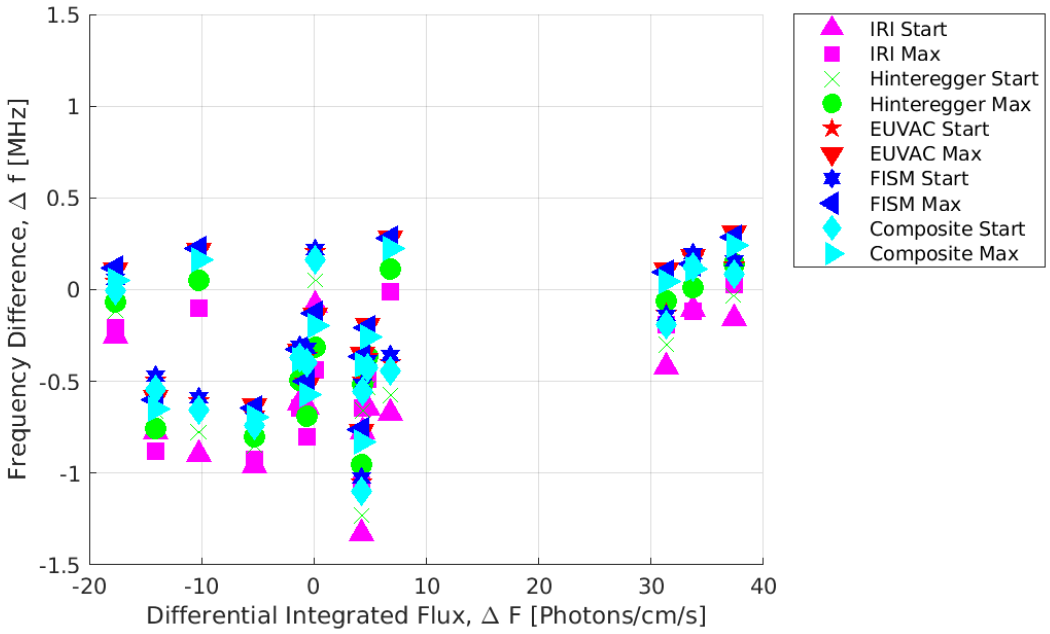

Figure 24. The foE difference for all M-class flares between model and ionosonde data.

3.2.3 Statistics for M-Class Flares

The ionosonde data for each flare was scaled by hand in the SAO Explorer and the electron frequency profiles were recalculated using the ARTIST5 software (Galkin et al., 2008) when available, which decreases uncertainty for the hmF2 and foF2 but introduces increased uncertainty into the hmE and foE measurements due to human estimation. Further, strong flares can interfere with the ionosonde and cause a blackout during the peak as found in 5 (21%) M-class flares. Ionosonde data is also only taken every 5 minutes at the highest cadence, so all flares were subject to cubic spline interpolation in time. Therefore, when considering skill scores, the uncertainty in the observational data should be taken into consideration. Statistics are only considered for M-class flares as no X-class flares will be used in Chapter IV for the ray tracing algorithm.

The total skill scores for each flare, comparing each model to the ionsonde data

for the entire electron frequency profile from 90 km to 300 km, are shown in Figures 25 and 26 and provided in Table 4 and 5. Overall, the PE for the models performed exceptionally well for the profiles, with no flares having a PE less than zero. As the PE is a comparison of the model error with respect to the observational deviations from the mean, and the electron frequency profiles contain large variations over altitude, these results are not surprising.

Table 4. The table of all the RMS scores for each model for each M-class flare, given in [MHz]. The start time is abbreviated as S., the peak time as P.; the Hinteregger method, EUVAC, and composite are also abbreviated. The best performing model for each flare has scores made bold in red.

Date	IRI S	IRI P	Hint. S	Hint. P	EU. S	EU. P	FISM S	FISM P	Comp. S	Comp. P
21-6-2015	0.30	0.46	**0.21**	0.37	0.22	0.40	0.31	0.51	**0.21**	0.39
3-7-2015	**0.62**	0.68	0.73	0.77	0.80	0.85	0.70	0.74	0.74	0.76
6-7-2015	0.53	0.53	0.58	**0.47**	0.65	0.51	0.57	0.55	0.59	0.48
21-8-2015	0.43	0.82	0.31	0.92	0.28	1.00	0.28	0.80	**0.27**	0.89
22-8-2015	**0.36**	0.52	0.51	0.58	0.55	0.65	0.47	0.57	0.50	0.55
1-10-2015	**0.38**	**0.38**	0.61	0.52	0.70	0.60	0.60	0.55	0.64	0.49
2-10-2015	**0.35**	0.38	0.47	0.52	0.52	0.57	0.45	0.43	0.48	0.49
2-10-2015	**0.81**	0.82	0.91	0.96	0.96	1.03	0.89	0.91	0.92	0.95
17-10-2015	**0.56**	0.62	0.80	0.84	0.87	0.90	0.76	0.77	0.81	0.83
31-10-2015	0.63	**0.62**	0.75	0.71	0.82	0.79	0.72	0.63	0.76	0.70
4-11-2015	0.70	0.86	**0.62**	1.52	0.67	1.61	0.61	1.56	0.63	1.55
9-11-2015	**0.40**	0.57	0.45	0.74	0.51	0.80	0.44	0.59	0.47	0.69
13-2-2016	**0.33**	0.49	0.64	0.82	0.75	0.92	0.62	0.61	0.67	0.77
14-2-2016	0.62	**0.58**	0.73	0.66	0.81	0.74	0.70	0.61	0.74	0.66

Table 5. The table of all the PE scores for each model for each M-class flare. The start time is abbreviated as S., the peak time as P.; the Hinteregger method, EUVAC, and composite are also abbreviated. The best performing model for each flare has scores made bold in red.

Date	IRI S	IRI P	Hint. S	Hint. P	EU. S	EU. P	FISM S	FISM P	Comp. S	Comp. P
21-6-2015	0.99	0.99	0.99	0.99	0.99	0.99	0.99	0.99	0.99	0.99
3-7-2015	**0.72**	0.69	0.67	0.65	0.64	0.62	0.68	0.66	0.67	0.66
6-7-2015	0.76	0.78	0.74	**0.80**	0.71	0.78	0.74	0.77	0.74	**0.80**
21-8-2015	0.79	0.58	0.85	0.53	0.86	0.49	**0.87**	0.60	**0.87**	0.54
22-8-2015	0.99	0.99	0.99	0.99	0.99	0.99	0.99	0.99	0.99	0.99
1-10-2015	**0.85**	0.84	0.75	0.77	0.71	0.74	0.75	0.76	0.74	0.79
2-10-2015	0.99	0.99	0.99	0.99	0.99	0.99	0.99	0.99	0.99	0.99
2-10-2015	0.60	**0.74**	0.55	0.70	0.52	0.68	0.56	0.71	0.54	0.70
17-10-2015	**0.87**	0.86	0.81	0.81	0.79	0.80	0.82	0.82	0.81	0.81
31-10-2015	0.99	0.99	0.99	0.99	0.99	0.99	0.99	0.99	0.99	0.99
4-11-2015	0.68	**1.00**	0.72	0.99	0.69	**1.00**	0.72	**1.00**	0.71	**1.00**
9-11-2015	**0.86**	0.77	0.84	0.70	0.82	0.68	0.85	0.76	0.84	0.73
13-2-2016	**0.99**	0.96	0.98	0.93	0.98	0.93	0.99	0.95	0.98	0.94
14-2-2016	0.78	**0.79**	0.74	0.77	0.72	0.74	0.75	0.78	0.74	0.77

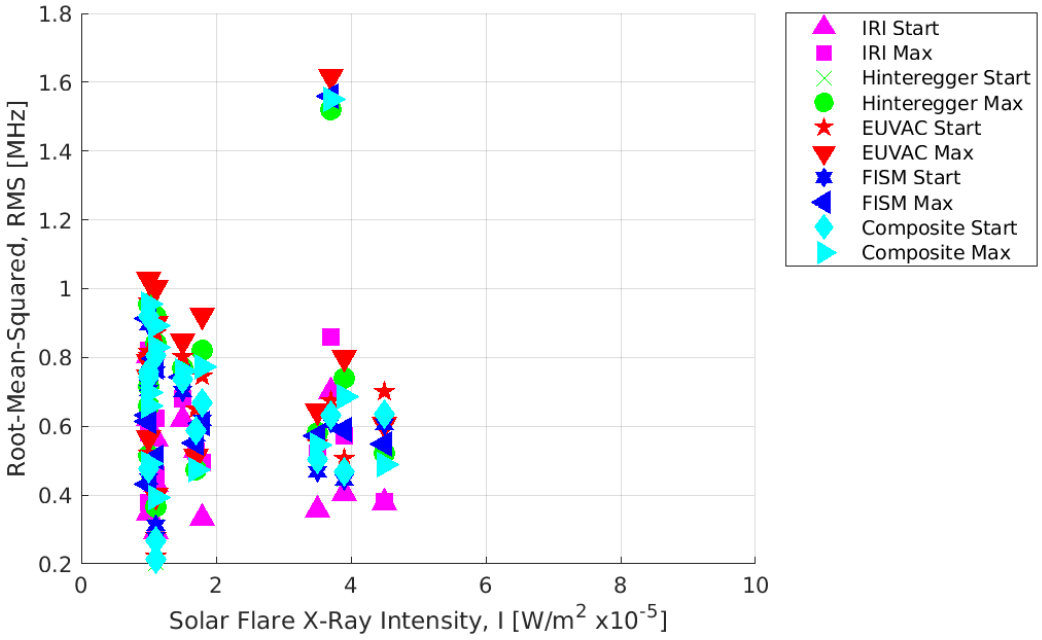

Figure 25. The RMS calculations of each M-class flare for the full profile, given for each model. The scores are compared to the solar intensity of the flare. The lower the RMS value, the better the model did at representing the real data.

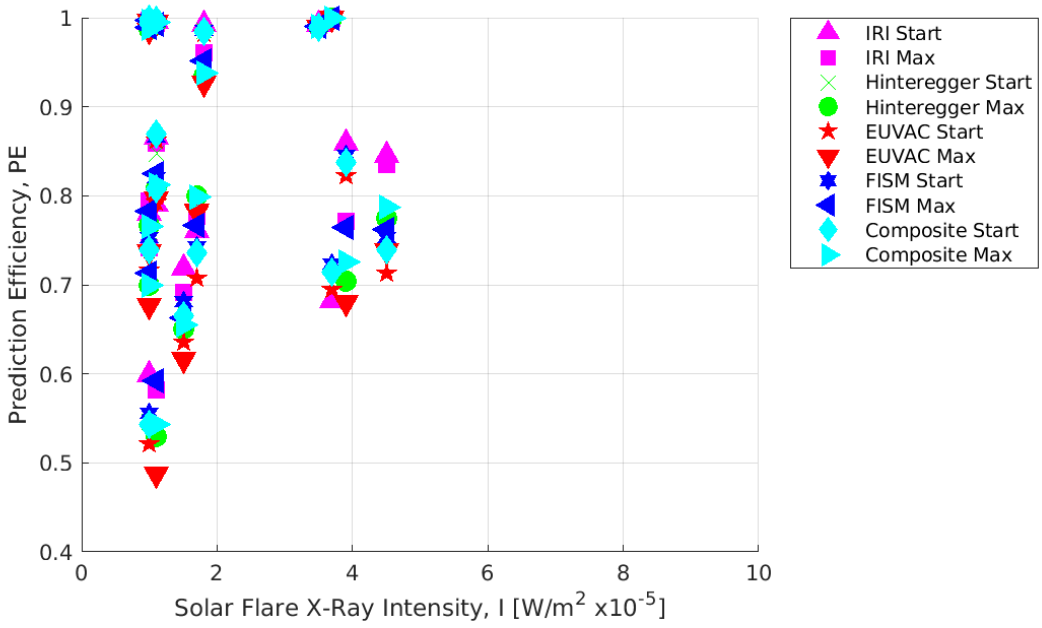

Figure 26. The PE calculations of each M-class flare for the full profile, given for each model. The scores are compared to the solar intensity of the flare. The closer to 1, the better the fit.

The RMS for all flares in the letter category was determined for both hmE and foE in Figure 27, with the total scores found in Table 6. The RMS for the peak times was consistently and considerably lower than at the start time for the hmE and foE except for the hmE when GLOW was run with FISM. As was evident in the difference plots as well, IRI performed the worst for hmE and foE, while GLOW with Hinteregger and EUVAC performed well for both. GLOW run with FISM did the best for the foE. The composite's scores, however, were low for both hmE and foE.

Table 6. The table of RMS values for each model for each parameter, in [km] for hmE and [MHz] for foE. The best performing model has scores made bold in red.

Parameter	IRI	Hinteregger	EUVAC	FISM	Composite
hmE Start	15.85	**8.04**	**8.04**	9.32	**8.04**
hmE Max	15.57	**7.77**	**7.77**	13.78	**7.77**
foE Start	0.69	0.59	0.47	**0.46**	0.50
foE Max	0.58	0.49	0.40	**0.39**	0.42

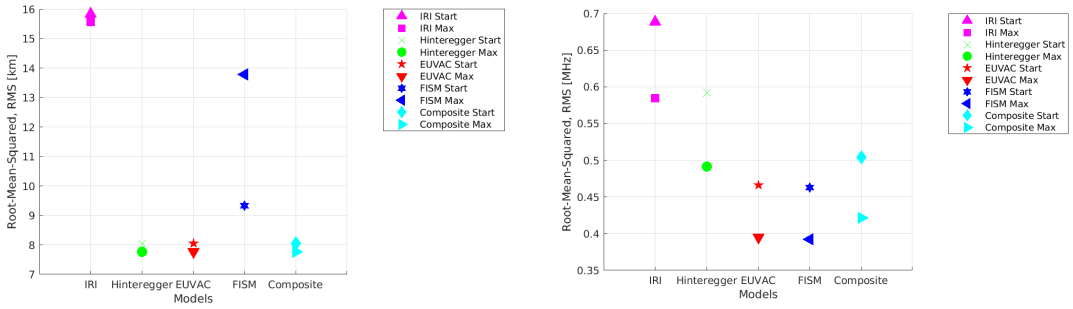

(a) hmE **(b) foE**

Figure 27. The RMS calculations of the M-class flares for the hmE and foE at the start and peak flare times.

The PE skill scores in Table 7 were also used to determine model efficiency, displayed in Figure 28, with similar results to the RMS scores. None of the PE scores

rose above zero, but all the models at the peak time were greater than -1 for both hmE and foE, with all variations of GLOW having greater than -0.5 at the peak time, indicating that GLOW is more reliable for flares to capture both hmE and foE. The PE scores for the hmE at the start time are particularly low, possibly due to the models trying to match to the overall profile rather than to the peak of the E-layer.

Table 7. The table of PE values for each model for each parameter. The best performing model has scores made bold in red.

Parameter	IRI	Hinteregger	EUVAC	FISM	Composite
hmE Start	-45.63	**-22.67**	**-22.67**	-26.44	**-22.67**
hmE Max	-1.41	**-0.16**	**-0.16**	-1.10	**-0.16**
foE Start	**-0.01**	**-0.01**	-0.02	-0.02	**-0.01**
foE Max	**-0.02**	**-0.02**	-0.03	-0.03	-0.03

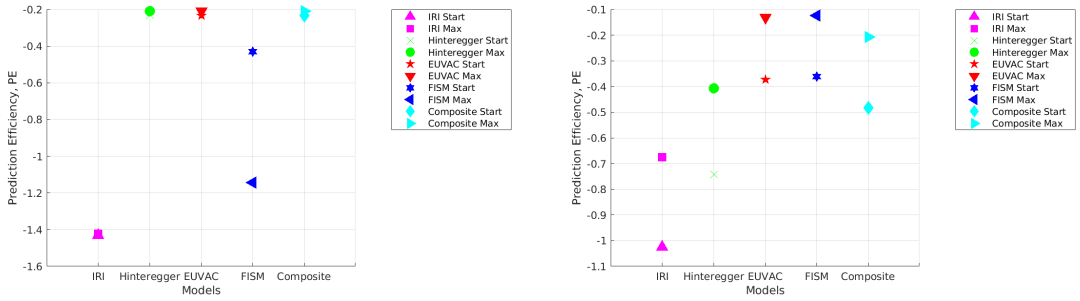

(a) hmE **(b) foE**

Figure 28. The PE calculations of M-class flares for the hmE and foE. A PE of 1 indicates a perfect model, while a score of 0 means the model performs as well as the variability around the mean and a negative score indicates the mean is a better fit than the model.

3.3 Discussion

This portion of the research showed that M-class flares can circumvent the blackout problem in ionosonde data for X-class flares, and M-class flares provided sufficient difference between flare start and peak values to provide useful analysis for models. X-class flares tended to degrade or under-saturate most HF measurement devices during the peak, resulting in empty ionograms. This was found when analyzing the 34 flares between 1 January 2003 and 31 December 2016 and finding that 59% of the X-class flares had empty ionograms. Conversely, of the 19 M-class flares between 1 June 2015 and 27 September 2016, only 26% were empty. This further supports the point that there are significantly more M-class flares that can be analyzed over X-class flares. Between 1 June 2015 and 27 September 2016, the time period corresponding to the HF data, there were no X-class flares. However between 1 January 2003 and 31 December 2016, there were a total of 1,084 M-class flares and 357 M-class flares that met the zenith angle requirements. Consequently, further research on solar flares can be aided by ensemble studies using M-class flares that demonstrate enhancement in electron content, but circumvent under-saturation.

Surprisingly, using FISM as a supplied solar spectrum did not improve the performance of GLOW in comparison with its own built-in solar spectrum schemes. According to FISM's literature, it was designed to be used for the smaller time-scales of flares and has been verified in other studies, so it was expected that FISM would perform the best in all statistics, but especially for foE. This is potentially caused by GLOW's coarse binning scheme that uses 123 bins but does not consider smaller bins around absorption lines, or GLOW's lack of energy codes as there is some evidence of ionospheric heating due to solar flares (Huang et al., 2014). Instead, the Hinteregger and EUVAC spectra are better fits for M-class flares for both the hmE and foE. However, GLOW run with any solar spectrum performs better than IRI at predicting

the foE, which is important for the application to HF skywave circuits.

A composite of all three methods will also be used for the ray tracing algorithm and is suggested for use in future applications. A larger sample of M-class flares is recommended for an ensemble study using an array of models, including IRI, NeQuick, and full-physics models like TIE-GCM and GITM. NeQuick can provide a comparison on how the sunspot number performs as a proxy for solar activity versus the $F_{10.7}$ proxy, while the full-physics models can provide a different comparison for full solar spectra. While these full-physics models are more computationally expensive, it is expected that these models will have more flexible electron frequency profiles and more accurate predictions for hmE and foE. The electron frequency profiles generated are used in a ray tracing algorithm between Millstone Hill and a CODAR site to predict changes in HF circuits and are shown in Chapter IV, as accurate electron frequency profiles are key to predicting ray paths.

IV. HF Skywave Circuit Response Modeling

In this chapter, the electron frequency profiles were input to a ray tracing algorithm in an effort to model HF skywave circuit data during the flares. This mirrors a similar study completed by Burg (2020).

4.1 Methodology

4.1.1 Data Selection

As mentioned in Chapter III, the HF circuit data to be used to compare the model results to comes from the HF collection described by Ginet et al. (2018). The experiment had multiple transmitters shown in Figure 29, but for this component the data products required were the measured group delay (τ_g), azimuth angle (α), and elevation angle (ϵ), where the azimuth and elevation angles compose the angle of arrival (AoA). The azimuth characterizes the direction of the incoming signal, with 0° representing north; the elevation characterizes the steepness of the incoming signal in regards to the z-axis and measured from the ground, so an elevation of 90° corresponds to a zenith angle of 0°. Meanwhile, the group delay represents the transit time between transmission and reception, derived from the integrated group path.

Ultimately, only two transmitter sites had data products (CSTM and NANT) both of which are Coastal Ocean Dynamics Applications Radar (CODAR) transmitters. The CSTM transmitter operated at the frequency of 4.82 MHz between 1 June 2015 and 27 September 2016 and contains 449 days of data, and the NANT transmitter operated at 4.8995 MHz from 15 July 2015 to 30 April 2016 for 251 days. The NANT CODAR transmitter site was located at 41.249° latitude and 290.026° longitude, and the CSTM CODAR transmitter site was located at 44.086° latitude and 293.789° longitude. Both have a maximum resolution of five seconds. The receiver site was at

Millstone Hill, located at 42.503° latitude and 288.765° longitude. Given the duration of and consistency data collection, the CSTM site as the transmitter was chosen as the data for comparison.

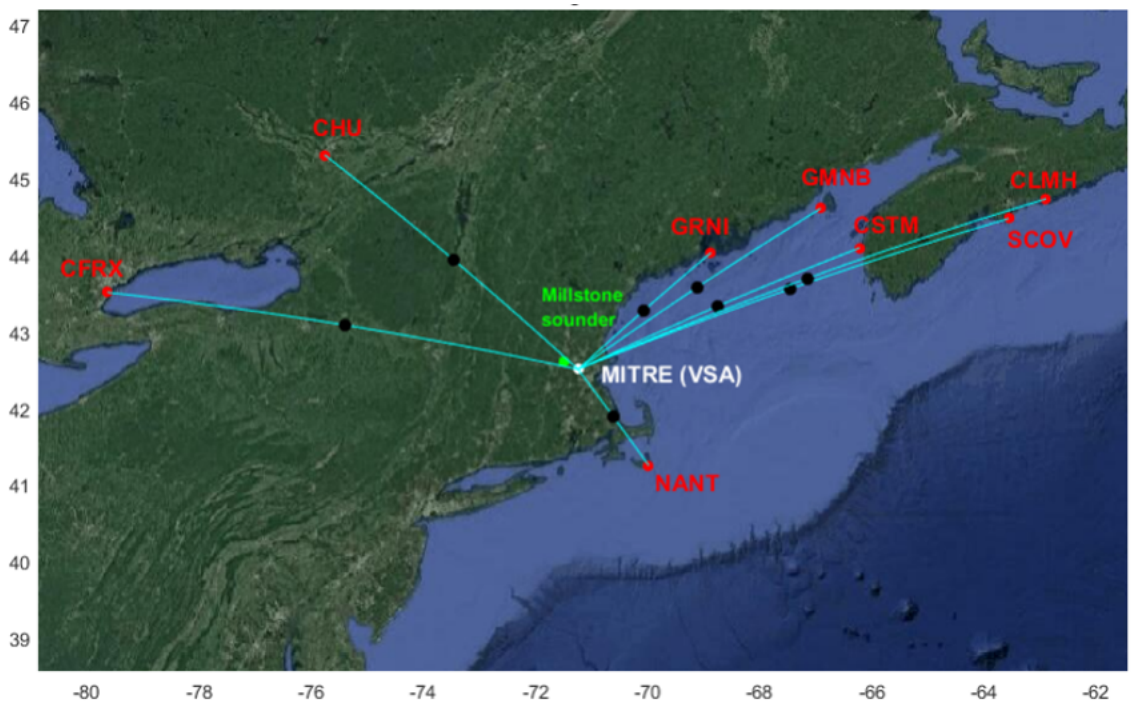

Figure 29. The map of the various transmitter sites in relation to the receiver at Millstone Hill (Ginet et al., 2018).

The HF AoA and group delay data for each of the flare dates was examined to determine the impacts of M-class flares. Each flare had data for the ordinary (O) and extraordinary (X) modes for the F-layer and X-mode for the E-layer. Here, only the O-mode is considered and therefore only the F-layer is used. There are gaps in the data collection for each day due to either ionospheric absorption or the reduction in ionosphere plasma densities particularly in the E-layer and F_1-layer after sunset and before sunrise. If such a data gap existed during the two hours surrounding a flare that was used in the previous section, the flare was removed from the data set. An example is given in Figure 30 for the flare on 21 June 2015. There is no data for the F-layer during the flare, so this flare was removed when analyzing the whole set.

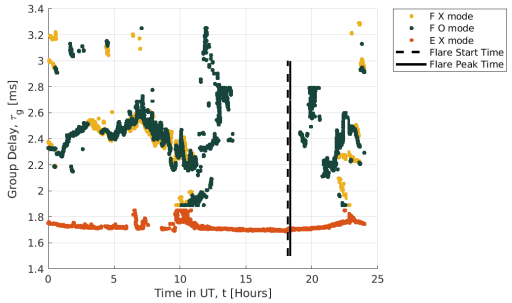

(a) Group Delay

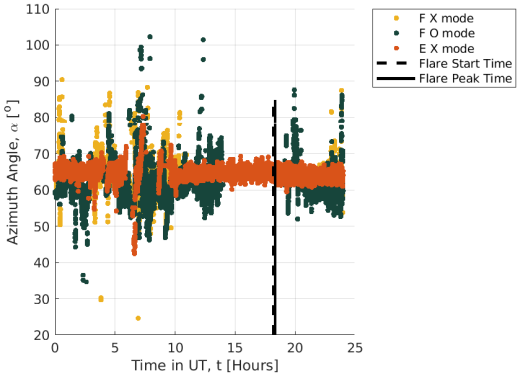

(b) Azimuth

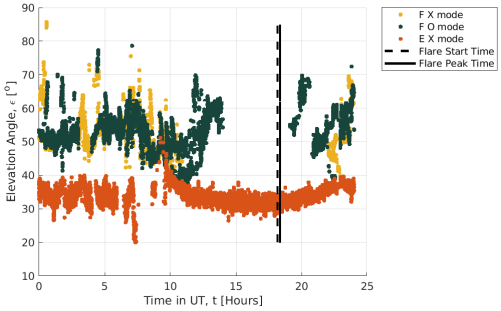

(c) Elevation

Figure 30. The group delay, azimuth angle, and elevation angle for 21 June 2015 for the O- and X-modes for the *F*-layer in green and yellow, respectively, and the X-mode for the *E*-layer. Obviously, there is no data for the *F*-layer during the flare.

In addition, since the resolution was so small for the data collection, the data was averaged over segments to produce a smoothed running average, which was then interpolated to match the one minute time intervals from the models. Since each flare had different sized time arrays, only a consistent sized segment of 24 data points were used in each forward running average section, given by the formula

$$x_{ave_j} = \frac{1}{24} \sum_{i=j}^{j+24} x_i. \tag{45}$$

The resulting smoothed running average was interpolated to the model times using MATLAB's built-in `spline` function, which computes a cubic spline that fits the given data.

4.1.2 Ray Tracing Algorithm

The selected ray tracing algorithm (Dao et al., 2016) was developed by AFRL and is an updated version of the algorithm developed by Jones and Stephenson (1975). Instead of FORTRAN, the algorithm is written in the coding language Julia. It plots the electron frequency profiles used for the input, produces the ray of the signal through an iterative process, and outputs the signal path, group path, group delay, azimuth angle, and elevation angle.

The ray tracing algorithm operates by importing a file detailing the electron frequency profiles over the area of interest. The electron frequency profiles used consist of 20 latitude values, 20 longitude values, and 102 altitude values; the latitude values span between 42° and 45°, the longitude values span from -72° to -66°, and the altitude ranges from 80 km to 640 km. A file for the three-dimensional grid of electron frequencies was generated for each minute of the two-hour span surrounding the flare for each flare. The electron frequencies are interpolated and then used to inform the calculations for the index of refraction used in the integration of the Hamiltonian equations. The algorithm can further be tuned for specific scenarios by adjusting the virtual height and desired wave mode. Here, the chosen virtual height was 500 km and only the O-mode was utilized. Finally, if a solution cannot be obtained, all results for that file are omitted from the analysis.

4.1.3 Comparisons and Statistics

Once the results from the ray tracing algorithm were obtained, each variable was compared with the CODAR data. However, a strange phenomena was noticed immediately: some of the results from the ray tracing algorithm set to find an O-mode solution for the HF circuit matched best with the *E*-layer X-mode rather than the *F*-layer O-mode, as given by the example in Figure 31 of the flare on 21 August 2015.

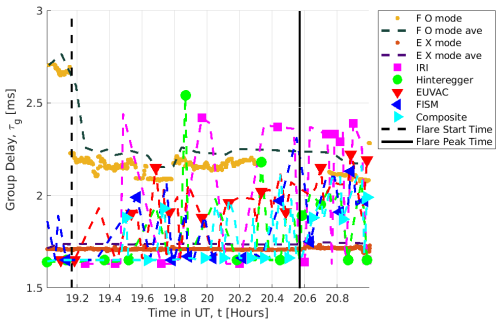

(a) Group Delay

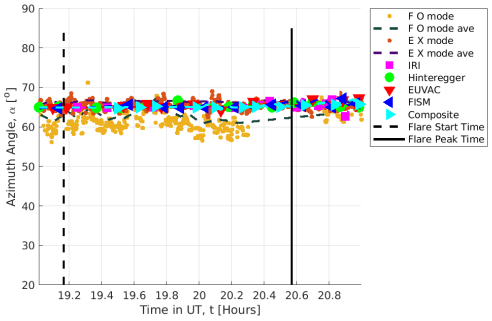

(b) Azimuth

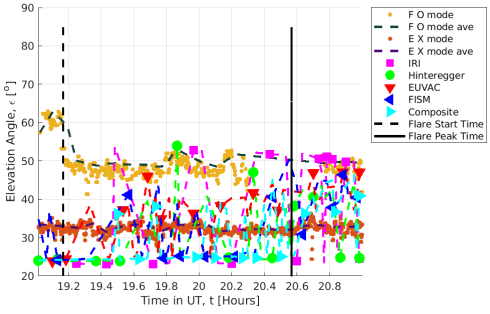

(c) Elevation

Figure 31. The group delay, azimuth angle, and elevation angle for 21 August 2015 for the models, the O-mode for the *F*-layer with its running average, and the X-mode for the *E*-layer and its running average. IRI and the Hinteregger method demonstrate the noticeable "split" in the data between the two modes in the group delay and elevation angle.

The data for the models was subsequently divided into two data sets to correspond to the two modes, determined by the minimum difference between the models' points and the data points of the two modes. The resulting split is demonstrated in Figure 32. The rest of the calculations and statistics were calculated based on this split for both the *F*-layer O-mode and *E*-layer X-mode.

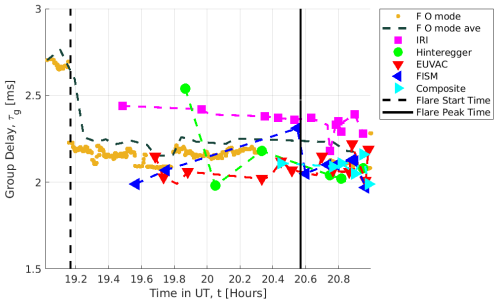

(a) Group Delay - F

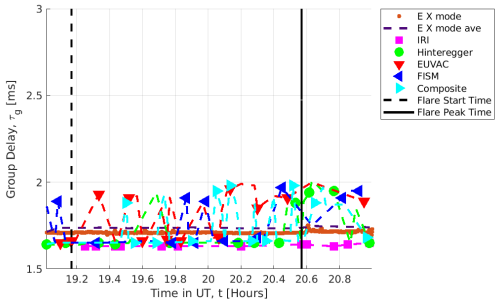

(b) Group Delay - E

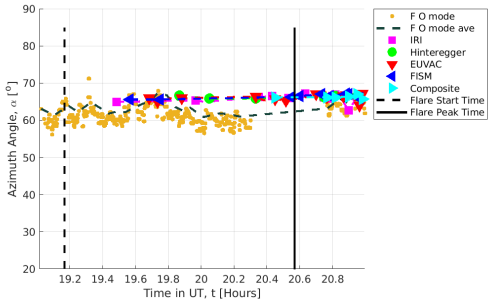

(c) Azimuth - F

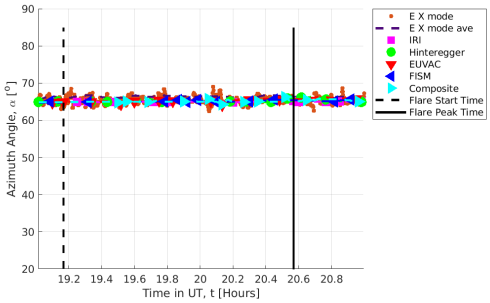

(d) Azimuth - E

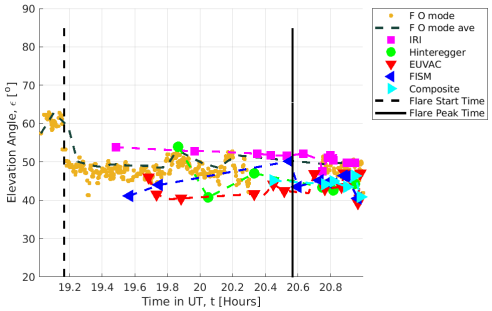

(e) Elevation - F

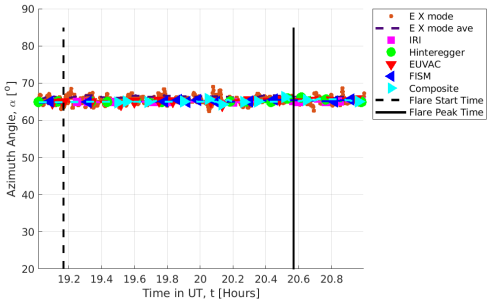

(f) Elevation - E

Figure 32. The group delay, azimuth angle, and elevation angle for 21 August 2015 for the models, with the O-mode for the *F*-layer on the left, and the X-mode for the *E*-layer split from the O-mode solutions on the right. All flares were split in this way for processing.

As each model for each flare was split differently, Table 8 shows which models had data for which layer for each flare.

Table 8. A table of which flares and models have data for each layer. This includes removing sets that do not cover the time period of interest (for example, the flare on 21 August 2015 does not have the full period for the *F*-layer). The table lists the layer with available measured and simulated data, represented by either E or F.

Date [DD-MM-YYYY]	**IRI**	**Hinteregger**	**EUVAC**	**FISM**	**Composite**
21-6-2015	E	E	E	E	E
3-7-2015	E,F	E,F	E,F	E,F	E,F
6-7-2015	E,F	E,F	E,F	E,F	E,F
21-8-2015	E	E	E	E	E
22-8-2015	F	F	F	F	F
1-10-2015	E,F	E,F	F	F	F
2-10-2015	E,F	F	F	F	F
2-10-2015	E,F	E,F	F	E,F	E,F
17-10-2015	–	–	–	–	–
31-10-2015	F	F	F	F	F
4-11-2015	E,F	F	F	F	F
9-11-2015	–	–	–	–	–
13-2-2016	F	E,F	F	F	F
14-2-2016	F	F	F	F	F

Similar to the analysis of the electron frequency profiles to the ionosonde data, the interpolated data from the CODAR HF circuits and the models were compared at the start and peak times for group delay, azimuth angle, and elevation angle using the RMS and PE scores described by Equations 43 and 44, respectively. The difference between peak and start time for each is also compared.

To examine if there is a significant change due to the flare, the change in the data and models over time was computed by taking the slope between consecutive data points, with an example shown in Figure 33. Since the greatest changes do not occur exactly at the start or peak times, the greatest change in the five minutes prior to the start of the flare and the greatest change between the start and peak times are used as the slope for the pre-flare or flaring time, respectively. The slope for the group delay, azimuth angle, and elevation angle are also compared in a similar manner using

the RMS and PE skill scores.

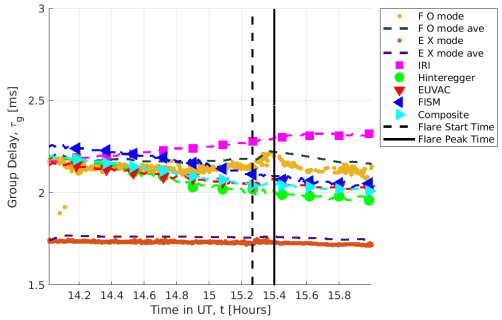

(a) Group Delay

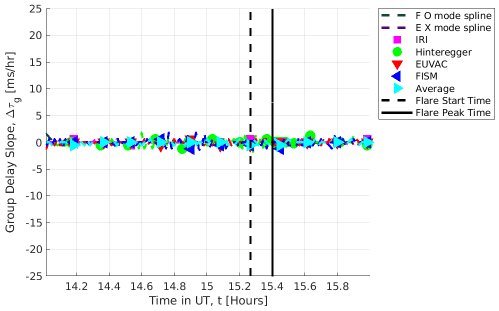

(b) Group Delay Slope

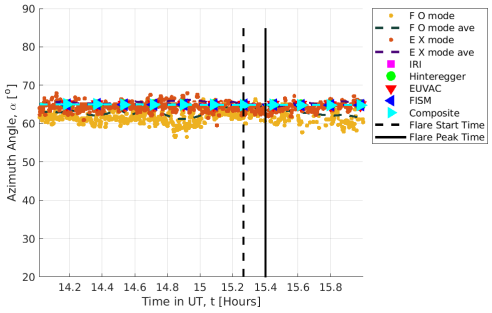

(c) Azimuth

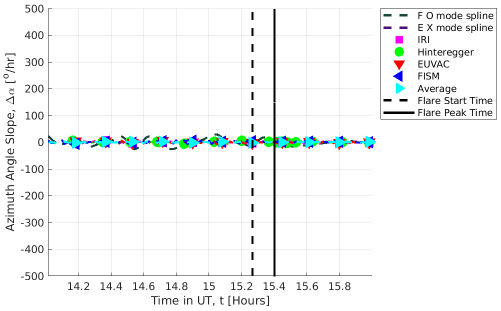

(d) Azimuth Slope

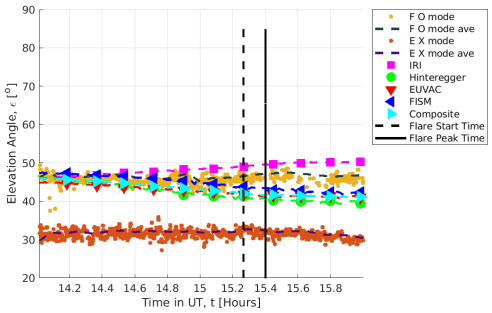

(e) Elevation

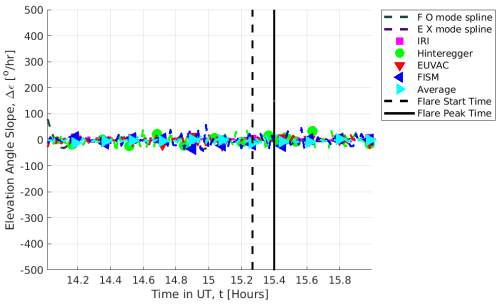

(f) Elevation Slope

Figure 33. The values and change in group delay, azimuth angle, and elevation angle for 13 February 2016 for the models, the O-mode for the *F*-layer with its running average, and the X-mode for the *E*-layer and its running average.

4.2 AoA Parameter Analysis

Once the modeled data was processed, the AoA parameters and the slopes were compared with the measured data. These two sets will be presented separately, beginning with the HF circuit parameters of group delay, azimuth angle, and elevation angle.

4.2.1 HF Circuit Parameter Time Variation

First, to determine how the AoA parameters are expected to behave during an ionospheric enhancement, a test case was created using GLOW run with EUVAC where the $F_{10.7}$ index was increased by 0.5 sfu every minute over two hours during an arbitrary date and time, with every other parameter held constant. Specifically, the date is 1 January 2000 starting at 1500 UTC, the previous day and 81-day average $F_{10.7}$ are 120 sfu, the Ap index is 4, and the $F_{10.7}$ begins at 120 sfu and ends at 180 sfu. These electron frequency profiles were used in the ray tracer and the results are presented in Figure 34. The predominant trends occur in the group delay and elevation angle, where both are decreasing as the solar flux increases. This matches theory, as the enhancement would decrease the altitude where the signal would reflect (see Figure 16) and therefore shorten the path. There is also a decrease in azimuth angle, but the data is highly scattered temporally.

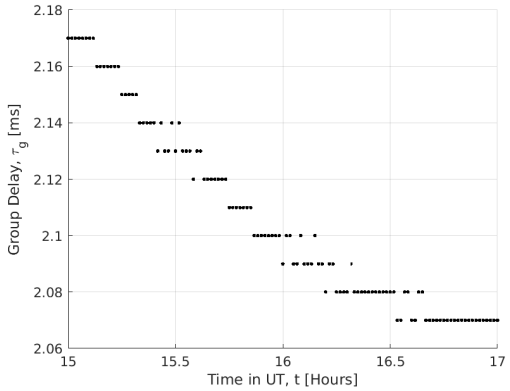

(a) Group Delay

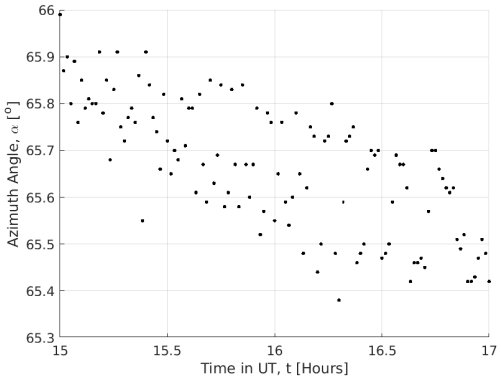

(b) Azimuth

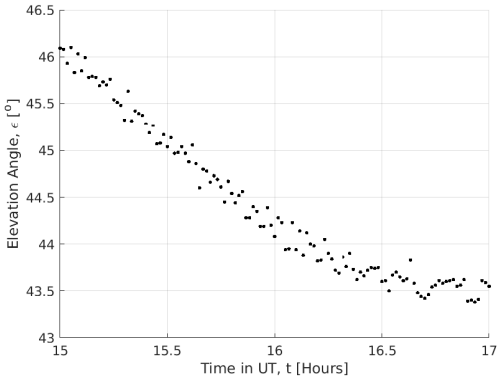

(c) Elevation

Figure 34. An example of how the AoA parameters of group delay, azimuth angle, and elevation angle respond to an enhancement of the solar flux. This uses electron frequency profiles from GLOW using EUVAC on 1 January 2000 at 1500 UTC, where the $F_{10.7}$ index increases by 0.5 sfu every minute, starting at 120 sfu.

The difference between the flare peak time and start time were first analyzed. The entire data set was considered instead of being separated to avoid having to interpolate the parameters in time. The first comparison is in regard to the differential integrated flux, which is the Riemann sum of the solar EUV flux between 0.05 and 14 nm at the start time subtracted from the Riemann sum of the flux at the peak time, shown in Figure 35. IRI was the most variable of all the models, but did not align with the AoA data. Further, there is no discernible trend between the change in solar flux and the change in any of the parameters. Some of the extreme differences, particularly for IRI, are most likely due to switch between E-layer and F-layer modes.

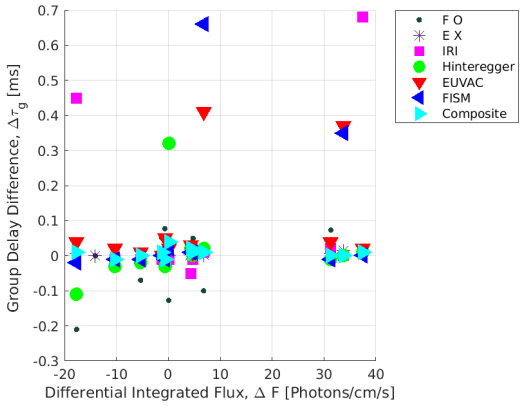

(a) Group Delay

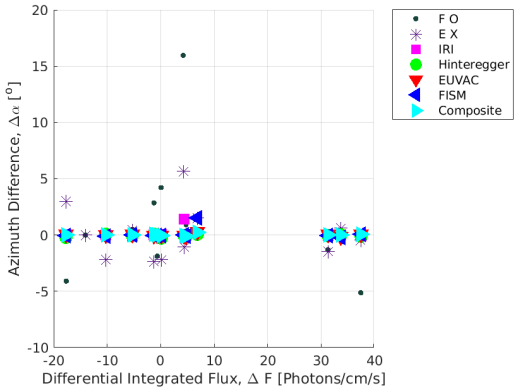

(b) Azimuth

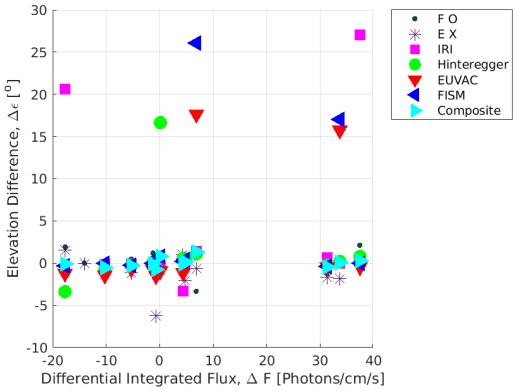

(c) Elevation

Figure 35. The comparison of the variation from the flare peak to start for group delay, azimuth angle, and elevation angle to the differential integrated flux.

The difference between peak and start time was compared again against the solar zenith angle in Figure 36; again, there was no significant trend between the change of any of the parameters and the zenith angle during the flare. This is similar to the results for GLOW. However, the time scale of the flare is small enough that there should not be a significant change based on the progression of the zenith angle; instead, the gaps in the CODAR data over 24-hours, like in Figure 30, can be partially explained by the change in zenith angle as certain modes are not supported at night. Again, however, the combination of of EUV flux, zenith angle, and neutral densities are required to properly model the changes in photoionization as the intensity is

a function of the optical depth, but the neutral densities are not calculated by the models of interest. Again, the extreme differences are potentially due to the switching between the E-layer and F-layer modes.

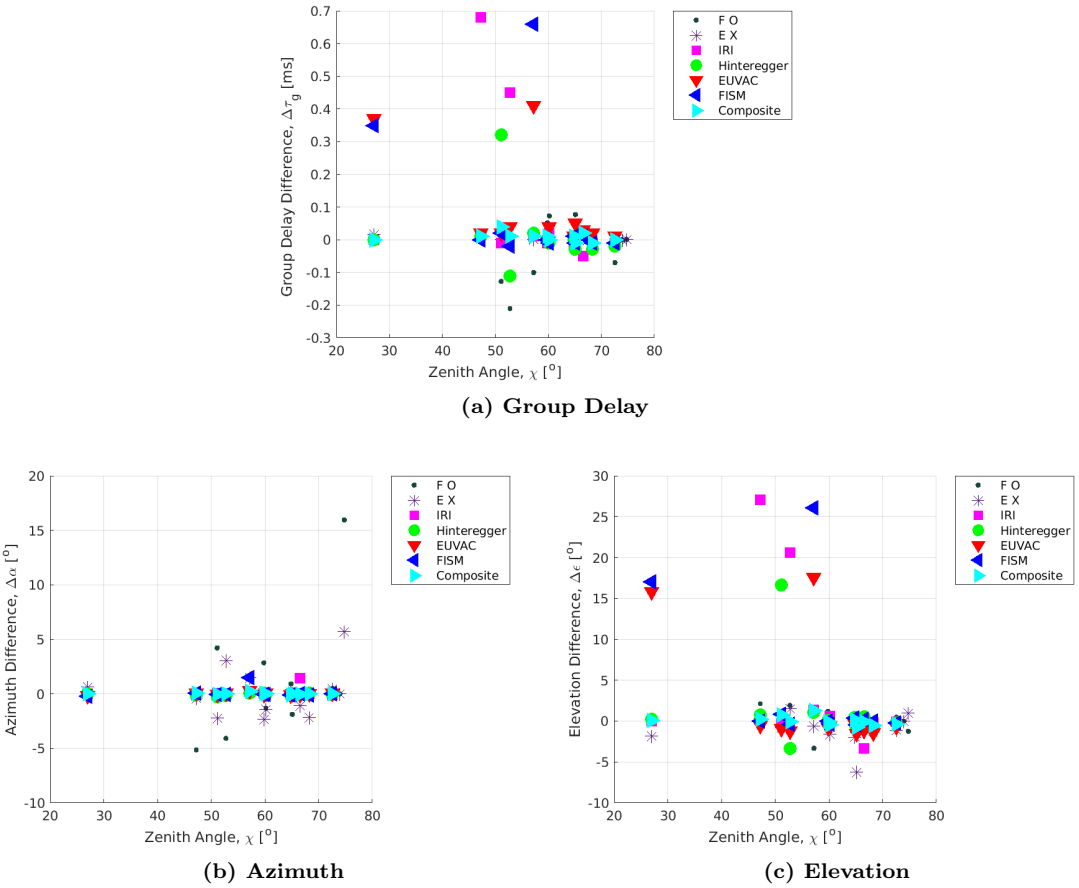

(a) Group Delay

(b) Azimuth

(c) Elevation

Figure 36. The comparison of the variation from the flare peak to start times for group delay, azimuth angle, and elevation angle to the solar zenith angle at the time of the flare.

The difference between peak to start times for each of the AoA parameters was computed and the variation in the CODAR data was directly compared to the change in model results in Figure 37. Again, this made no distinction between E- and F-layer in the models in order to avoid interpolation, though the F-layer data from the CODAR data set was used for this comparison. There is little variation in the models, and some variation can be attributed to the data being split between layers. Though

the expected and observed variation in time for the group delay should be negative as the solar intensity increases, GLOW using FISM and EUVAC had positive changes. There was also a significant number of flares that showed little change between start and peak times in the CODAR data for the azimuth and elevation angles, and the model parameters reflect this.

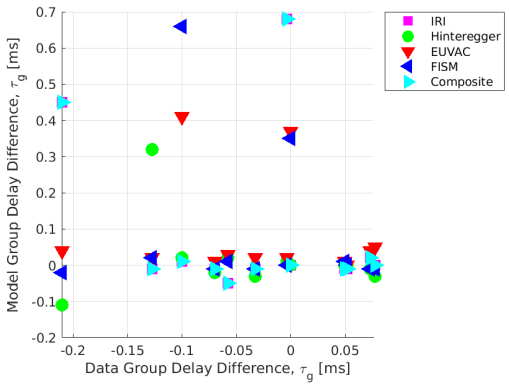

(a) Group Delay

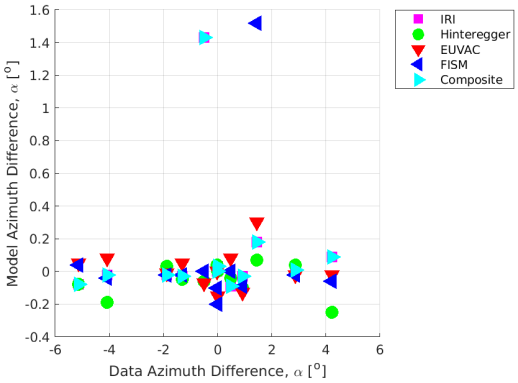

(b) Azimuth

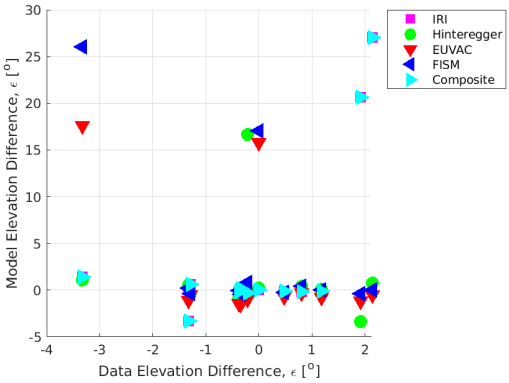

(c) Elevation

Figure 37. The comparison of the variation from the flare peak to start times for group delay, azimuth angle, and elevation angle to the the variation between peak and start times for the same parameters from the CODAR data.

The variation from the peak to start times from the electron frequency profiles was also compared to the variation in time in the ray tracing data as shown in Figure 38. The difference in hmE and foE between peak and start time for each model was directly compared to the difference in group delay, azimuth angle, and elevation angle between the same times and same model, and the difference in ionosonde data was compared to the difference in CODAR data, and revealed that there was no overall trend or correlation between the profiles and the ray tracing data. These were also not separated by layer to avoid interpolation. Interestingly, the greater the absolute change in hmE for the FISM frequency profiles, the less change there was in all AoA parameters. The inverse also seems to hold that the less change in the hmE, the greater the variation in AoA parameters over time, but no model besides FISM showed a significant variation. The data also showed more variation in hmE over the AoA parameters for the F-layer, similar to GLOW run with FISM. No such pattern was observed in the change in foE.

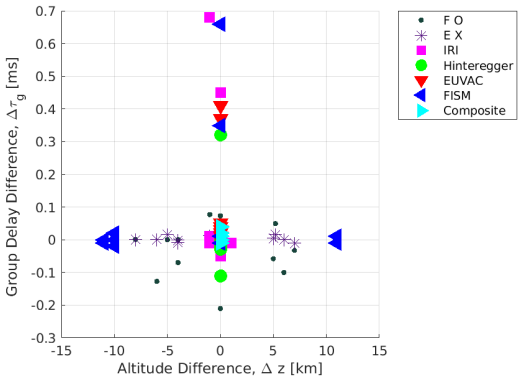

(a) Group Delay - hmE

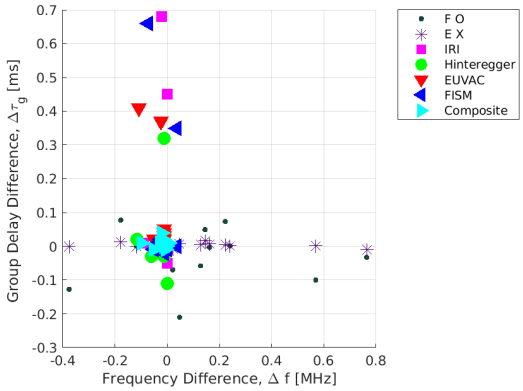

(b) Group Delay - foE

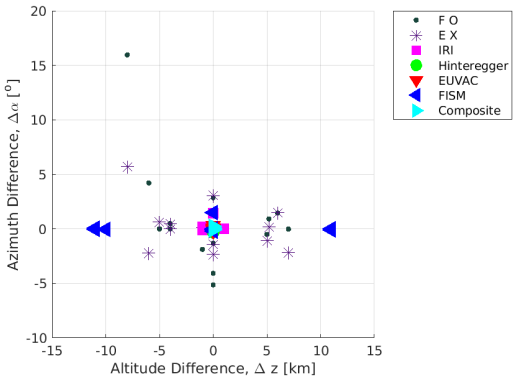

(c) Azimuth - hmE

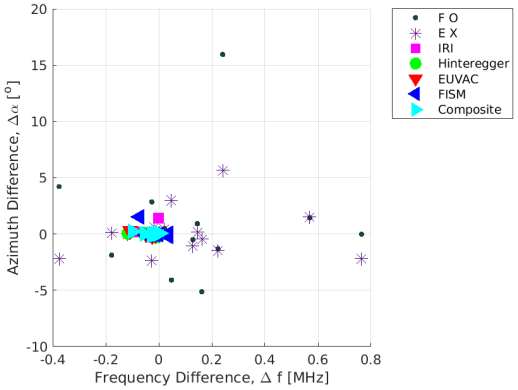

(d) Azimuth - foE

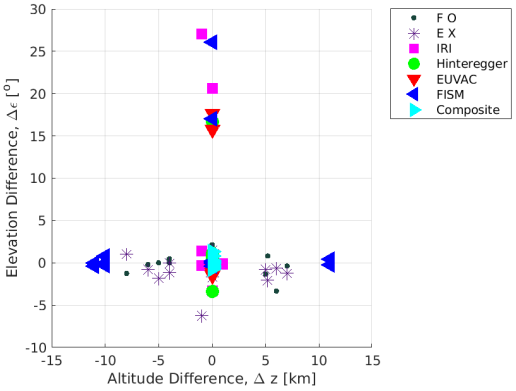

(e) Elevation - hmE

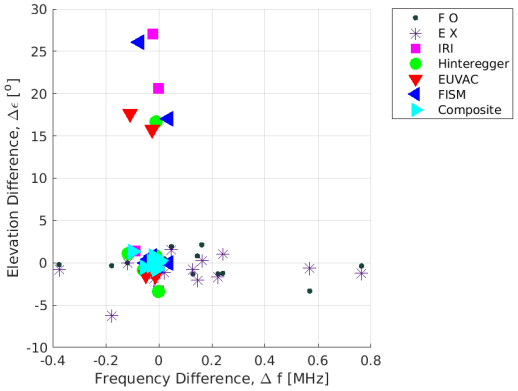

(f) Elevation - foE

Figure 38. The comparison of the variation from the flare peak to the start times for group delay, azimuth angle, and elevation angle to the difference in time for the hmE and foE for the same flare.

Overall, there were no indications of significant trends over time for the AoA parameters with regards to factors that form the basis of the calculations, thus indicating that the flare did not consistently affect the path of the signal between start and peak flare times. As there was no obvious trend between AoA parameters and the progression of the flare in terms of solar zenith angle and differential integrated flux, the focus turned to validating the ray tracing algorithm and its ability to correctly predict the CODAR data.

4.2.2 HF Circuit Parameter Statistics

Beginning with the AoA parameters, the full two hours of AoA parameters was compared to the equivalent time period for the CODAR data. The RMS scores are tabulated in Tables 9, 10, and 11 for group delay, azimuth angle, and elevation angle for each flare, and displayed in Figure 39 against the solar flare intensity. Each model for each flare was split between F-layer and E-layer, but only the F-layer O-mode is considered. Not all flares had scores for each model, as there was lack of data for either the CODAR or models in the cases where the score is empty. An RMS of zero implies a perfect fit, which gives a reference to determine how well each solar spectrum model informs the ray tracing algorithm. GLOW run with EUVAC and FISM showed the best fits for the F-layer over the entire two-hour period, while GLOW run with the Hinteregger method and IRI displayed the worst fits.

Table 9. The RMS values for the group delay for each flare for the *F*-layer O-mode depending on model, in units of [ms]. It follows from Table 8, so not all models have corresponding scores for the layer.

Date	IRI	Hinteregger	EUVAC	FISM	Composite
21-6-2015	–	–	–	–	–
3-7-2015	–	**0.21**	–	–	0.21
6-7-2015	–	–	–	–	–
21-8-2015	–	–	–	–	–
22-8-2015	0.16	0.19	**0.12**	0.14	0.15
1-10-2015	0.17	0.13	**0.09**	0.10	0.10
2-10-2015	0.21	0.21	0.23	**0.19**	0.21
2-10-2015	**0.13**	0.19	0.17	0.18	0.18
17-10-2015	–	–	–	–	–
31-10-2015	0.09	0.12	**0.05**	0.07	0.08
4-11-2015	–	0.12	0.13	**0.10**	0.11
9-11-2015	–	–	–	–	–
13-2-2016	0.09	0.14	0.11	**0.08**	0.11
14-2-2016	0.11	0.07	0.06	**0.05**	0.05

Table 10. The RMS values for the azimuth angle for each flare for the *F*-layer O-mode depending on model, in units of [°]. It follows from Table 8, so not all models have corresponding scores for the layer.

Date	IRI	Hinteregger	EUVAC	FISM	Composite
21-6-2015	–	–	–	–	–
3-7-2015	–	**2.84**	–	–	2.93
6-7-2015	–	–	–	–	–
21-8-2015	–	–	–	–	–
22-8-2015	3.43	3.38	**3.35**	3.36	3.36
1-10-2015	2.50	1.70	1.49	1.48	**1.48**
2-10-2015	**3.06**	3.16	3.16	3.08	3.14
2-10-2015	2.91	3.05	2.64	2.51	**2.51**
17-10-2015	–	–	–	–	–
31-10-2015	3.52	3.47	3.47	**3.47**	3.47
4-11-2015	–	**1.78**	1.79	1.78	1.78
9-11-2015	–	–	–	–	–
13-2-2016	2.27	2.36	2.25	2.25	**2.25**
14-2-2016	2.92	2.67	2.69	**2.66**	2.68

Table 11. The RMS values for the elevation angle for each flare for the *F*-layer O-mode depending on model, in units of [°]. It follows from Table 8, so not all models have corresponding scores for the layer.

Date	IRI	Hinteregger	EUVAC	FISM	Composite
21-6-2015	–	–	–	–	–
3-7-2015	–	**6.79**	–	–	6.89
6-7-2015	–	–	–	–	–
21-8-2015	–	–	–	–	–
22-8-2015	**4.23**	7.63	5.92	6.03	6.32
1-10-2015	5.94	4.78	4.12	**3.60**	4.16
2-10-2015	6.69	6.21	7.13	**5.77**	6.44
2-10-2015	**4.25**	6.32	6.24	6.09	6.18
17-10-2015	–	–	–	–	–
31-10-2015	**2.03**	5.22	3.30	3.43	3.81
4-11-2015	–	3.71	4.25	**3.34**	3.72
9-11-2015	–	–	–	–	–
13-2-2016	**2.25**	4.64	4.14	2.72	3.84
14-2-2016	2.20	3.10	3.14	**1.51**	2.54

Figure 39 also indicates that there is no correlation between the fit and the intensity of the flare, though this does not account for the absorption in the atmosphere included in the optical depth variable. It also further shows how IRI and GLOW run with Hinteregger display worse fits than the other models except for the elevation angle. Meanwhile, GLOW using EUVAC, FISM, and the composite demonstrated improved fits for the AoA parameters. There is an inverse relation for the *F*-layer azimuth angle between intensity and RMS score.

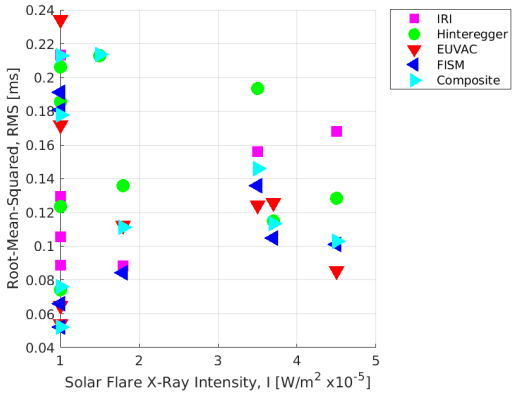

(a) Group Delay

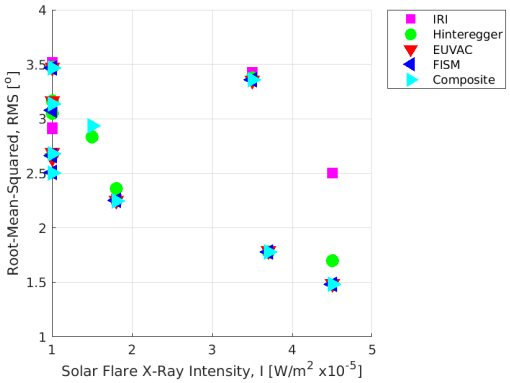

(b) Azimuth

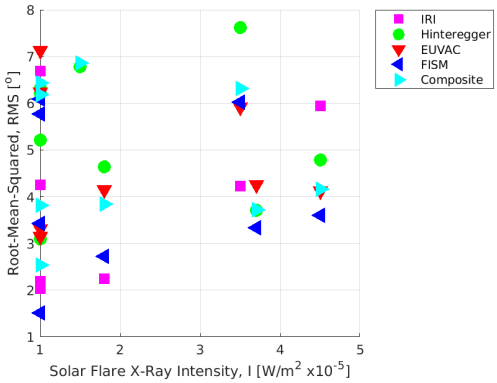

(c) Elevation

Figure 39. The RMS scores for the group delay, azimuth angle, and elevation angle for *F*-layer modes over the entire two-hour time period.

The PE scores were tabulated as well in Tables 12, 13, and 14 for the group delay, azimuth angle, and elevation angle for each model for each flare for the F-layer modes. As a reminder, a PE score of 1 again indicates a perfect fit, while a PE of 0 implies that the model had as decent a fit as just using the composite of the data, while a negative score indicates the model did not predict the data well. None of the models had consistent positive scores for any AoA parameter, and for the majority of cases were negative. IRI and GLOW ran with the Hinteregger method showed the

lowest PE scores, as indicated by the RMS scores previously, and again GLOW with EUVAC and FISM were either positive or near 0 for the majority of flares, showing promise for modeling the flare responses.

Table 12. The PE values for each flare for the *F*-layer O-mode depending on model for the group delay. It follows from Table 8, so not all models have corresponding scores for the layer.

Date	IRI	Hinteregger	EUVAC	FISM	Composite
21-6-2015	–	–	–	–	–
3-7-2015	–	0.29	–	–	0.29
6-7-2015	–	–	–	–	–
21-8-2015	–	–	–	–	–
22-8-2015	-0.25	-0.55	**0.00**	-0.09	-0.17
1-10-2015	-1.60	-0.99	**-0.32**	-0.57	-0.60
2-10-2015	-1.10	-1.03	-1.30	**-0.88**	-1.09
2-10-2015	**-2.29**	-3.72	-3.37	-3.60	-3.52
17-10-2015	–	–	–	–	–
31-10-2015	-0.89	-1.63	**-0.15**	-0.40	-0.62
4-11-2015	–	-1.49	-1.73	**-1.27**	-1.46
9-11-2015	–	–	–	–	–
13-2-2016	-2.48	-4.36	-3.42	**-2.32**	-3.39
14-2-2016	-1.48	-0.74	-0.52	**-0.22**	-0.22

Table 13. The PE values for the azimuth angle for each flare for the *F*-layer O-mode depending on model. It follows from Table 8, so not all models have corresponding scores for the layer.

Date	IRI	Hinteregger	EUVAC	FISM	Composite
21-6-2015	–	–	–	–	–
3-7-2015	–	**0.41**	–	–	0.39
6-7-2015	–	–	–	–	–
21-8-2015	–	–	–	–	–
22-8-2015	-1.04	-1.01	**-0.99**	-0.99	-1.00
1-10-2015	-0.24	0.16	0.26	0.27	**0.27**
2-10-2015	**-0.14**	-0.18	-0.18	-0.15	-0.17
2-10-2015	0.06	0.01	0.14	0.19	**0.19**
17-10-2015	–	–	–	–	–
31-10-2015	-1.90	-1.86	-1.86	**-1.85**	-1.86
4-11-2015	–	0.20	**0.20**	0.20	0.20
9-11-2015	–	–	–	–	–
13-2-2016	-0.45	-0.51	-0.44	-0.44	**-0.44**
14-2-2016	-0.81	-0.66	-0.67	**-0.65**	-0.66

Table 14. The PE values for the elevation angle for each flare for the *F*-layer O-mode depending on model. It follows from Table 8, so not all models have corresponding scores for the layer.

Date	IRI	Hinteregger	EUVAC	FISM	Composite
21-6-2015	–	–	–	–	–
3-7-2015	–	**-0.16**	–	–	-0.18
6-7-2015	–	–	–	–	–
21-8-2015	–	–	–	–	–
22-8-2015	**-0.28**	-1.31	-0.80	-0.83	-0.92
1-10-2015	-1.28	-0.83	-0.58	**-0.38**	-0.59
2-10-2015	-2.03	-1.81	-2.23	**-1.61**	-1.91
2-10-2015	**-1.36**	-2.51	-2.46	-2.38	-2.43
17-10-2015	–	–	–	–	–
31-10-2015	**-0.02**	-1.62	-0.66	-0.73	-0.92
4-11-2015	–	-1.59	-1.96	**-1.33**	-1.59
9-11-2015	–	–	–	–	–
13-2-2016	**-0.99**	-3.11	-2.68	-1.42	-2.41
14-2-2016	-0.32	-0.86	-0.89	**0.09**	-0.52

The PE scores are also displayed in Figure 40 against the solar flare intensity, demonstrating again the large errors of IRI and GLOW with the Hinteregger method. There was no obvious trend in the F-layer.

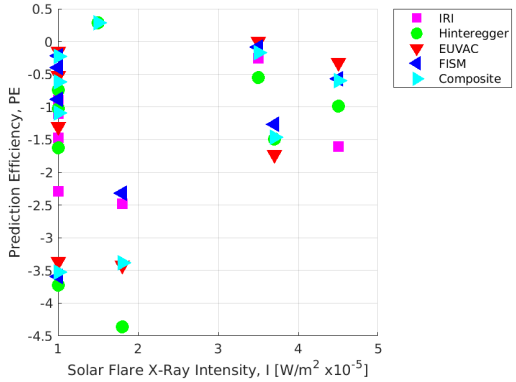

(a) Group Delay

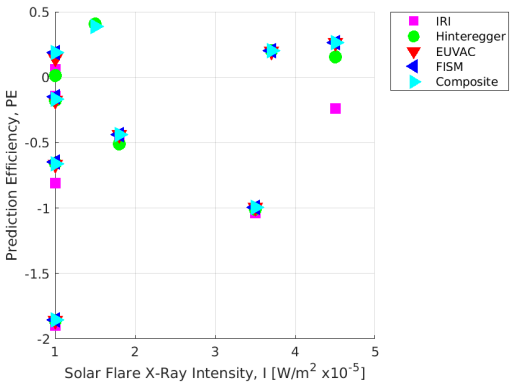

(b) Azimuth

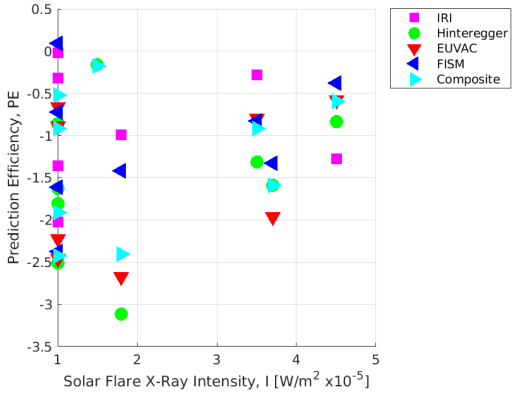

(c) Elevation

Figure 40. The PE scores for the group delay, azimuth angle, and elevation angle for the *F*-layer modes over the entire two-hour time period.

The RMS and PE scores were also calculated for the AoA parameters for the start and peak times for the flares for each layer. The RMS scores for each model are displayed in Table 15 for the E-layer and F-layer, respectively, and graphically shown in Figure 41. GLOW using EUVAC did the best for the F-layer, while GLOW ran

with the composite of all spectra did the best for the E-layer. The models did better at matching the group delay and azimuth at the peak time for the F-layer than the start time, but the opposite is true for the E-layer. Overall, however, IRI did the worst out of all the models for all the AoA parameters at both start and peak times, validating that GLOW is better at modeling the ionosphere response than IRI.

Table 15. The RMS values for each model for each AoA parameter, in [ms] for group delay, [°] for azimuth angle, and [°] for elevation angle for the *F*-layer O-mode.

Parameter	IRI	Hinteregger	EUVAC	FISM	Composite
τ_g **Start**	0.51	0.44	**0.36**	0.38	0.38
τ_g **Max**	0.32	0.32	**0.26**	0.30	0.30
α **Start**	**5.56**	5.69	5.65	5.65	5.63
α **Max**	5.07	**5.04**	5.07	5.04	5.05
ϵ **Start**	15.87	12.81	8.54	**8.24**	8.88
ϵ **Max**	10.77	9.57	9.31	**8.85**	9.17

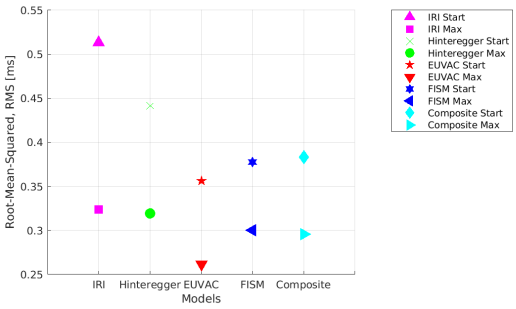

(a) Group Delay - F

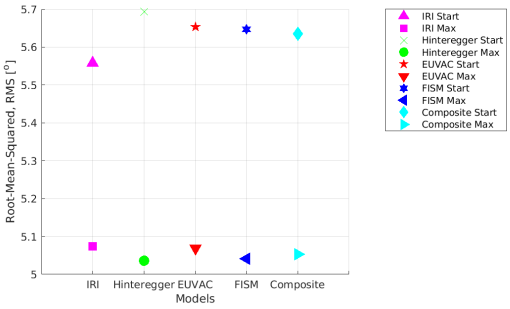

(b) Azimuth - F

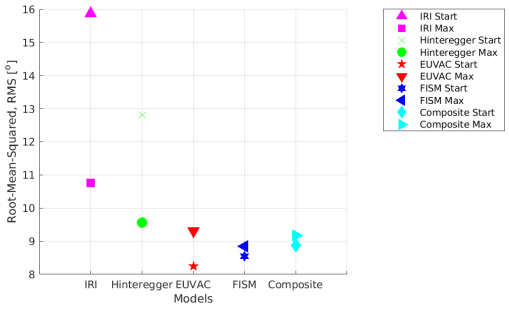

(c) Elevation - F

Figure 41. The RMS scores for AoA parameters for the start and peak flare times for the *F*-layer O-mode.

Finally, the PE scores were calculated and included in Table 16 for the F-layer and displayed in Figure 42. All but one PE score (for IRI) were positive, implying that the fits for all models for all AoA parameters for the start and peak times were good, with the azimuth angle being fit the best for all models for both layers. Overall, GLOW with EUVAC and the composite of all solar spectra had the highest PE scores and IRI had the lowest, which is not surprising given the IRI results for both the electron frequency profiles and ray tracing algorithm results.

Table 16. The PE values for each model for each AoA parameter for the *F*-layer O-mode.

Parameter	IRI	Hinteregger	EUVAC	FISM	Composite
τ_g **Start**	0.20	0.31	**0.44**	0.41	0.40
τ_g **Max**	0.47	0.48	**0.58**	0.51	0.52
α **Start**	**0.68**	0.67	0.67	0.67	0.67
α **Max**	0.73	**0.74**	0.73	0.74	0.73
ϵ **Start**	-0.01	0.19	**0.48**	0.46	0.44
ϵ **Max**	0.31	0.39	0.41	**0.44**	0.41

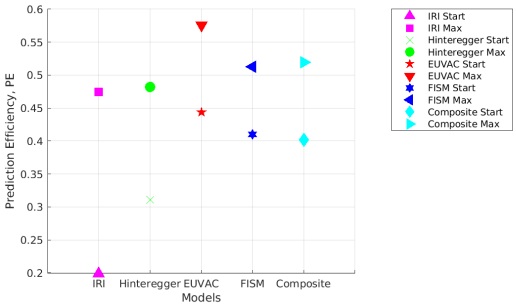

(a) Group Delay

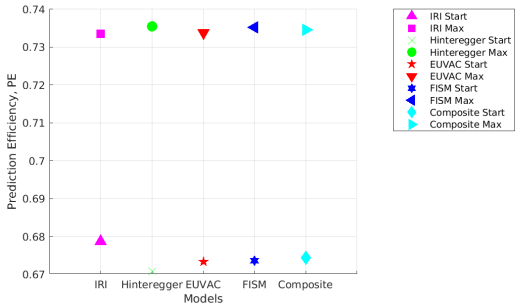

(b) Azimuth

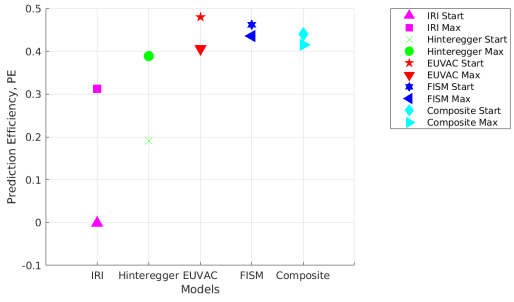

(c) Elevation

Figure 42. The PE scores for AoA parameters for the start and peak flare times for the *F*-layer O-mode.

Unlike the statistics for the electron frequency profiles, the models performed better at predicting the AoA parameters only at the start and peak flare times rather than the full time period.

4.3 Change in Time of AoA Parameters Analysis

The change in AoA parameters in time was examined in addition to confirm the findings of the analysis of the AoA parameters, as the slope can show if there are sudden changes before the flare or during the flare. The temporal slope was taken as the difference between consecutive points of the models and interpolated running average of the data, divided by the difference in consecutive times. The slopes of the pre-flare and flaring times were the maximum slope around the times, where the slope of the pre-flare was taken as the maximum slope within 5 minutes of the start of the flare, and the slope of the flaring time was the maximum slope between the start and peak flare times.

4.3.1 Data Slope Time Variation

The slopes of the AoA parameters were then compared to the same factors as the AoA parameters, starting in Figure 43 with the differential integrated flux. The slope of the AoA parameters have a positive relationship, but overall there was little variation in the slope for any of the AoA parameters regardless of change in flux. It is of note that IRI has the greatest change in slope, as it was the model that fluctuated between F-layer and E-layer modes the most.

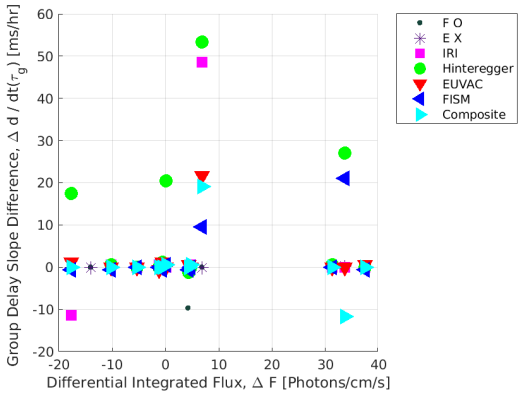

(a) Group Delay

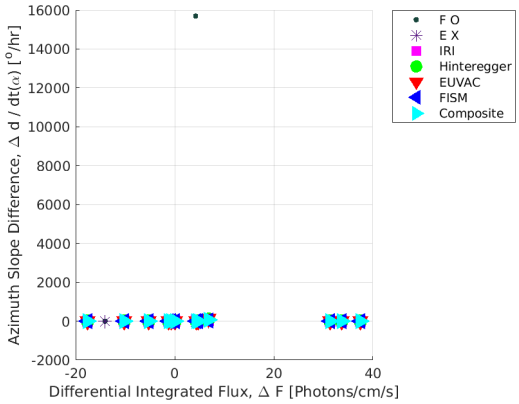

(b) Azimuth

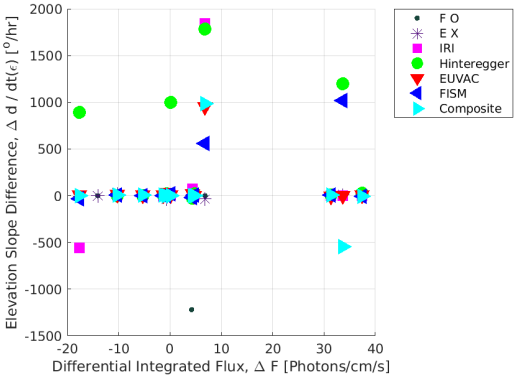

(c) Elevation

Figure 43. The comparison of the variation from the flare peak to the start times for the slope of the group delay, azimuth angle, and elevation angle to the differential integrated flux.

As expected, the zenith angle did not show any trend for the slopes in Figure 44 due to the minuscule variation in time.

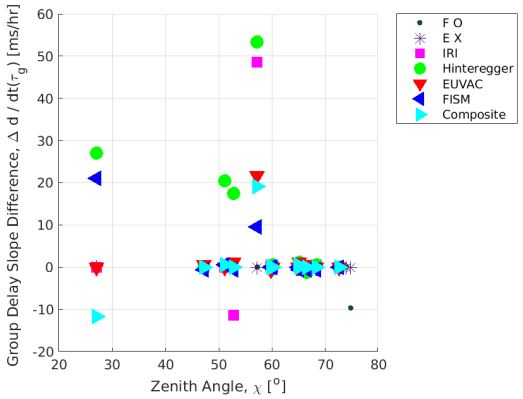

(a) Group Delay

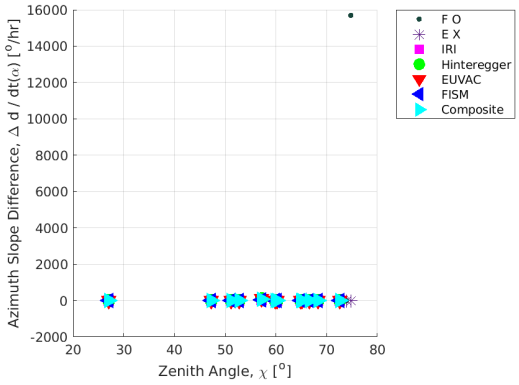

(b) Azimuth

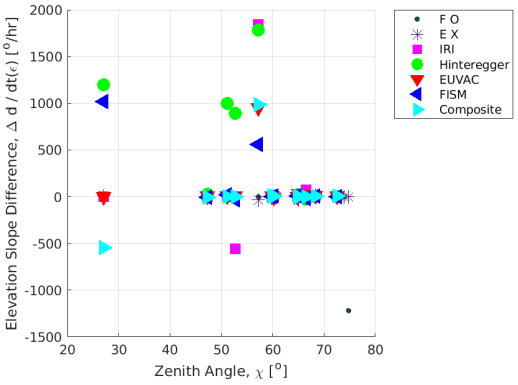

(c) Elevation

Figure 44. The comparison of the variation from the flare peak to the start times of the slope of the group delay, azimuth angle, and elevation angle to the solar zenith angle for the same flare.

The change in slope for the AoA parameters was compared to the change in hmE and foE from the GLOW results, shown in Figure 45. Similar to the results in Figure 38, there is an inverse relationship between the the change in hmE and the change in the slope of the AoA parameters, where if there is a change in hme, there is little to no change in the AoA parameters; and if there is a change in AoA parameters, there is little to no change in hmE.

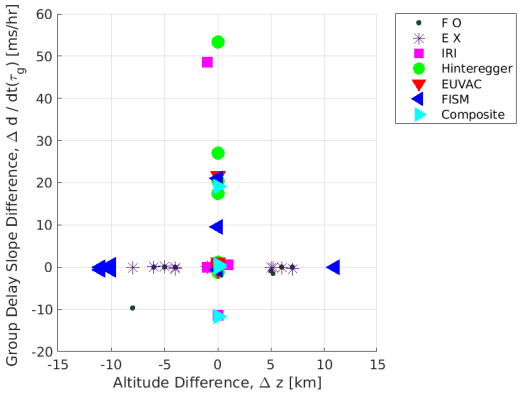

(a) Group Delay - hmE

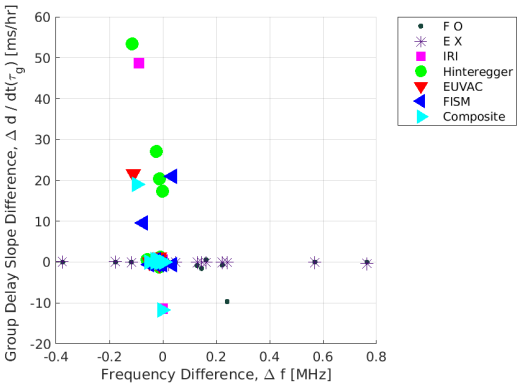

(b) Group Delay - foE

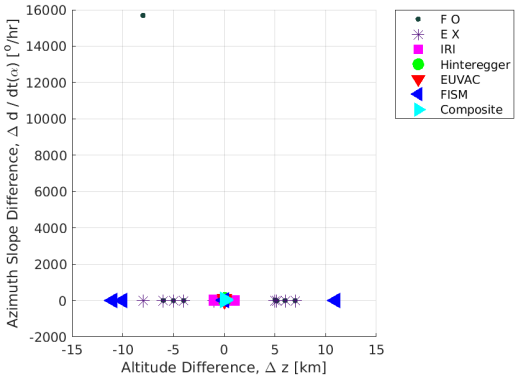

(c) Azimuth - hmE

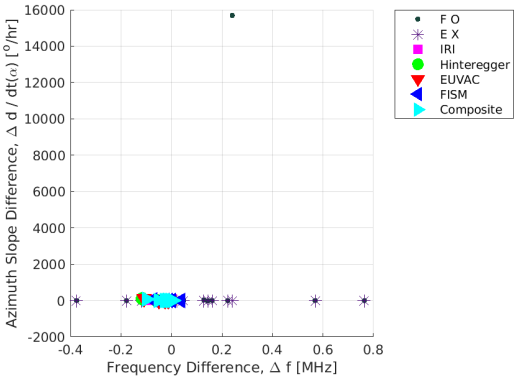

(d) Azimuth - foE

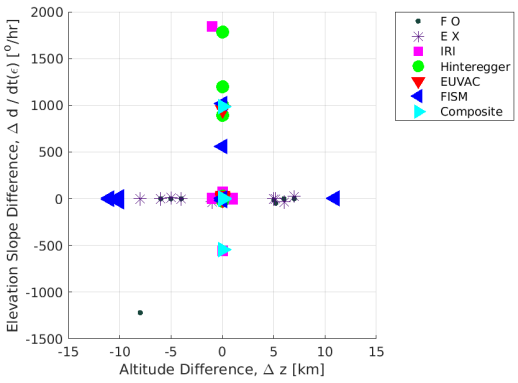

(e) Elevation - hmE

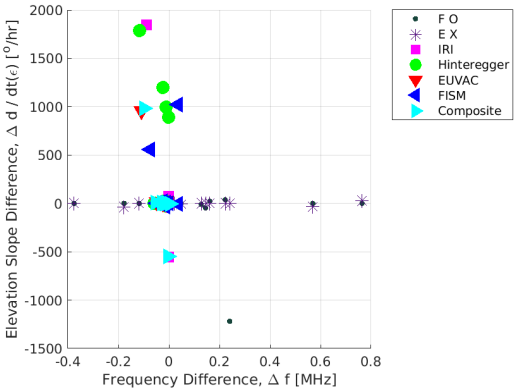

(f) Elevation - foE

Figure 45. The comparison of the variation from the flare peak to start times of the slope of the group delay, azimuth angle, and elevation angle to the difference in time of the hmE and foE for the same flare.

The change in time of the slope of the AoA parameters from the models was compared to the variation from the slope from the data in Figure 46 to display the accuracy of the models. Again, the model slopes were not split between E- and F-layers to preserve data integrity in time, which resulted in large model differences compared to the data difference. It is of note that the models do not vary in time when the data does vary, and vice versa. There is good agreement with theory in the data, as the change in slope in time is predominantly negative for group delay, with only two flares or 17% having positive slope changes. However, most flare data did not show significant slope changes in azimuth or elevation angles.

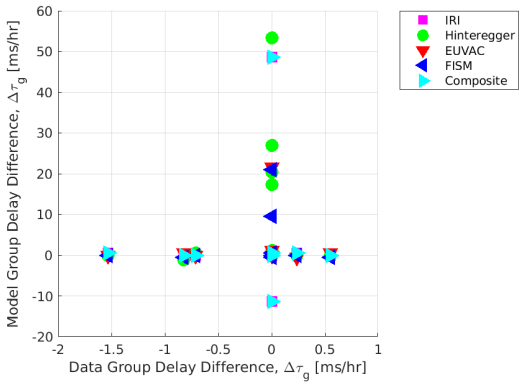

(a) Group Delay

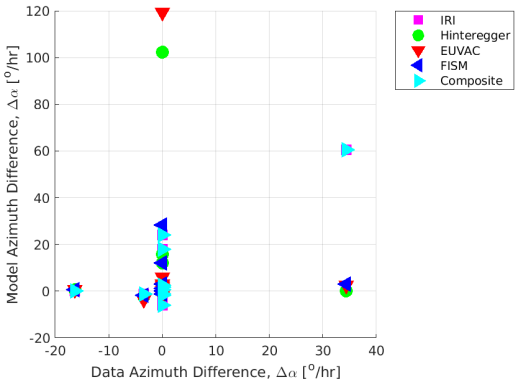

(b) Azimuth

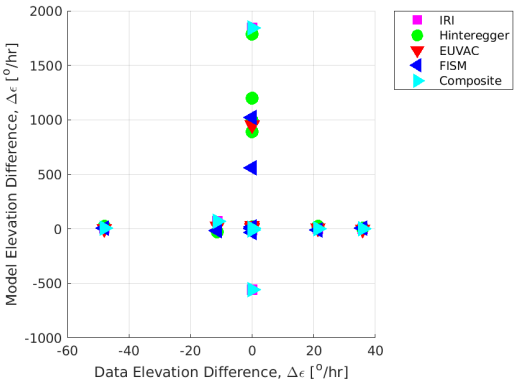

(c) Elevation

Figure 46. The comparison of the variation from the flare peak to start times for the slope of group delay, azimuth angle, and elevation angle to the the variation between peak and start times for the same parameter slopes from the CODAR data.

4.3.2 Data Slope Statistics

Lastly, the same statistical analysis was done for the slope of the AoA parameters, starting with the RMS scores for each model over the entire two-hour time period around the flare. The RMS score for each AoA parameter is shown in Tables 17, 18, and 19 for group delay, azimuth angle, and elevation angle respectively. These RMS values are significantly greater than those for the AoA parameters themselves. Again, this is good indication that IRI and GLOW run with the Hinteregger or EUVAC method are not designed to predict how the AoA parameters change throughout the flaring period due to the use of the daily $F_{10.7}$ index.

Table 17. The RMS values for the slope of the group delay for each flare for the *F*-layer O-mode depending on model, in units of [ms/hr]. It follows from Table 8, so not all models have corresponding scores for the layer.

Date	IRI	Hinteregger	EUVAC	FISM	Composite
21-6-2015	–	–	–	–	–
3-7-2015	**17.58**	22.02	22.56	23.41	22.52
6-7-2015	53.41	0.39	**0.33**	–	0.35
21-8-2015	–	–	–	–	–
22-8-2015	8.22	8.56	8.27	8.66	**7.70**
1-10-2015	**5.15**	8.38	7.18	8.29	6.51
2-10-2015	**5.02**	8.69	8.22	8.37	7.86
2-10-2015	**3.29**	4.65	5.01	5.72	4.05
17-10-2015	–	–	–	–	–
31-10-2015	**5.13**	6.88	7.16	8.29	5.50
4-11-2015	**1.42**	4.47	4.40	5.30	3.97
9-11-2015	–	–	–	–	–
13-2-2016	**4.55**	7.81	6.10	8.31	5.12
14-2-2016	**4.82**	8.92	6.47	7.47	5.73

Table 18. The RMS values for the slope of the azimuth angle for each flare for each layer depending on model, in units of [°/hr]. It follows from Table 8, so not all models have corresponding scores for the layer.

Date	IRI	Hinteregger	EUVAC	FISM	Composite
21-6-2015	–	–	–	–	–
3-7-2015	**186.37**	235.74	245.53	256.32	246.37
6-7-2015	1,511.28	80.70	**80.67**	–	**80.67**
21-8-2015	–	–	–	–	–
22-8-2015	191.58	162.49	160.27	161.35	**159.63**
1-10-2015	**117.95**	135.12	161.33	162.77	160.05
2-10-2015	**277.21**	366.69	341.90	336.39	354.03
2-10-2015	351.02	**65.46**	396.03	333.28	327.93
17-10-2015	–	–	–	–	–
31-10-2015	104.99	88.97	89.56	88.99	**87.56**
4-11-2015	**37.51**	208.52	209.73	209.01	208.10
9-11-2015	–	–	–	–	–
13-2-2016	143.65	**139.89**	142.78	143.36	140.71
14-2-2016	130.24	133.22	132.38	133.06	**129.58**

Table 19. The RMS values for the slope of the elevation angle for each flare for each layer depending on model, in units of [°/hr]. It follows from Table 8, so not all models have corresponding scores for the layer.

Date	IRI	Hinteregger	EUVAC	FISM	Composite
21-6-2015	–	–	–	–	–
3-7-2015	**439.28**	458.31	461.79	482.69	457.12
6-7-2015	1,080.74	27.14	25.43	–	**25.26**
21-8-2015	–	–	–	–	–
22-8-2015	294.26	224.23	217.84	240.68	**199.12**
1-10-2015	**238.75**	303.79	275.07	291.81	274.36
2-10-2015	**89.81**	221.68	210.71	221.92	206.51
2-10-2015	173.67	**167.21**	210.75	251.17	203.26
17-10-2015	–	–	–	–	–
31-10-2015	219.46	240.43	237.25	257.14	**208.62**
4-11-2015	**61.87**	127.88	144.30	155.74	126.31
9-11-2015	–	–	–	–	–
13-2-2016	**175.23**	265.35	218.32	259.87	187.12
14-2-2016	**171.47**	267.97	205.78	238.13	186.09

The RMS for the slope of the AoA parameters is compared to the solar flare intensity in Figure 47; no trends between RMS score and intensity were observed.

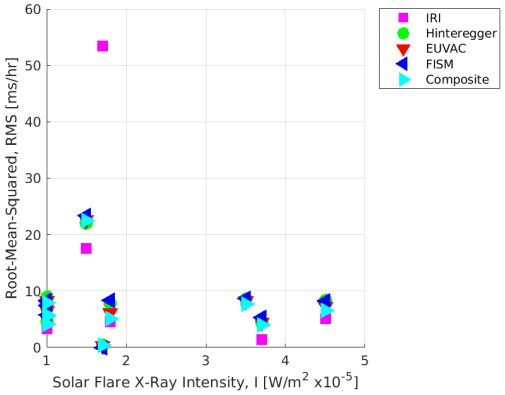

(a) Group Delay

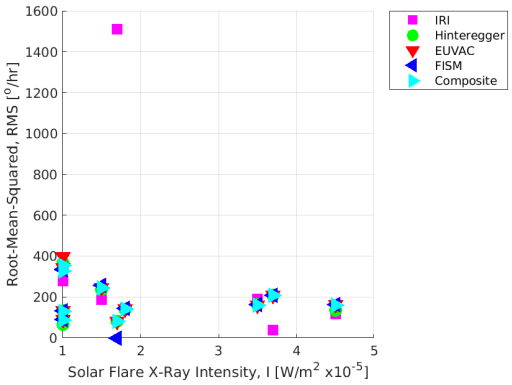

(b) Azimuth

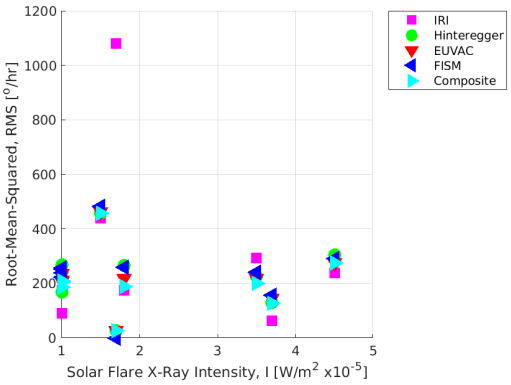

(c) Elevation

Figure 47. The RMS scores for the slope of the group delay, azimuth angle, and elevation angle for the *F*-layer O-mode over the entire two-hour time period.

The PE scores were also computed for the slopes of the AoA parameters and given in Tables 20, 21, and 22 for group delay, azimuth angle, and elevation angle. The majority of values were positive and above 0.90, indicating a good match between the change in AoA parameters and the change in the data over the entire time period for the F-layer O-mode. Only the flares on 21 June 2015, 3 July 2015, and 6 July 2015 have negative values and only for the slope in group delay.

Table 20. The PE values for the slope of the group delay for each flare for each layer depending on model. It follows from Table 8, so not all models have corresponding scores for the layer.

Date	IRI	Hinteregger	EUVAC	FISM	Composite
21-6-2015	–	–	–	–	–
3-7-2015	**0.99**	0.99	0.99	0.99	0.99
6-7-2015	0.90	1.00	**1.00**	–	**1.00**
21-8-2015	–	–	–	–	–
22-8-2015	0.99	0.99	0.99	0.99	**0.99**
1-10-2015	**0.99**	0.99	0.99	0.99	0.99
2-10-2015	**0.99**	0.98	0.98	0.98	0.99
2-10-2015	**0.99**	0.99	0.99	0.98	0.99
17-10-2015	–	–	–	–	–
31-10-2015	**0.99**	0.98	0.98	0.98	0.99
4-11-2015	**0.96**	0.89	0.89	0.87	0.90
9-11-2015	–	–	–	–	–
13-2-2016	**0.99**	0.98	0.98	**0.99**	**0.99**
14-2-2016	**0.99**	0.98	0.99	0.98	0.99

Table 21. The PE values for the slope of the azimuth angle for each flare for each layer depending on model. It follows from Table 8, so not all models have corresponding scores for the layer.

Date	IRI	Hinteregger	EUVAC	FISM	Composite
21-6-2015	–	–	–	–	–
3-7-2015	**0.99**	0.99	0.99	0.99	0.99
6-7-2015	0.92	**0.99**	**0.99**	–	**0.99**
21-8-2015	–	–	–	–	–
22-8-2015	0.99	0.99	**0.99**	0.99	**0.99**
1-10-2015	**0.99**	0.99	0.99	0.99	0.99
2-10-2015	**0.98**	0.97	0.98	0.98	0.98
2-10-2015	0.99	**1.00**	0.99	0.99	0.99
17-10-2015	–	–	–	–	–
31-10-2015	0.99	0.99	0.99	0.99	**0.99**
4-11-2015	**0.99**	0.99	0.99	0.99	0.99
9-11-2015	–	–	–	–	–
13-2-2016	0.99	**0.99**	0.99	0.99	**0.99**
14-2-2016	**0.99**	0.99	0.99	0.99	**0.99**

Table 22. The PE values for the slope of the elevation angle for each flare for each layer depending on model. It follows from Table 8, so not all models have corresponding scores for the layer.

Date	IRI	Hinteregger	EUVAC	FISM	Composite
21-6-2015	–	–	–	–	–
3-7-2015	**0.99**	0.99	0.99	0.99	0.99
6-7-2015	0.91	0.99	–	0.99	**0.99**
21-8-2015	–	–	–	–	–
22-8-2015	0.99	0.99	0.99	0.99	**0.99**
1-10-2015	**0.99**	0.99	0.99	0.99	0.99
2-10-2015	**0.99**	0.99	0.99	0.99	0.99
2-10-2015	0.99	**0.99**	0.99	0.99	0.99
17-10-2015	–	–	–	–	–
31-10-2015	0.99	0.99	0.99	0.99	**0.99**
4-11-2015	**0.99**	0.99	0.99	0.99	0.99
9-11-2015	–	–	–	–	–
13-2-2016	**0.99**	0.98	0.99	0.99	0.99
14-2-2016	**0.99**	0.98	0.98	0.99	0.99

The PE scores were similarly compared against the solar flare intensity in Figure 48. Similar to previous results, there was no trend in the data, but it serves to again verify that IRI does not capture the change in AoA parameters.

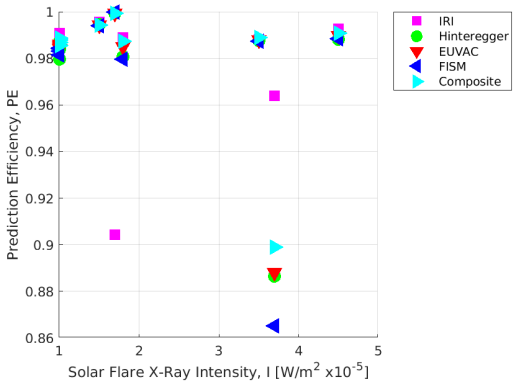

(a) Group Delay

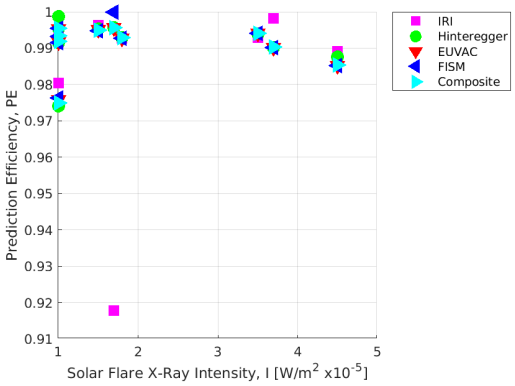

(b) Azimuth

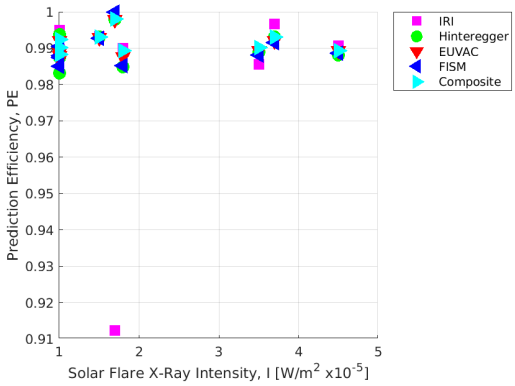

(c) Elevation

Figure 48. The PE scores for the slope of the group delay, azimuth angle, and elevation angle for the *F*-layer O-mode over the entire two-hour time period.

The RMS scores were then calculated for just the change in AoA parameter slopes around the start and peak flare times for the F-layer O-mode, shown in Table 23. It is also graphically displayed in Figure 49. IRI had the highest RMS for group delay for the F-layer. However, for the azimuth and elevation angle, all models performed about equally well, but all were significantly worse in modeling the change around the start time over the peak time.

Table 23. The RMS values for each model for each slope of the AoA parameter, in [ms/hr] for group delay, [°/hr] for azimuth angle, and [°/hr] for elevation angle for the *F*-layer.

Parameter	IRI	Hinteregger	EUVAC	FISM	Composite
$\frac{d}{dt}\tau_g$ **Pre**	13.57	8.92	9.02	**7.77**	9.14
$\frac{d}{dt}\tau_g$ **Flare**	50.08	**47.13**	51.82	48.37	52.23
$\frac{d}{dt}\alpha$ **Pre**	**3,008.07**	3,010.59	3,009.24	3,009.46	3,011.25
$\frac{d}{dt}\alpha$ **Flare**	**2.639.62**	2,654.54	2,654.97	2,654.62	2,656.99
$\frac{d}{dt}\epsilon$ **Pre**	**789.25**	1,302.77	1,303.67	1,158.11	1,306.50
$\frac{d}{dt}\epsilon$ **Flare**	**1,624.44**	1,801.34	1,994.04	1,908.38	2,003.57

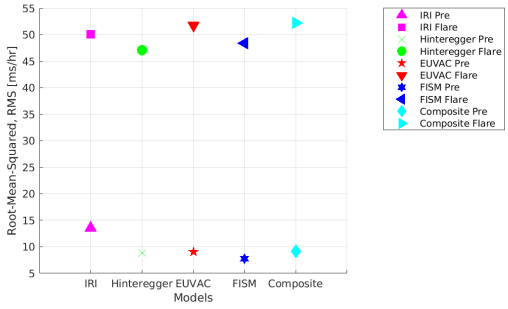

(a) Group Delay

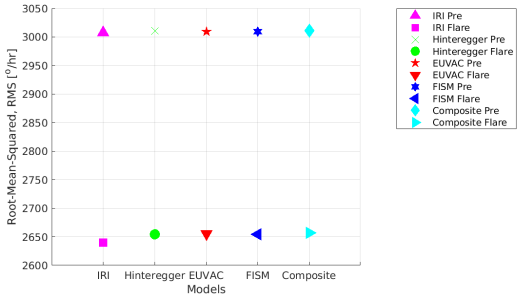

(b) Azimuth

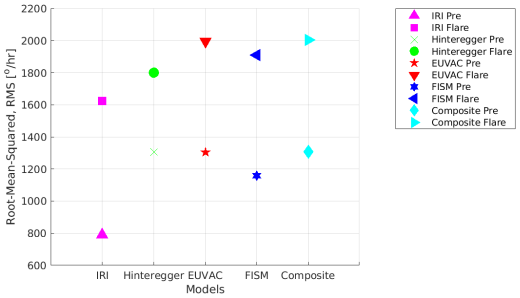

(c) Elevation

Figure 49. The RMS scores for the slope of the AoA parameters for the start and peak flare times for the *F*-layer O-mode.

Lastly, the PE scores for the change in AoA parameters for the start and peak times were computed and tabulated in Table 24 and shown in Figure 50. The F-layer group delay changes have positive PE scores, implying that these were more accurately determined. Unfortunately, this was not true for the other AoA parameter slopes.

Table 24. The table of PE values for each model for each AoA parameter for the F-layer.

Parameter	IRI	Hinteregger	EUVAC	FISM	Composite
$\frac{d}{dt}\tau_g$ **Pre**	0.84	0.90	0.89	**0.91**	0.89
$\frac{d}{dt}\tau_g$ **Flare**	-0.38	**-0.30**	-0.43	-0.34	-0.44
$\frac{d}{dt}\alpha$ **Pre**	**-0.42**	-0.42	-0.42	-0.42	-0.42
$\frac{d}{dt}\alpha$ **Flare**	**-1.07**	-1.08	-1.08	-1.08	-1.08
$\frac{d}{dt}\epsilon$ **Pre**	**0.41**	0.02	0.02	0.13	0.02
$\frac{d}{dt}\epsilon$ **Flare**	**-0.51**	-0.67	-0.85	-0.77	-0.86

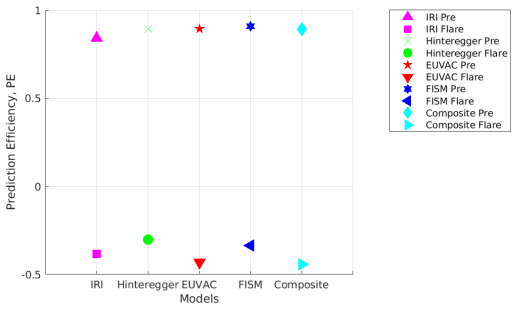

(a) Group Delay

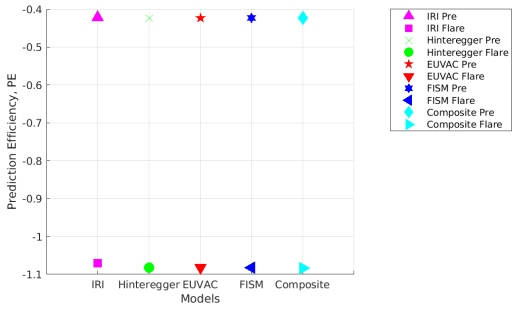

(b) Azimuth

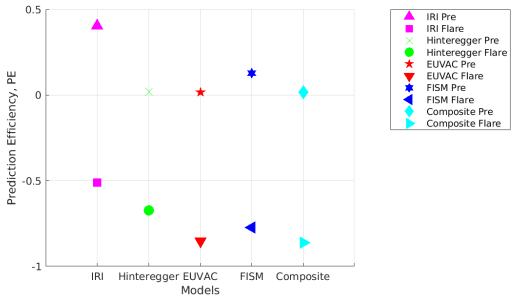

(c) Elevation

Figure 50. The PE scores for the change in AoA parameters for the start and peak flare times for the *F*-layer O-mode.

4.4 Discussion

The hypothesis of this research was that the change in solar spectrum driven by the increase in EUV activity from an M-class solar flare would modify the ionosphere enough to change the response of the CODAR and affect the HF circuit parameters. The goal was to attempt to model this perceived change in response. The expectation was to see a clear decrease in group delay and elevation angle during the flare, and possibly some decrease in azimuth angle. However, there was no consistent trend between start and peak flare times for any of the AoA parameters or even the change in AoA parameters. Some flares exhibited almost no change from start to peak.

Others showed drastic decreases in all AoA parameters at the start of the flare that led to an absence of data later in time as the ionosphere absorbed the signal, as shown in flares like on 21 August 2015 or 9 November 2015, where the latter demonstrated a loss of signal at the start for all AoA parameters for both layers. There was also no trend between the models or data and the zenith angle or change in intensity, although a correlation cannot be made without examining the neutral densities. Some attempt to account for variations based on time of day were made by comparing to the solar zenith angle, but no attempts were made for potential seasonal variations.

Despite not showing any significant trend, the results did show an ability to model the CODAR data using GLOW to determine the electron frequency profiles. This further validates the ray tracing algorithm and the GLOW model's ability to model physical processes. It also increases the confidence in the analysis of the trends or lack of that were observed. While the PE scores for the AoA parameters over the entire time frame were less than zero, they were significantly more capable to determine the AoA parameters at the start and peak flare time; conversely, the models were more capable of predicting the overall change in AoA parameters over the time period. Despite validation having been a part of Jones and Stephenson (1975), Dao et al. (2016), and Burg (2020), none of these studies used GLOW or examined the affect of various solar spectrum schemes on the results of the ray tracing algorithm. As GLOW consistently outperformed IRI in all instances, it can be noted that GLOW does produce electron frequency profiles that show improved performance during M-class flares.

As there were no X-class flares that took place over the course of the AoA study, it is difficult to extrapolate if a stronger intensity would have a more consistent affect on the HF circuit response. However, as the intensities of the M-class flares did not reflect a trend, it is hypothesized that the X-class flares would either show a loss

of signal entirely or also show no correlation between intensity and change in AoA parameters.

V. Conclusions

5.1 Final Thoughts

The primary question this research sought to answer was how solar flares affected the ionosphere and HF skywave circuits. Particularly, given the available data, it was to determine if M-class solar flares were strong enough to enhance the ionosphere and disturb the HF circuit parameters. The electron frequency profiles generated from various ionosphere and solar spectrum models and the ionosonde data from the duration of a collection of 14 M-class flares were temporally analyzed to determine if there was any variation between the pre-flare and peak flare times. An additional 14 X-class flares were analyzed to serve as a comparison between solar intensities. However, only the M-class flares were used in the ray tracing algorithm to produce the AoA parameters as no X-class flares occurred during the collection of the CODAR data used to validate the results.

The final analysis for both the electron frequency profiles and the AoA parameters showed that there was no consistent trend or correlation for the difference between the start time of the solar flare and the peak time, for any of the five variables - hmE, foE, group delay, azimuth angle, and elevation angle. The only consistent change between start and peak flare time was in the solar X-ray spectrum between 0.5 and 15 Å. Often, there would be a perturbation between the overall electron frequency profiles, but the change was often minor for M-class flares and often would decrease in E-layer peak frequency between start and peak times. An idealized case with constantly increasing solar flux demonstrated that the group delay and elevation angle should decrease over time. The decrease in group delay was demonstrated in the data for 7 flares, but the decrease in elevation angle was only seen in the data for 5. Further, the models did not reflect this decrease and instead showed either

little variation or an increase in time. It is therefore concluded that flares should be examined on a case-by-case basis for interesting variations, instead of concluding with a generalized trend on how low-intensity solar flares affect either the electron frequency profiles or AoA parameters. While the generalized trend would be more useful to operators and forecasters, the data sets available for HF parameters are not large enough and complete enough to control for seasonal or solar cycle variations or to make statistically significant fits of the data during solar flares. If a large data set was collected, or enough smaller studies were aggregated and controlled for variations in the experiments, the methodology used here could reveal potential trends.

It is of note that another question arose from the analysis of the data, namely if M-class flares can be used in lieu of X-class flares. X-class flares in particular are difficult to analyze in an ensemble as measurement devices often experience blackouts during intense flaring periods and possible subsequent CME events, but X-class flares are the most interesting and important events to analyze as they cause the most damage. M-class flares, in contrast, are low enough in intensity to typically not cause instrument blackout but not intense enough to observe drastic changes in the ionosphere. However, it was shown that M-class flares can show enough variation to use in data analysis provided the flare is strong enough in intensity, as illustrated by the increase in solar flux in the same wavelength bins as X-class flares. This shows that the M-class flares would affect the ionosphere at similar altitudes as X-class flares, particularly in the D- and E-layers. A collection of 14 X-class flares were used to produce electron frequency profiles to compare to those of the M-class flares. Neither the X-class flares nor the M-class flares demonstrated a clear trend in hmE or foE variation in time, so these parameters cannot determine if the M-class flares display similar ionospheric responses to X-class flares. It is also important to note that the variables used here to determine trend are not the ideal variables, as it was

limited to only the E-layer for the electron frequency profiles. Further, the variables of solar intensity and solar zenith angle only comprise a portion of the relationship to the flux in the ionosphere; the neutral density is another significant variable that was not considered due to the lack of neutral density calculations in the models used.

The analysis did serve as a comprehensive validation study for modeling M-class flares and for the ray tracing algorithm's use with extreme space weather phenomena like solar flares, which was the second research objective. GLOW did extremely well modeling the electron frequency profiles between 90 km and 640 km as the PE scores were positive, and the average of all the solar spectra improved the performance of the model considerably. It was expected that IRI and GLOW using the Hinteregger method and EUVAC would show larger errors than GLOW using FISM since the first three models rely on a daily static solar flux with temporal changes resulting from observed daily ionospheric cycles, while the latter has a solar flux that varies each minute. Surprisingly, IRI displayed significant ability to model the electron frequency profiles and marginally outperformed GLOW at modeling the slopes of the AoA parameters, as it was expected that GLOW ran with FISM would best emulate the small changes in time. However, IRI showed larger errors in predicting the AoA parameters, which indicated that GLOW is the preferred model to use with the ray tracing algorithm. Further, though the PE scores for the AoA parameters were mostly negative for individual flares, the changes in parameters between the peak and start flare time had overwhelmingly positive PE scores, with GLOW using EUVAC having the best fits. The slopes of the AoA parameters in time for individual flares additionally had positive PE scores, with the majority being between 0.90 and 1.00 and IRI and the composite from GLOW matching the data the best. Overall, the solar spectra and the results produced from them demonstrated that the models work well at predicting measured data. This is in part due to the lower intensity of

the solar flares examined, which resulted in smaller variations in electron frequency profiles than would typically be observed during larger flares or other space weather events like a geomagnetic storm or traveling ionospheric disturbance. Thus, the electron frequency profiles during M-class flares closely resemble a pre-flare ionosphere's profiles, and thus the models that only have solar flux variation on a day timescale performed as well or better than the model with minute timescale variation.

There were some issues concerning the data that affected the results. Most notably, that despite the ray tracing algorithm having been set to calculate the O-mode solutions, some model results were more closely aligned with the E-layer X-mode data from the CODAR data set. An absolute difference method was employed to separate the two modes, but error was introduced by this biasing. Further, some results were affected when the data was not separated to preserve temporal integrity, such as when the difference between the AoA parameters at the start and peak times was taken, as it is likely some differences were between O-modes and X-modes. There was also the issue of instrument blackout, which still occurred for some ionosonde and CODAR measurements. This missing data was either interpolated or the flare was removed completely from the analysis. Overall, the ensemble of 14 M-class flares for the electron frequency profile analysis and the 12 M-class flares for the HF circuit analysis is larger than typical studies, but not large enough to draw concrete conclusions or statistical significance.

5.2 Future Recommendations

The first recommendation for future research is to use solar spectrum data from satellites to inform GLOW using its user-supplied spectrum function instead of using FISM. For example, instruments from the SORCE SOLSTICE, SIM, and XPS experiments (Mauceri et al., 2020) contain irradiance measurements from 0.1 nm to 2400 nm, but exclude 34-115 nm. This has the potential to produce more accurate electron frequency profiles, but also risks losing spectrum data during instrument failure or during extreme events that might saturate the instruments.

It would also be worthwhile to compare GLOW's electron frequency profiles to those from more robust models such as TIE-GCM, USU-GAIM, GITM, or SAMI3. This comparison would show how accurate GLOW is compared to how quickly it runs. It would also be of note how GLOW compares to the other prominent quick-run model, NeQuick. This would provide a more thorough study as to which ionosphere model would perform best with the ray tracing algorithm.

Considering the ray tracing algorithm, it would be beneficial to compare the O-modes and X-modes produced from the algorithm to the data, as the CODAR data set contained both O- and X-mode data and contained X-mode data for both the E-layer and F-layer. The X-mode is not as well studied as the O-mode, but it might provide more insight as to what is occurring during a flare or other extreme space weather event. Additional data sets from other HF circuit experiments would also contribute to this understanding, and perhaps provide more context or trends if they contain additional solar flares. A data set with X-class flares would be useful to compare with the response to M-class flares.

Lastly, modifying GLOW to include transport equations would allow increased confidence in the F-layer AoA parameters, as GLOW currently only calculates to 200 km before splicing in the results from IRI. Adding the heat equations would

give additional temperature variations that might be missed as well. Neutral density calculations would provide much needed information to determine the optical depth and to further analyze the trend in electron frequency profiles and AoA parameters. Currently, GLOW relies on calculations from the NRLMSISE-00 model and do not vary with solar spectra variations. Full-physics models contain additional chemistry modules that do account for this, but this addition might be beyond GLOW's intent as a modeling package for airglow calculations. An alternative to modifying GLOW would be to modify an existing full-physics model to accept a user-supplied solar spectrum file instead of relying on either empirical calculations using the $F_{10.7}$ index or using a built-in EUVAC module. There are methods to do this for TIE-GCM, but it is not as simple a process as it is for GLOW.

Appendix A

A.1 Hinteregger Method Bins

The Hinteregger method was one of the earliest models to compute the EUV spectrum and relies on a fit of the reference spectrum F74113 and coefficients c_1 and c_2 (Hinteregger et al., 1981). The values for a 22-bin scheme are found in Solomon and Qian (2005) and another fit is described in the source files for the GLOW model; both are reproduced in Tables 25 and 26, respectively.

Table 25. The parameters for the Hinteregger method, described by Solomon and Qian (2005) for a 22-bin scheme.

Bin, i	**Wavelength**, λ [nm]	**F74113** [photons cm^{-2} s^{-1}]	c_1 [photons cm^{-2} s^{-1}]	c_2 [photons cm^{-2} s^{-1}]
1	0.05-0.4	5.010×10^{1}	0.000×10^{0}	2.984×10^{2}
2	0.4-0.8	1.000×10^{4}	0.000×10^{0}	7.600×10^{3}
3	0.8-1.8	2.000×10^{6}	0.000×10^{0}	4.600×10^{5}
4	1.8-3.2	7.600×10^{6}	7.470×10^{5}	9.220×10^{5}
5	3.2-7.0	1.659×10^{8}	6.623×10^{7}	4.293×10^{6}
6	7.0-15.5	4.012×10^{8}	1.662×10^{8}	5.678×10^{6}
7	15.5-22.4	2.078×10^{9}	1.510×10^{8}	6.273×10^{7}
8	22.4-29.0	1.724×10^{9}	3.310×10^{8}	9.834×10^{7}
9	29.0-32.0	6.793×10^{9}	2.220×10^{9}	4.286×10^{7}
10	32.0-54.0	2.750×10^{9}	5.469×10^{8}	1.080×10^{8}
11	54.0-65.0	5.035×10^{9}	2.969×10^{9}	1.590×10^{7}
12	65.0-79.8	1.562×10^{9}	6.938×10^{8}	8.208×10^{6}
13	65.0-79.8	1.264×10^{9}	6.690×10^{8}	5.445×10^{5}
14	79.8-91.3	3.011×10^{9}	3.011×10^{9}	0.000×10^{0}
15	79.8-91.3	4.661×10^{9}	4.213×10^{9}	0.000×10^{0}
16	79.8-91.3	1.020×10^{9}	1.020×10^{9}	0.000×10^{0}
17	91.3-97.5	5.441×10^{8}	4.187×10^{8}	0.000×10^{0}
18	91.3-97.5	1.483×10^{9}	1.307×10^{9}	0.000×10^{0}
19	91.3-97.5	8.642×10^{8}	8.440×10^{8}	0.000×10^{0}
20	97.5-98.7	6.056×10^{9}	3.671×10^{9}	0.000×10^{0}
21	98.7-102.7	5.569×10^{9}	4.984×10^{9}	0.000×10^{0}
22	102.7-105.0	6.309×10^{9}	5.796×10^{9}	0.000×10^{0}

Table 26. The parameters for the Hinteregger method, described in the GLOW files.

Bin, i	**Wavelength**, λ [nm]	**F74113** [photons cm^{-2} s^{-1}]	c_1 [photons cm^{-2} s^{-1}]	c_2 [photons cm^{-2} s^{-1}]
1	0.05-0.1	0.000×10^{0}	0.000×10^{0}	0.000×10^{0}
2	0.1-0.2	1.000×10^{-1}	0.000×10^{0}	4.800×10^{0}
3	0.2-0.4	5.000×10^{1}	0.000×10^{0}	2.900×10^{2}
4	0.4-0.8	1.000×10^{4}	0.000×10^{0}	7.600×10^{3}
5	0.8-1.8	2.000×10^{6}	0.000×10^{0}	4.600×10^{5}
6	1.8-2.3	9.000×10^{5}	0.000×10^{0}	2.300×10^{5}
7	2.3-3.2	6.700×10^{6}	7.470×10^{5}	6.920×10^{5}
8	3.2-4.4	3.800×10^{6}	0.000×10^{0}	4.350×10^{5}
9	4.4-6.0	8.560×10^{7}	3.229×10^{7}	2.175×10^{6}
10	6.0-7.0	7.650×10^{7}	3.395×10^{7}	1.683×10^{6}
11	7.0-8.0	7.930×10^{7}	4.706×10^{7}	1.127×10^{6}
12	8.0-9.0	6.570×10^{7}	1.228×10^{7}	1.202×10^{6}
13	9.0-10.0	9.400×10^{7}	3.860×10^{7}	8.247×10^{5}
14	10.0-11.0	3.090×10^{7}	1.266×10^{7}	1.896×10^{5}
15	11.0-12.0	2.130×10^{7}	1.736×10^{7}	3.780×10^{3}
16	12.0-13.0	1.590×10^{7}	1.237×10^{7}	1.260×10^{3}
17	13.0-14.0	1.060×10^{7}	8.589×10^{6}	0.000×10^{0}
18	14.0-15.0	5.590×10^{7}	9.379×10^{6}	9.296×10^{5}
19	15.0-16.0	6.100×10^{7}	7.912×10^{6}	2.492×10^{6}
20	16.0-17.0	1.322×10^{8}	6.989×10^{7}	7.400×10^{5}
21	17.0-18.0	8.460×10^{8}	5.053×10^{7}	1.161×10^{7}
22	18.0-19.0	4.458×10^{8}	7.553×10^{6}	1.199×10^{7}
23	19.0-20.0	3.568×10^{8}	0.000×10^{0}	1.597×10^{7}
24	20.0-21.0	1.420×10^{8}	2.299×10^{7}	9.957×10^{6}
25	21.0-22.0	9.240×10^{7}	0.000×10^{0}	8.507×10^{6}
26	22.0-23.0	2.388×10^{8}	6.350×10^{7}	6.124×10^{6}
27	23.0-24.0	1.319×10^{8}	5.611×10^{7}	2.565×10^{6}
28	24.0-25.0	3.184×10^{8}	6.340×10^{7}	8.582×10^{6}
29	25.0-26.0	5.497×10^{8}	8.695×10^{7}	1.808×10^{7}
30	26.0-27.0	1.052×10^{8}	0.000×10^{0}	8.750×10^{6}
31	27.0-28.0	2.725×10^{8}	6.101×10^{7}	1.379×10^{7}
32	28.0-29.0	1.367×10^{8}	0.000×10^{0}	4.332×10^{7}
33	29.0-30.0	1.477×10^{8}	0.000×10^{0}	4.035×10^{6}
34	30.0-31.0	6.235×10^{9}	2.220×10^{9}	2.820×10^{7}
35	31.0-32.0	4.098×10^{8}	0.000×10^{0}	1.063×10^{7}
36	32.0-33.0	4.700×10^{6}	0.000×10^{0}	5.170×10^{6}
37	33.0-34.0	3.400×10^{7}	0.000×10^{0}	3.400×10^{7}
38	34.0-35.0	4.176×10^{8}	0.000×10^{0}	1.089×10^{7}
39	35.0-36.0	1.034×10^{8}	0.000×10^{0}	3.619×10^{6}
40	36.0-37.0	8.325×10^{8}	0.000×10^{0}	2.947×10^{7}

41	37.0-38.0	0.000×10^{0}	0.000×10^{0}	0.000×10^{0}
42	38.0-39.0	0.000×10^{0}	0.000×10^{0}	0.000×10^{0}
43	39.0-40.0	1.560×10^{7}	7.504×10^{6}	0.000×10^{0}
44	40.0-41.0	1.791×10^{8}	8.615×10^{7}	0.000×10^{0}
45	41.0-42.0	8.800×10^{6}	0.000×10^{0}	3.590×10^{6}
46	42.0-43.0	0.000×10^{0}	0.000×10^{0}	0.000×10^{0}
47	43.0-44.0	2.047×10^{8}	0.000×10^{0}	1.973×10^{6}
48	44.0-45.0	0.000×10^{0}	0.000×10^{0}	0.000×10^{0}
49	45.0-46.0	9.100×10^{6}	7.553×10^{6}	0.000×10^{0}
50	46.0-47.0	1.999×10^{8}	1.577×10^{7}	2.279×10^{6}
51	47.0-48.0	3.240×10^{7}	2.689×10^{7}	0.000×10^{0}
52	48.0-49.0	6.500×10^{7}	4.841×10^{7}	0.000×10^{0}
53	49.0-50.0	1.688×10^{8}	7.578×10^{7}	1.162×10^{7}
54	50.0-51.0	1.434×10^{8}	8.728×10^{7}	0.000×10^{0}
55	51.0-52.0	3.350×10^{7}	2.446×10^{7}	0.000×10^{0}
56	52.0-53.0	1.112×10^{8}	3.137×10^{7}	5.340×10^{6}
57	53.0-54.0	1.860×10^{8}	1.358×10^{8}	0.000×10^{0}
58	54.0-55.0	2.320×10^{7}	7.656×10^{6}	0.000×10^{0}
59	55.0-56.0	8.839×10^{8}	4.107×10^{8}	0.000×10^{0}
60	56.0-57.0	1.336×10^{8}	8.231×10^{7}	0.000×10^{0}
61	57.0-58.0	6.890×10^{7}	5.719×10^{7}	0.000×10^{0}
62	58.0-59.0	1.591×10^{9}	1.566×10^{9}	0.000×10^{0}
63	59.0-60.0	2.092×10^{8}	9.479×10^{7}	0.000×10^{0}
64	60.0-61.0	4.500×10^{8}	0.000×10^{0}	1.260×10^{7}
65	61.0-62.0	1.670×10^{7}	6.931×10^{6}	0.000×10^{0}
66	62.0-63.0	1.600×10^{9}	7.095×10^{8}	3.301×10^{6}
67	63.0-64.0	2.490×10^{7}	2.067×10^{7}	0.000×10^{0}
68	64.0-65.0	3.300×10^{7}	1.370×10^{7}	0.000×10^{0}
69	65.0-66.0	2.180×10^{7}	1.552×10^{7}	0.000×10^{0}
70	66.0-67.0	6.200×10^{6}	2.573×10^{6}	0.000×10^{0}
71	67.0-68.0	1.060×10^{7}	5.279×10^{6}	0.000×10^{0}
72	68.0-69.0	1.392×10^{8}	5.298×10^{7}	3.411×10^{5}
73	69.0-70.0	4.350×10^{7}	1.735×10^{7}	2.034×10^{5}
74	70.0-71.0	4.022×10^{8}	1.732×10^{8}	0.000×10^{0}
75	71.0-72.0	8.010×10^{7}	4.281×10^{7}	0.000×10^{0}
76	72.0-73.0	1.860×10^{7}	1.860×10^{7}	0.000×10^{0}
77	73.0-74.0	2.420×10^{7}	2.420×10^{7}	0.000×10^{0}
78	74.0-75.0	3.060×10^{7}	3.060×10^{7}	0.000×10^{0}
79	75.0-76.0	1.418×10^{8}	1.025×10^{8}	0.000×10^{0}
80	76.0-77.0	3.973×10^{8}	2.340×10^{8}	0.000×10^{0}
81	77.0-78.0	3.085×10^{8}	6.600×10^{7}	5.335×10^{6}
82	78.0-79.0	6.392×10^{8}	2.732×10^{8}	2.873×10^{6}
83	79.0-80.0	5.858×10^{8}	3.281×10^{8}	0.000×10^{0}

84	80.0-81.0	1.402×10^{8}	1.402×10^{8}	0.000×10^{0}
85	81.0-82.0	1.802×10^{8}	1.802×10^{8}	0.000×10^{0}
86	82.0-83.0	2.318×10^{8}	2.318×10^{8}	0.000×10^{0}
87	83.0-84.0	9.645×10^{8}	5.746×10^{8}	0.000×10^{0}
88	84.0-85.0	3.830×10^{8}	3.830×10^{8}	0.000×10^{0}
89	85.0-86.0	4.925×10^{8}	4.925×10^{8}	0.000×10^{0}
90	86.0-87.0	6.324×10^{8}	6.324×10^{8}	0.000×10^{0}
91	87.0-88.0	8.125×10^{8}	8.125×10^{8}	0.000×10^{0}
92	88.0-89.0	1.044×10^{9}	1.044×10^{9}	0.000×10^{0}
93	89.0-90.0	1.341×10^{9}	1.341×10^{9}	0.000×10^{0}
94	90.0-91.0	1.839×10^{9}	1.781×10^{9}	0.000×10^{0}
95	91.0-92.0	1.224×10^{9}	1.113×10^{9}	0.000×10^{0}
96	92.0-93.0	3.903×10^{8}	3.751×10^{8}	0.000×10^{0}
97	93.0-94.0	4.536×10^{8}	3.865×10^{8}	0.000×10^{0}
98	94.0-95.0	4.582×10^{8}	4.039×10^{8}	0.000×10^{0}
99	95.0-96.0	5.130×10^{7}	2.555×10^{7}	0.000×10^{0}
100	96.0-97.0	6.140×10^{7}	3.058×10^{7}	0.000×10^{0}
101	97.0-98.0	6.855×10^{9}	4.483×10^{9}	0.000×10^{0}
102	98.0-99.0	2.795×10^{8}	1.440×10^{8}	0.000×10^{0}
103	99.0-100.0	4.881×10^{8}	2.526×10^{8}	0.000×10^{0}
104	100.0-101.0	1.265×10^{8}	6.300×10^{7}	0.000×10^{0}
105	101.0-102.0	2.363×10^{8}	1.177×10^{8}	0.000×10^{0}
106	102.0-103.0	4.556×10^{9}	4.465×10^{9}	0.000×10^{0}
107	103.0-104.0	5.992×10^{9}	5.638×10^{9}	0.000×10^{0}
108	104.0-105.0	2.596×10^{8}	1.293×10^{8}	0.000×10^{0}
109	105.0-110.0	3.208×10^{9}	7.164×10^{8}	0.000×10^{0}
110	110.0-115.0	3.139×10^{9}	4.828×10^{8}	0.000×10^{0}
111	115.0-121.0	1.571×10^{10}	4.317×10^{9}	0.000×10^{0}
112	121.0-122.0	3.788×10^{11}	1.203×10^{11}	0.000×10^{0}
113	122.0-125.0	7.076×10^{9}	1.272×10^{9}	0.000×10^{0}
114	125.0-130.0	7.608×10^{9}	1.460×10^{9}	0.000×10^{0}
115	130.0-135.0	2.594×10^{10}	5.486×10^{9}	0.000×10^{0}
116	135.0-140.0	1.355×10^{10}	2.629×10^{9}	0.000×10^{0}
117	140.0-145.0	1.795×10^{10}	2.445×10^{9}	0.000×10^{0}
118	145.0-150.0	2.772×10^{10}	2.418×10^{9}	0.000×10^{0}
119	150.0-155.0	5.017×10^{10}	5.569×10^{9}	0.000×10^{0}
120	155.0-160.0	7.190×10^{10}	5.854×10^{9}	0.000×10^{0}
121	160.0-165.0	1.045×10^{11}	7.868×10^{9}	0.000×10^{0}
122	165.0-170.0	1.986×10^{11}	8.805×10^{9}	0.000×10^{0}
123	170.0-175.0	3.378×10^{11}	1.447×10^{10}	0.000×10^{0}

A.2 EUVAC Model Bins

The EUVAC model relies on the modified reference flux F74113 and a scaling factor A, which are binned according to wavelength. The values were reported in Richards et al. (1994) and are reproduced here in Table 27 for reference.

Table 27. The parameters for the EUVAC model. The F74113 fluxes in bins 1 and 2 were tripled, and bins 3 and 4 were doubled, according to Richards et al. (1994).

Bin, i	**Wavelength**, λ [nm]	**F74113** [$\times 10^{-9}$ photons cm^{-2} s^{-1}]	**A**
1	5-10	1.200	1.0017×10^{-2}
2	10-15	0.450	7.1250×10^{-3}
3	15-20	4.800	1.3375×10^{-2}
4	20-25	3.100	1.9450×10^{-2}
5	25.632	0.460	2.7750×10^{-3}
6	28.415	0.210	1.3768×10^{-1}
7	25-30	1.679	2.6467×10^{-2}
8	30.331	0.800	2.500×10^{-2}
9	30.378	6.900	3.3333×10^{-3}
10	30-35	0.965	2.2450×10^{-2}
11	36.807	0.650	6.5917×10^{-3}
12	35-40	0.314	3.6542×10^{-2}
13	40-45	0.383	7.4083×10^{-3}
14	46.522	0.290	7.4917×10^{-3}
15	45-50	0.285	2.0225×10^{-2}
16	50-55	0.452	8.7583×10^{-3}
17	55.437	0.720	3.2667×10^{-3}
18	58.433	1.270	5.1583×10^{-3}
19	55-60	0.357	3.6583×10^{-3}
20	60.976	0.530	1.6175×10^{-2}
21	62.973	1.590	3.3250×10^{-3}
22	60-65	0.342	1.1800×10^{-2}
23	65-70	0.230	4.2667×10^{-3}
24	70.336	0.360	3.0417×10^{-3}
25	70-75	0.141	4.7500×10^{-3}
26	76.515	0.170	3.8500×10^{-3}
27	77.041	0.260	1.2808×10^{-2}
28	78.936	0.702	3.2750×10^{-3}
29	75-80	0.758	4.7667×10^{-3}
30	80-85	1.625	4.8167×10^{-3}
31	85-90	3.537	5.6750×10^{-3}
32	90-95	3.000	4.9833×10^{-3}
33	97.702	4.400	3.9417×10^{-3}
34	95-100	1.475	4.4167×10^{-3}
35	102.572	3.500	5.1833×10^{-3}
36	103.191	2.100	5.2833×10^{-3}
37	100-105	2.467	4.3750×10^{-3}

A.3 GLOW Input File

GLOW run using the command line requires an input file saved as a text file. demonstrated in Table 28. The variables required are the year combined with the day of the year (Date), written for example as 2003001 for 1 January 2003; the time (UT) in UTC; the latitude (lat); the longitude (lon); the 81-day average $F_{10.7}$ (F107a) in [sfu]; the daily $F_{10.7}$ (F107) in [sfu]; the previous day's $F_{10.7}$ (F107p) in [sfu]; the Ap index (Ap); the auroral electron Maxwellian flux (Ef) in [erg/cm^2/s]; the auroral electron Maxwellian characteristic energy (Ec) in [eV]; the auroral proton Maxwellian energy flux (PFmax) in [erg/cm^2/s]; the auroral proton Maxwellian characteristic energy (PEmax) in [eV]; and either 0, 1, or 2 to indicate which solar spectrum scheme to use (ss), where 0 corresponds to the Hinteregger method, 1 to EUVAC, and 2 to the user-supplied solar spectrum file. Unless modeling the aurora, Ef, Ec, PFmax, and PEmax are usually left as 0.0.

Table 28. The format for the GLOW input text file, and can be separated by either tabs or spaces. Each input value besides the year with the day of the year and the solar spectrum indicator has one decimal point.

Variable	Units	Example
Date	yyyyddd	2016355
UT	UTC	12.0
lat	°	0.0
lon	°	180.0
F107a	sfu	100.0
F107	sfu	100.0
F107p	sfu	100.0
Ap	–	4.0
Ef	erg/cm^2/s	0.0
Ec	eV	0.0
PFmax	erg/cm^2/s	0.0
PEmax	eV	0.0
ss	–	1

Bibliography

115th Congress. National Defense Authorization Act for Fiscal Year 2018, 2018.

116th Congress. Promoting Research and Observations of Space Weather to Improve the Forecasting of Tomorrow Act, 2020.

Acebal, A. O. *Extending F10.7's Time Resolution to Capture Solar Flare Phenomena*. PhD thesis, Utah State University, 2008.

Angryk, R., Martens, P., Aydin, B., Kempton, D., Mahajan, S., Basodi, S., Ahmadzadeh, A., Cai, X., Filali Boubrahimi, S., Hamdi, S. M., Schuh, M., and Georgoulis, M. SWAN-SF, 2020. URL https://dataverse.harvard.edu/dataset.xhtml?persistentId=doi:10.7910/DVN/EBCFKM.

Appleton, E. V. and Barnett, M. A. F. On some direct evidence for downward atmospheric reflection of electric rays. *Proceedings of the Royal Society of London. Series A, Containing Papers of a Mathematical and Physical Character*, 109(752): 621–641, 12 1925. ISSN 0950-1207. doi: 10.1098/rspa.1925.0149. URL https://royalsocietypublishing.org/doi/10.1098/rspa.1925.0149.

Atkinson, N. Solar Flares Can Now Be Predicted More Accurately. *Universe Today*, 1 2010. URL https://www.universetoday.com/51585/solar-flares-can-now-be-predicted-more-accurately/.

Barth, C. A., Tobiska, W. K., Rottman, G. J., and White, O. R. Comparison of 10.7 cm radio flux with SME solar Lyman alpha flux. *Geophysical Research Letters*, 17(5):571–574, 4 1990. ISSN 00948276. doi: 10.1029/GL017i005p00571. URL http://doi.wiley.com/10.1029/GL017i005p00571.

Bell, T. E. and Phillips, T. A Super Solar Flare. *NASA Science*, 5 2008. URL https://science.nasa.gov/science-news/science-at-nasa/2008/06may_carringtonflare.

Berghmans, D., Van der Linden, R. A., Vanlommel, P., Clette, F., and Robbrecht, E. History of the Sunspot Index : 25 years SIDC. *Beitrage zur Geschichte der Geophysik und Kosmischen Physik VII*, 1(288):1–12, 2006.

Bilitza, D. International Reference Ionosphere. Technical report, Science Applications Research, Lanham, 11 1990. URL http://irimodel.org/docs/IRI1990pp0-84.pdf.

Bilitza, D. IRI the International Standard for the Ionosphere. *Advances in Radio Science*, 16:1–11, 9 2018. ISSN 1684-9973. doi: 10.5194/ars-16-1-2018. URL https://ars.copernicus.org/articles/16/1/2018/.

Board, S. S., Sciences, P., and Committee on the Societal and Economic Impacts of Severe Space Weather Events. *Severe Space Weather Events–Understanding Societal and Economic Impacts*. National Academies Press, Washington, D.C., 12 2008. ISBN 9780309127691. doi: 10.17226/12507. URL http://www.nap.edu/catalog/12507.

Bonadonna, M., Lanzerotti, L., and Stailey, J. The National Space Weather Program: Two decades of interagency partnership and accomplishments. *Space Weather*, 15 (1):14–25, 1 2017. doi: 10.1002/2016SW001523.

Boteler, D. H. A 21st Century View of the March 1989 Magnetic Storm. *Space Weather*, 17(10):1427–1441, 10 2019. ISSN 1542-7390. doi: 10.1029/2019SW002278. URL https://onlinelibrary.wiley.com/doi/abs/10.1029/2019SW002278.

Breit, G. and Tuve, M. A. A Radio Method of Estimating the Height of the Conducting Layer. *Nature*, 116(2914):357–357, 9 1925. ISSN 0028-0836. doi: 10.1038/116357a0. URL https://www.nature.com/articles/116357a0.pdfhttp://www.nature.com/articles/116357a0.

Bridgman, C. J. *Introduction to the Physics of Nuclear Weapons Effects*. Defense Threat Reduction Agency, Ft. Belvoir, first edition, 2001.

Burg, K. S. *Validation technique for modeled bottomside ionospheres using ray tracing*. 2020. URL https://scholar.afit.edu/etd/3192.

Cannon, P., Angling, M., Barclay, L., Curry, C., Dyer, C., Edwards, R., Greene, G., Horne, R., Hapgood, M., Owen, J., Jackson, D., Mitchell, C., Richards, A., Ryden, K., Rogers, C., Saunders, S., Tanner, R., Sweeting, M., Thomson, A., and Underwood, C. *Extreme space weather: impacts on engineered systems and infrastructures*. Royal Academy of Engineering, London, 2013. ISBN 1-903496-95-0. URL http://www.raeng.org.uk/news/publications/list/reports/Space_Weather_Full_Report_Final.PDF.

Carrington, R. C. Description of a Singular Appearance seen in the Sun on September 1, 1859. *Monthly Notices of the Royal Astronomical Society*, 20(1):13–15, 11 1859. ISSN 0035-8711. doi: 10.1093/mnras/20.1.13. URL https://academic.oup.com/mnras/article-lookup/doi/10.1093/mnras/20.1.13.

Carter, J. The Sun Just Woke Up. 'M-Class' Solar Flare Ends 925-Day Solar Snooze, 5 2020. URL https://www.forbes.com/sites/jamiecartereurope/2020/05/29/the-sun-just-woke-up-m-class-solar-flare-ends-925-day-solar-snooze.

Chakraborty, S. *Characterization and Modeling of Solar Flare Effects in the Iono-*

sphere Observed by HF Instruments. PhD thesis, Virginia Polytechnic Institute and State University, 2021.

Chamberlin, P. C., Eparvier, F. G., Knoer, V., Leise, H., Pankratz, A., Snow, M., Templeman, B., Thiemann, E. M., Woodraska, D. L., and Woods, T. N. The Flare Irradiance Spectral Model-Version 2 (FISM2). *Space Weather*, 18(12), 2020. ISSN 15427390. doi: 10.1029/2020SW002588. URL https://doi.org/10.1029/2020SW002588.

Chamberlin, P. C., Woods, T. N., and Eparvier, F. G. Flare Irradiance Spectral Model (FISM): Flare component algorithms and results. *Space Weather*, 6(5):n/a–n/a, 5 2008. ISSN 15427390. doi: 10.1029/2007SW000372. URL http://doi.wiley.com/10.1029/2007SW000372.

Chapman, S. The absorption and dissociative or ionizing effect of monochromatic radiation in an atmosphere on a rotating earth. *Proceedings of the Physical Society*, 43(1):26–45, 1931. ISSN 09595309. doi: 10.1088/0959-5309/43/1/305.

Citrone, P. J. Paper Session I-B - USAF Space Weather Support. In *The Space Congress Proceedings*, volume 20, pages 8–15, 1995.

Clette, F. Is the F 10.7cm – Sunspot Number relation linear and stable? *Journal of Space Weather and Space Climate*, 11:2, 1 2021. ISSN 2115-7251. doi: 10.1051/swsc/2020071. URL https://www.swsc-journal.org/10.1051/swsc/2020071.

Clette, F., Berghmans, D., Vanlommel, P., Van der Linden, R. A., Koeckelenbergh, A., and Wauters, L. From the Wolf number to the International Sunspot Index: 25 years of SIDC. *Advances in Space Research*, 40(7):919–928, 1 2007. ISSN 02731177. doi: 10.1016/j.asr.2006.12.045. URL https://linkinghub.elsevier.com/retrieve/pii/S0273117707001974.

Codrescu, M. The influence of the ionosphere on GPS Operations. In *Applications of GPS/GNSS in NOAA*, Boulder, CO, 2007. Space Weather Prediction Center, NCEP/NWS/NOAA. URL ftp://ftp.ngdc.noaa.gov/STP/GPS_GNSS/Mihail's.pdf.

Conrad, E. E., Gurtman, G. A., Kweder, G., Mandell, M. J., and White, W. W. Collateral Damage to Satellites from an EMP Attack. Technical report, Defense Threat Reduction Agency, Ft. Belvoir, 2010.

Dao, E. V., McNamara, L. F., and Colman, J. J. Magnetic field effects on the accuracy of ionospheric mirror models for geolocation. *Radio Science*, 51(4):284–300, 2016. ISSN 1944799X. doi: 10.1002/2015RS005884.

Dudok de Wit, T. and Bruinsma, S. The 30 cm radio flux as a solar proxy for thermosphere density modelling. *Journal of Space Weather and Space Climate*, 7:A9, 3 2017. ISSN 2115-7251. doi: 10.1051/swsc/2017008. URL http://www.swsc-journal.org/10.1051/swsc/2017008.

European Commission. Ionospheric Correction Algorithm for Galileo Single Frequency Users. 2016.

Floyd, L., Newmark, J., Cook, J., Herring, L., and McMullin, D. Solar EUV and UV spectral irradiances and solar indices. *Journal of Atmospheric and Solar-Terrestrial Physics*, 67(1-2):3–15, 1 2005. ISSN 13646826. doi: 10.1016/j.jastp.2004.07.013. URL https://linkinghub.elsevier.com/retrieve/pii/S1364682604001737.

Foster, B. TIEGCM Documentation. Technical report, NCAR High Altitude Observatory, 2016.

Foukal, P. *Solar Astrophysics*. Wiley-VCH, Weinheim, 3rd edition, 2013. ISBN 978-3-527-41103-0.

Galkin, I. A., Khmyrov, G. M., Kozlov, A. V., Reinisch, B. W., Huang, X., and Paznukhov, V. V. The ARTIST 5. *AIP Conference Proceedings*, 974(February): 150–159, 2008. ISSN 0094243X. doi: 10.1063/1.2885024.

Ginet, G., Nowak, J., Weber, Z., Mullins, M., Fawcett, G., Appadwedula, S., DeOliveira-Costa, A., Teig, L., Davis, R., Rosario, E., Franzini, C., and Best, S. HFGeo Long Term Collect. Technical report, MIT Lincoln Laboratory, MITRE Corporation, 2018.

Gombosi, T. I., Baker, D. N., Balogh, A., Erickson, P. J., Huba, J. D., and Lanzerotti, L. J. Anthropogenic Space Weather. *Space Science Reviews*, 212(3-4):985–1039, 2017. ISSN 15729672. doi: 10.1007/s11214-017-0357-5.

Heaviside, O. Telegraphy, 1902.

Hinteregger, H. E., Fukui, K., and Gilson, B. R. Observational, reference and model data on solar EUV, from measurements on AE-E. *Geophysical Research Letters*, 8(11):1147–1150, 11 1981. ISSN 00948276. doi: 10.1029/GL008i011p01147. URL `http://doi.wiley.com/10.1029/GL008i011p01147`.

Hodgson, R. On a curious Appearance seen in the Sun. *Monthly Notices of the Royal Astronomical Society*, 20(1):15–16, 11 1859. ISSN 0035-8711. doi: 10.1093/mnras/20.1.15. URL `https://academic.oup.com/mnras/article-lookup/doi/10.1093/mnras/20.1.15`.

Huang, Y., Richmond, A. D., Deng, Y., Chamberlin, P. C., Qian, L., Solomon, S. C., Roble, R. G., and Xiao, Z. Wavelength dependence of solar irradiance enhancement during X-class flares and its influence on the upper atmosphere. *Journal of Atmospheric and Solar-Terrestrial Physics*, 115-116:87–94, 8 2014. ISSN 13646826. doi: 10.1016/j.jastp.

2013.10.011. URL http://dx.doi.org/10.1016/j.jastp.2013.10.011https://linkinghub.elsevier.com/retrieve/pii/S1364682613002824.

Huba, J. D., Maute, A., and Crowley, G. SAMI3_ICON: Model of the Ionosphere/-Plasmasphere System. *Space Science Reviews*, 212(1-2):731–742, 10 2017. ISSN 0038-6308. doi: 10.1007/s11214-017-0415-z.

ITU Radiocommunication Assembly. Choice of Indices for Long-Term Ionospheric Predictions. Technical Report 8, ITU Radiocommunication Assembly, 1999.

Jones, R. M. and Stephenson, J. J. A versatile three-dimensional ray tracing computer program for radio waves in the ionosphere. Technical Report 75-76, 1975. URL https://www.researchgate.net/publication/260960849_A_versatile_three-dimensional_ray_Tracing_computer_program_for_radio_waves_in_the_ionosphere.

Kennelly, A. E. Research in Telegraphy. *Electric World and Engineering*, 6:473, 1902.

Kimball, D. S. A Study of the Aurora of 1859. *Geophysical Institute*, (6), 1960.

King, J. H. and Papitashvili, N. E. Solar wind spatial scales in and comparisons of hourly Wind and ACE plasma and magnetic field data. *Journal of Geophysical Research: Space Physics*, 110(A2):1–9, 2005. ISSN 21699402. doi: 10.1029/2004JA010649.

Knipp, D. J., Ramsay, A. C., Beard, E. D., Boright, A. L., Cade, W. B., Hewins, I. M., McFadden, R. H., Denig, W. F., Kilcommons, L. M., Shea, M. A., and Smart, D. F. The May 1967 great storm and radio disruption event: Extreme space weather and extraordinary responses. *Space Weather*, 14(9):614–633, 9 2016. doi: 10.1002/2016SW001423.

Kranich, S. N. *CORRELATION OF SOLAR X-RAY FLUX AND SID MODIFIED VLF SIGNAL STRENGTH*. PhD thesis, Air Force Institute of Technology, 2015.

Liebowitz, R. P. Donald Menzel and the Creation of the Sacramento Peak Observatory. *Journal for the History of Astronomy*, 33(2):193–211, 5 2002. ISSN 0021-8286. doi: 10.1177/002182860203300207. URL http://journals.sagepub.com/doi/10.1177/002182860203300207.

Lipiec, E. and Humphreys, B. E. Space Weather : An Overview of Policy and Select U . S . Government Roles and Responsibilities. Technical report, Congressional Research Service, 2020.

Longmire, C. L. On the Electromagnetic Pulse Produced by Nuclear Explosions. *IEEE Transactions on Electromagnetic Compatibility*, EMC-20(1):3–13, 1978. ISSN 1558187X. doi: 10.1109/TEMC.1978.303688.

Markus, R. M., Halbeisen, N. F., and Fuller, J. F. Air Weather Service: Our Heritage. Technical report, Military Airlift Command Historical Office, Scott Air Force Base, IL, 1987.

Mauceri, S., Pilewskie, P., Woods, T., Béland, S., and Richard, E. Intercomparing Solar Spectral Irradiance From SORCE SIM. *Earth and Space Science*, 7(4):1–16, 4 2020. ISSN 2333-5084. doi: 10.1029/2019EA001002. URL https://doi.org/10.1029/2019EA001002https://onlinelibrary.wiley.com/doi/abs/10.1029/2019EA001002.

McIntosh, S. W., Chapman, S., Leamon, R. J., Egeland, R., and Watkins, N. W. Overlapping Magnetic Activity Cycles and the Sunspot Number: Forecasting Sunspot Cycle 25 Amplitude. *Solar Physics*, 295(12):163, 12 2020. ISSN 0038-0938. doi: 10.1007/s11207-020-01723-y. URL http://arxiv.org/abs/2006.

15263http://dx.doi.org/10.1007/s11207-020-01723-yhttps://www.http://link.springer.com/10.1007/s11207-020-01723-y.

Mitra, A. P. The D-region of the ionosphere. *Endeavour*, 2(1):12–21, 1 1978. ISSN 0160-9327. doi: 10.1016/0160-9327(78)90028-5.

Nava, B., Coïsson, P., and Radicella, S. M. A new version of the NeQuick ionosphere electron density model. *Journal of Atmospheric and Solar-Terrestrial Physics*, 70 (15):1856–1862, 2008. ISSN 13646826. doi: 10.1016/j.jastp.2008.01.015.

NOAA Space Weather Prediction Center. Solar Cycle 25 Forecast Update, 12 2019. URL https://www.swpc.noaa.gov/news/solar-cycle-25-forecast-update.

Obama, B. Executive Order 13744, 2016.

Pisacane, V. L. *The Space Environment and Its Effects on Space Systems*. AIAA Press, Reston, second edition, 2016. ISBN 978-1-62410-353-7.

Popik, T. S., Kearns, J. T., Baker, G. H., Cooper, H. F., and Harris, W. R. High Consequence Scenarios for North Korean Atmospheric Nuclear Tests with Policy Recommendations for the U. S. Government High Consequence Scenarios for North Korean Atmospheric Nuclear Tests with Policy Recommendations for the U. S. Government. 2017.

Poppe, B. B. and Jorden, K. P. *Sentinels of the Sun: Forecasting Space Weather*. Bower House, Boulder, CO, 2006. ISBN 1555663796.

Qian, L., Burns, A. G., Emery, B. A., Foster, B., Lu, G., Maute, A., Richmond, A. D., Roble, R. G., Solomon, S. G., and Wang, W. The NCAR TIE-GCM: A Community Model of the Coupled Thermosphere/Ionosphere System. In Huba,

J. D., Schunk, R. W., and Khazanov, G., editors, *Modeling the Ionosphere– Thermosphere System*, pages 72–83. American Geophysical Union, Boulder, CO, 2013. ISBN 9780875904917. doi: 10.1029/2012GM001297.

Reda, I. and Andreas, A. Solar Position Algorithm for Solar Radiation Applications (Revised). *National Renewable Energy Laboratory Nrel/Tp-560-34302*, (January): 1–56, 2005. ISSN 0038-092X.

Reinisch, B. W. and Galkin, I. A. Global Ionospheric Radio Observatory (GIRO). *Earth, Planets and Space*, 63(4):377–381, 4 2011. ISSN 1343-8832. doi: 10.5047/eps.2011.03.001.

Richards, P. G., Fennelly, J. A., and Torr, D. G. EUVAC: A solar EUV Flux Model for aeronomic calculations. *Journal of Geophysical Research*, 99(A5):8981, 1994. ISSN 0148-0227. doi: 10.1029/94JA00518. URL `http://doi.wiley.com/10.1029/94JA00518`.

Ridley, A. J., Deng, Y., and Tóth, G. The global ionosphere-thermosphere model. *Journal of Atmospheric and Solar-Terrestrial Physics*, 68(8):839–864, 2006. ISSN 13646826. doi: 10.1016/j.jastp.2006.01.008.

Roy, V. sun_position.m, 2004.

Russel, C. T., Luhmann, J. G., and Strangeway, R. J. *Space Physics: An Introduction*. Cambridge University Press, Cambridge, first edition, 2016. ISBN 978-1-107-09882-4.

Scherliess, L., Schunk, R. W., Gardner, L. C., Zhu, L., Eccles, J. V., and Sojka, J. J. The USU-GAIM Data Assimilation Models for Ionospheric Specifications and Forecasts. 2017.

Schunk, R. and Nagy, A. *Ionospheres: Physics, Plasma Physics, and Chemistry*. Cambridge University Press, New York, second edition, 2009. ISBN 978-0-521-87706-0.

Schwalbe, S. *Modeling High-Altitude Nuclear Detonations Using Existing Ionospheric Models*. Number March. Wright-Patterson AFB, 2019.

Shim, J. S., Kuznetsova, M., Rasttter, L., Bilitza, D., Butala, M., Codrescu, M., Emery, B. A., Foster, B., Fuller-Rowell, T. J., Huba, J., Mannucci, A. J., Pi, X., Ridley, A., Scherliess, L., Schunk, R. W., Sojka, J. J., Stephens, P., Thompson, D. C., Weimer, D., Zhu, L., and Sutton, E. CEDAR electrodynamics thermosphere ionosphere (ETI) challenge for systematic assessment of ionosphere/thermosphere models: Electron density, neutral density, NmF2, and hmF2 using space based observations. *Space Weather*, 10(10), 2012. ISSN 15427390. doi: 10.1029/2012SW000851.

Solomon, S. Preliminary Documentation for the GLOW Model. 9 2018. URL `http://download.hao.ucar.edu/pub/stans/glow/docs/Glow.txt`.

Solomon, S. C. Global modeling of thermospheric airglow in the far ultraviolet. *Journal of Geophysical Research: Space Physics*, 122(7):7834–7848, 2017. ISSN 21699402. doi: 10.1002/2017JA024314.

Solomon, S. C. and Qian, L. Solar extreme-ultraviolet irradiance for general circulation models. *Journal of Geophysical Research: Space Physics*, 110(A10):1–14, 2005. ISSN 21699402. doi: 10.1029/2005JA011160.

Space Weather Operations; Research; and Mitigation Working Group, Subcommittee, S. W. S., Hazards, and Committee on Homeland and National Security of the National Science & Technology Council. National Space Weather Strategy and

Action Plan. Technical Report March, Office of Science and Technology Policy, Washington, D.C., 2019.

Stuckenberg, D., Woolsey, R. J., and DeMaio, D. Electromagnetic Defense Task Force. Technical report, LeMay Center for Doctrine Development and Education, Maxwell Air Force Base, 11 2018.

Tapping, K. F. The 10.7 cm solar radio flux (F10.7). *Space Weather*, 11(7):394–406, 2013. ISSN 15427390. doi: 10.1002/swe.20064.

Tiwari, B. R. and Kumar, M. The Solar Flux and Sunspot Number; A Long-Trend Analysis. *International Annals of Science*, 5(1):47–51, 7 2018. ISSN 2456-7132. doi: 10.21467/ias.5.1.47-51. URL `https://journals.aijr.in/index.php/ias/article/view/751`.

Trump, D. J. Executive Order 13865, 2019.

USA National Science and Technology Council. National Space Weather Action Plan. Technical report, 2015. URL `https://www.whitehouse.gov/sites/default/files/microsites/ostp/final_nationalspaceweatheractionplan_20151028.pdf`.

Viereck, R., Puga, L., McMullin, D., Judge, D., Weber, M., and Tobiska, W. K. The Mg II index: A proxy for solar EUV. *Geophysical Research Letters*, 28(7): 1343–1346, 2001. ISSN 00948276. doi: 10.1029/2000GL012551.

Wertz, J. R. and Larson, W. J. *Space Mission Analysis and Design*. Microcosm Press and Springer, Hawthorne, CA and New York, NY, third edition, 2007. ISBN 978-1881883-10-4.

Zhu, L., Schunk, R. W., Jee, G., Scherliess, L., Sojka, J. J., and Thompson, D. C.

Validation study of the Ionosphere Forecast Model using the TOPEX total electron content measurements. *Radio Science*, 41(05):6, 2006. doi: 10.1029/2005RS003336.

REPORT DOCUMENTATION PAGE

Form Approved
OMB No. 0704–0188

1. REPORT DATE *(DD–MM–YYYY)*	2. REPORT TYPE	3. DATES COVERED *(From — To)*
06–09–2021	Dissertation	Oct 2018 — Sep 2021

4. TITLE AND SUBTITLE

Development and Verification
of Extreme Space Weather Phenomena Models

5a. CONTRACT NUMBER

5b. GRANT NUMBER

5c. PROGRAM ELEMENT NUMBER

6. AUTHOR(S)

Schwalbe, Sophia Gloria, Capt, USAF

5d. PROJECT NUMBER

5e. TASK NUMBER

5f. WORK UNIT NUMBER

7. PERFORMING ORGANIZATION NAME(S) AND ADDRESS(ES)

Air Force Institute of Technology
Graduate School of Engineering and Management (AFIT/EN)
2950 Hobson Way
WPAFB OH 45433-7765

8. PERFORMING ORGANIZATION REPORT NUMBER

AFIT-ENP-DS-21-S-034

9. SPONSORING / MONITORING AGENCY NAME(S) AND ADDRESS(ES)

Air Force Research Laboratory/Space Vehicles
3550 Aberdeen Avenue SE
Kirtland AFB, NM 87117
COMM 505-246-5397
Email: christopher.fallen.1@spaceforce.mil

10. SPONSOR/MONITOR'S ACRONYM(S)

AFRL/RV

11. SPONSOR/MONITOR'S REPORT NUMBER(S)

12. DISTRIBUTION / AVAILABILITY STATEMENT

DISTRIBUTION STATEMENT A: APPROVED FOR PUBLIC RELEASE; DISTRIBUTION UNLIMITED

13. SUPPLEMENTARY NOTES

14. ABSTRACT

A range of 14 M-class flares from 1 June 2015 to 27 September 2016 were analyzed to find significant trends in electron frequency profile modeling using the GLobal airglOW (GLOW) model and radar parameters using a ray tracing algorithm developed by the Air Force Research Laboratory. GLOW was run for all the flares using three different solar spectrum schemes and an average of the three: the Hinteregger method, EUV flux model for aeronomic calculations (EUVAC), and a rebinned Flare Irradiance Spectrum Model (FISM) result. Comparing data for the E-layer where GLOW is most accurate, it was determined that GLOW using EUVAC performed best at the peak flare time for determining both the peak altitude and frequency of the E-region, while using FISM as a user-supplied spectrum in GLOW was less accurate for estimating both, likely due to the extreme variations in solar flux, coarse binning scheme, and lack of robust chemistry and energy calculations within GLOW. GLOW performed better at predicting peak altitude and frequency than the International Reference Ionosphere (IRI), which is often used as a basis for ionosphere predictions. GLOW also outperformed IRI at modeling the radar parameters before and during the solar flares, though no significant trends were found. GLOW using EUVAC or FISM showed promise at predicting the radar parameters and their change over time, but the ray tracing algorithm produced solutions that varied between E- and F-layers and O- and X-modes, leading to results that were often skewed or varied drastically in time.

15. SUBJECT TERMS

Solar Flares, Ionosphere, Ionospheric Models, Space Weather, Ray Tracing

16. SECURITY CLASSIFICATION OF:			17. LIMITATION OF ABSTRACT	18. NUMBER OF PAGES	19a. NAME OF RESPONSIBLE PERSON
a. REPORT	b. ABSTRACT	c. THIS PAGE			Dr. Robert Loper, AFIT/ENP
U	U	U	UU	149	19b. TELEPHONE NUMBER *(include area code)* (937) 266-5506; robert.d.loper@nasa.gov